

OPTICAL PERFORMANCE OF RANDOM ANTI-REFLECTION
STRUCTURED SURFACES (RARSS) ON SPHERICAL LENSES

by

Courtney D. Taylor

A dissertation submitted to the faculty of
The University of North Carolina at Charlotte
in partial fulfillment of the requirements
for the degree of Doctor of Philosophy in
Optical Science and Engineering

Charlotte

2016

Approved by:

Dr. Menelaos K. Poutous

Dr. Ishwar D. Aggarwal

Dr. Glenn D. Boreman

Dr. Chris J. Evans

Dr. Tom Weldon

©2016
Courtney D. Taylor
ALL RIGHTS RESERVED

ABSTRACT

COURTNEY D. TAYLOR. Optical performance of random anti-reflection structured surfaces (rARSS) on spherical lenses. (Under the direction of DR. MENELAOS K. POUTOUS)

Random anti-reflection structured surfaces (rARSS) have been reported to improve transmittance of optical-grade fused silica planar substrates to values greater than 99%. These textures are fabricated directly on the substrates using reactive-ion/inductively-coupled plasma etching (RIE/ICP) techniques, and often result in transmitted spectra with no measurable interference effects (fringes) for a wide range of wavelengths. The RIE/ICP processes used in the fabrication process to etch the rARSS is anisotropic and thus well suited for planar components. The improvement in spectral transmission has been found to be independent of optical incidence angles for values from 0° to $\pm 30^\circ$. Qualifying and quantifying the rARSS performance on curved substrates, such as convex lenses, is required to optimize the fabrication of the desired AR effect on optical-power elements. In this work, rARSS was fabricated on fused silica plano-convex (PCX) and plano-concave (PCV) lenses using a planar-substrate optimized RIE process to maximize optical transmission in the range from 500 to 1100 nm. An additional set of lenses were etched in a non-optimized ICP process to provide additional comparisons. Results are presented from optical transmission and beam propagation tests (optimized lenses only) of rARSS lenses for both TE and TM incident polarizations at a wavelength of 633 nm and over a 70° full field of view in both singlet and doublet configurations. These results suggest optimization of the fabrication process is not required, mainly due to the wide angle-

of-incidence AR tolerance performance of the rARSS lenses. Non-optimized recipe lenses showed low transmission enhancement, and confirmed the need to optimized etch recipes prior to process transfer of PCX/PCV lenses. Beam propagation tests indicated no major beam degradation through the optimized lens elements. Scanning electron microscopy (SEM) images confirmed different structure between optimized and non-optimized samples. SEM images also indicated isotropically-oriented surface structures on both types of lenses.

ACKNOWLEDGMENTS

I would like to thank myself, for the hard work and perseverance it has taken to make it this far. With my help, I have succeeded in my endeavors. My will to keep facing each challenge has faltered at times, but with my support I have continued on. All of my success I owe to me.

I give thanks to God Almighty, who has given unto this Earth the greatest head of hair ever to grace optical science and engineering, and thanks to my efforts to expose the world to this follicular miracle. It is through Him that all things are totally bitchin'.

Thank you to me, who has chosen friends and would-be family to care for me and cook my dinners because let's be real I can't cook and no one wants to eat my signature burnt salad. Thanks to my partner Luke, who has ensured that my sacred hands do not touch a dirty dish.

I would also like to thank I for all of the sacrifices I have made in service to myself. Through salad-dressing sandwiches on dumpster bread, barbecue-sauce soups, stolen flat beer and soggy cigarettes I have kept going. Nights spent sleeping in a leaky car and on a friend's sofa have paid off. Now I have the sofa and the legally-purchased food. Look at me, I'm the captain now.

Finally, thanks to me for ignoring as many people as possible. By valuing my own life, knowledge, and experience over others, I have achieved my dreams. As the Latins say, "Illegitimi non carborundum", which of course means "Never give up, never surrender".

TABLE OF CONTENTS

LIST OF FIGURES	viii
LIST OF TABLES	xviii
CHAPTER 1: INTRODUCTION	1
1.1. Introduction to Random Anti-Reflection Surface Structures	1
1.2. Fabrication of Surface Structure	4
1.3. Performance Measurement Tools	7
1.4. Transmission Analysis of Random Anti-Reflection Surface Structure on Singlet Lenses	10
1.4.1. Transmission Determination of Untreated Lenses	10
1.4.2. Transmission Determination of Anti-reflection Coated Lenses	16
1.5. Transmission and Beam Profile Determination of Performance of Random Anti-Reflection Surface Structures on Doublet Lenses	30
1.5.1. Transmission Determination of Doublet Lenses	30
1.5.2. Gaussian Beam Propagation Through Multi-Element Systems	32
1.5.3. Seidel Wavefront Aberrations	46
1.6. Proposed Methodology for Performance Measurement of Random Anti-Reflection Surface Structure on Curved Surfaces	48
CHAPTER 2: TRANSMISSION PERFORMANCE OF SINGLET LENSES WITH RANDOM ANTI-REFLECTION SURFACE STRUCTURE	52
2.1. Introduction	52
2.2. Experimental Implementation	52

	vii
2.3. Computation of Transmission of Lens Elements	60
2.4. Transmission Performance Results of Spherical Lenses with random Anti-Reflection Surface Structure	69
2.5. Conclusions of Performance of Random Anti-Reflection Surface Structure on Singlet Lenses	90
CHAPTER 3: TRANSMISSION AND BEAM PROFILE PERFORMANCE OF DOUBLET LENSES	95
3.1. Introduction	95
3.2. Experimental Implementation	95
3.3. Computation of Transmission and Beam Propagation Through Doublet Lenses	98
3.4. Performance Results	106
3.4.1. Transmission Performance Results	106
3.4.2. Beam Profile Performance Results	113
3.5. Conclusions of Performance of Random Anti-Reflection Surface Structure on Doublet Lenses	120
CHAPTER 4: CONCLUSIONS	125
4.1. Summary of Optical Performance of Random Anti-Reflection Surface Structure	125
4.2. Future Work	128
4.2.1. Random Anti-Reflection Surface Structure on Microlens Arrays	128
4.2.2. Wavefront Performance and Scattering Measurements of Random Anti-Reflection Surface Structure on Non-Planar Surfaces	130
REFERENCES	131

LIST OF FIGURES

- FIGURE 1: Measured transmission for FS over a wavelength range of 500nm to 2000nm. The black line is the transmission for planar fused silica (FS) with no rARSS, and the blue line is the transmission for planar FS with one side etched with rARSS for peak transmission at 633nm. The red line is the transmission enhancement of the rARSS sample over the unetched sample. The vertical dashed line indicates the design peak wavelength of 633nm. The dip in transmission around 1400nm is due to the absorption of water in the FS. 8
- FIGURE 2: A section of a spherical surface with a ray, k , incident at a non-zero angle θ_i with respect to the optical axis z . A location of interest away from the apex of the surface experiences a further angular deviation, θ_d . A new axis normal to the curved surface, z' , is then used as the reference of z to determine θ'_i . 12
- FIGURE 3: Spherical lens surface sag. $s(r)$ represents the sag of the lens at a distance r from the apex of the lens. R represents the radius of curvature; in the special case of a spherical lens, it is equivalent to the focal length of the front surface. 13
- FIGURE 4: Global and corresponding local angle values over the convex surfaces of PCX and PCV FS test lenses: (a) +50mm EFL, (b) -50mm EFL, (c) +75mm EFL, (d) -75mm EFL, (e) +100mm EFL, (f) -100 mm EFL. A graphic of the corresponding lens is shown in each plot. For each, the black line is the 0° global angle, the red line is the 15° global angle, and the blue line is the 30° global. For a given global angle over a clear aperture of 18mm, the local angle has a range of over 45°. 14
- FIGURE 5: Total intensity transmission for a parallel-surface single slab showing the effect of summing multiple internal incoherent reflections. 15
- FIGURE 6: Representation of spherical surface as adjacent planar trapezoid segments. (a) Spherical surface to be modeled, (b) trapezoidal arrangement condensing surface to planar segments. If an incident wave possesses a sufficiently small profile, then the simpler trapezoidal model can be used to determine transmission through the element as a whole. 17

- FIGURE 7: Doublet slab layout showing the additional surface reflections added by the second lens. 31
- FIGURE 8: Experimental layout used to measure localized transmission of rARSS lenses: L, +100mm EFL PCX lens that is focusing the incident beam to a $96\mu\text{m}$ spot size at the front surface of the test lens; TL, lens under test; P, photodiode detector; C, data-collecting PC. TL rests on a kinematic stage, allowing (a) translation along the vertical coordinate y and (b) rotation around the azimuth angle ϕ . 54
- FIGURE 9: Laser power test data over a time period of approximately 6300 seconds, or roughly 1 hour 45 minutes, beginning at laser start-up. 55
- FIGURE 10: OSLO sample ray trace diagram of the focusing lens L used to create the $96\mu\text{m}$ spot size on the test lens TL. Sample shown is +50mm EFL BK7 lens. Ray pencil from L to detector plane P is shown in blue. Diagram is to scale and is in mm. 55
- FIGURE 11: Global angle θ and corresponding local angle θ' . A global 60° field-of-view can be tested by tilting the element with respect to the back planar surface across a test full aperture of 12–15mm. (a) PCX lens tilted at global 0° , 15° , and 30° , with respect to the planar back surface. (b) PCX lens tilted at global -0° , -15° , and -30° , with respect to the planar back surface. The translated rays are shown in both cases. The localized rays are accessed by translating the lens holder along the vertical direction. The local angle is between the incoming ray and the curved surface normal. (c) Ray R incident on a curved surface C will have a different local angle θ' with respect to the surface normal when compared to the optic axis global angle θ . This angle will continue to change as the ray is translated across the open aperture. PCV lenses were measured in with the same arrangement. 56
- FIGURE 12: Global and corresponding local angle variation over the convex surface of +50mm EFL FS lens. The black line is the 0° global angle, the red line is the 15° global angle, and the blue line is the 30° global. For a given global angle over a clear aperture of 18mm, the local angle has a range of over 45° . The dashed lines represent the axes of radial position and local angle for ease of comparison. 57
- FIGURE 13: Azimuthal intervals used to verify azimuthal sampling value. From left to right: 45° , 30° , 20° , 10° . 58

FIGURE 14: Comparison of transmission performance based on azimuthal zone interval. (a) 45° interval, (b) 30° interval, (c) 20° interval, and (d) 10° interval. The performance measurement and error is consistent between 45° and 10° azimuthal intervals. 59

FIGURE 15: Two sets (\blacktriangle, \circ) of normalized transmission enhancement measurements $\tau_{123}(r)$ at normal incidence through a FS flat substrate with a thickness of 2 mm and diameter of 25.4 mm and a single rARSS surface using the test layout shown in Fig. ???. Each point shown is an average of 100 measurements on a single location using 45° linearly-polarized light. The standard deviation is the thickness of the circles shown. The +3% and +4% framing values are shown for comparison as dashed lines. The overall average transmission enhancement of the slabs is +3.6%, corresponding to a single-surface AR. 59

FIGURE 16: TE and TM transmission enhancement for a SLAR on FS as a function of AOI. The curves were obtained using Eqs. ?? and ??, and the specific thin-film values are given in the text. The vertical asymptote of the TM curve indicates the location of the Brewster's angle for the uncoated boundary. 65

FIGURE 17: Contour plots showing transmission enhancement $[\tau_{12}(\theta')]$ of equal relative values to the maximum possible (3.65%) obtained for a SLAR on FS as functions of the layer thickness in wavelength units and the layer index of refraction. (a) Equal transmission enhancement contours for AOI at 0°. (b) Equal transmission enhancement contours for AOI at 34.02°. In the latter case, the maximum transmission enhancement is 50% of the Fresnel losses due to a single airsilica boundary, occurring only at the center of the contours shown here. 67

FIGURE 18: Measured (bullets) and calculated (lines) normalized transmission of a FS planar substrate as functions of radial distance (r) for double-sided AR-coated BK7 lens (black), single-sided rARSS FS lens (red), and uncoated FS lens (blue). (a) TE and (b) TM incident polarization at global angle $\theta = 0^\circ$. (c) TE and (d) TM incident polarization at $\theta = 15^\circ$. (e) TE and (f) TM incident polarization at $\theta = 30^\circ$. The standard deviation of the experimental measurements is the thickness of the bullets if not shown as a vertical bar. 70

FIGURE 19: Measured (bullets) and calculated (lines) normalized transmission of a FS +50mm EFL PCX lens as functions of radial distance (r) for double-sided AR-coated BK7 lens (black), single-sided rARSS FS lens (red), and uncoated FS lens (blue). (a) TE and (b) TM incident polarization at $\theta = 0^\circ$. (c) TE and (d) TM incident polarization at $\theta = 15^\circ$. (e) TE and (f) TM incident polarization at $\theta = 30^\circ$. The standard deviation of the experimental measurements is the thickness of the bullets if not shown as a vertical bar.

71

FIGURE 20: Measured (bullets) and calculated (lines) normalized transmission of a FS +75mm EFL PCX lens as functions of radial distance (r) for double-sided AR-coated BK7 lens (black), single-sided rARSS FS lens (red), and uncoated FS lens (blue). (a) TE and (b) TM incident polarization at $\theta = 0^\circ$. (c) TE and (d) TM incident polarization at $\theta = 15^\circ$. (e) TE and (f) TM incident polarization at $\theta = 30^\circ$. The standard deviation of the experimental measurements is the thickness of the bullets if not shown as a vertical bar.

72

FIGURE 21: Measured (bullets) and calculated (lines) normalized transmission of a FS +100mm EFL PCX lens as functions of radial distance (r) for double-sided AR-coated BK7 lens (black), single-sided rARSS FS lens (red), and uncoated FS lens (blue). (a) TE and (b) TM incident polarization at $\theta = 0^\circ$. (c) TE and (d) TM incident polarization at $\theta = 15^\circ$. (e) TE and (f) TM incident polarization at $\theta = 30^\circ$. The standard deviation of the experimental measurements is the thickness of the bullets if not shown as a vertical bar.

73

FIGURE 22: Plots showing fractional transmission enhancement τ as a function of θ' for a θ of 0° , 15° , and 30° across all PCX lens samples; TE mode (squares), and TM mode (circles). The dashed line represents 3.6% transmission enhancement, the theoretical limit for normal incidence of FS.

77

FIGURE 23: Transmission enhancement as a function of the local angle θ' across all PCX lenses tested; TE-mode enhancement (squares) and TM mode (circles). The dashed line represents the theoretical limit +3.6% transmission enhancement for normal incidence of a FS planar surface. The red line represents the TE-mode theoretical enhancement for a single-sided ideal AR thin-film-coated planar substrate over the θ' range. The blue line represents the TM mode for the same computed parameters. The θ measurement set ranges are indicated as well.

78

FIGURE 24: Measured (bullets) and calculated (lines) normalized transmission of a FS $-50mm$ EFL PCX lens as functions of radial distance (r) for double-sided AR-coated BK7 lens (black), single-sided rARSS FS lens (red), and uncoated FS lens (blue). (a) TE and (b) TM incident polarization at $\theta = 0^\circ$. (c) TE and (d) TM incident polarization at $\theta = 15^\circ$. (e) TE and (f) TM incident polarization at $\theta = 30^\circ$. The standard deviation of the experimental measurements is the thickness of the bullets if not shown as a vertical bar.

FIGURE 25: Measured (bullets) and calculated (lines) normalized transmission of a FS $-75mm$ EFL PCX lens as functions of radial distance (r) for double-sided AR-coated BK7 lens (black), single-sided rARSS FS lens (red), and uncoated FS lens (blue). (a) TE and (b) TM incident polarization at $\theta = 0^\circ$. (c) TE and (d) TM incident polarization at $\theta = 15^\circ$. (e) TE and (f) TM incident polarization at $\theta = 30^\circ$. The standard deviation of the experimental measurements is the thickness of the bullets if not shown as a vertical bar.

FIGURE 26: Measured (bullets) and calculated (lines) normalized transmission of a FS $-100mm$ EFL PCX lens as functions of radial distance (r) for double-sided AR-coated BK7 lens (black), single-sided rARSS FS lens (red), and uncoated FS lens (blue). (a) TE and (b) TM incident polarization at $\theta = 0^\circ$. (c) TE and (d) TM incident polarization at $\theta = 15^\circ$. (e) TE and (f) TM incident polarization at $\theta = 30^\circ$. The standard deviation of the experimental measurements is the thickness of the bullets if not shown as a vertical bar.

FIGURE 27: Plots showing fractional transmission enhancement τ as a function of θ' for a θ of 0° , 15° , and 30° across all PCV lens samples; TE mode (squares), and TM mode (circles). The dashed line represents 3.6% transmission enhancement, the theoretical limit for normal incidence on FS.

FIGURE 28: Transmission enhancement as a function of θ' across all PCV lenses tested; TE-mode enhancement (squares) and TM mode (circles). The dashed line represents the theoretical limit +3.6% transmission enhancement for normal incidence of a FS planar surface. The red line represents the TE-mode theoretical enhancement for a single-sided ideal AR thin-film-coated planar substrate over the θ' range. The blue line represents the TM mode for the same computation parameters. The θ measurement set ranges are indicated as well.

- FIGURE 29: Fractional transmission enhancement as a function of θ' for non-optimized lenses. Enhancement data are shown with red indicating TE-mode polarization and blue indicating TM-mode polarization. 86
- FIGURE 30: Fractional transmission enhancement as a function of lens surface height at the measurement locations for both optimized and non-optimized lenses. Enhancement data for the optimized lenses are shown as transparent markers with red indicating TE-mode polarization and blue indicating TM-mode polarization. Enhancement data for non-optimized lenses are shown as solid markers with the same color indicators as for the optimized lenses. 86
- FIGURE 31: SEM images showing center, halfway between center and edge, and edge surface structure on $+50mm$ EFL lenses. The left column shows the optimized sample, and the right column shows the non-optimized sample. 87
- FIGURE 32: SEM images showing center, halfway between center and edge, and edge surface structure on $-50mm$ EFL lenses. The left column shows the optimized sample, and the right column shows the non-optimized sample. 88
- FIGURE 33: Experimental layout used to measure localized transmission of rARSS lens doublets: L, $+100mm$ EFL PCX lens that is focusing the incident beam to a $96 \mu m$ spot size at the front surface of the test lens; H, the test lens holder; L1, positive lens under test; RR, a retaining ring with a thickness of $2.0mm$; L2, negative lens under test; P, photodiode detector; C, data-collecting PC. H rests on a kinematic stage, allowing (a) translation along the vertical coordinate y and (b) rotation around the azimuth angle ϕ . 96
- FIGURE 34: Ray trace performed in OSLO of a $50mm$ EFL matched pair of BK7 lenses from the plano surface of the PCX lens to the detector plan. The images show the translated matched pair starting at the top with $0.0mm$ translation and moving down in $1.5mm$ increments to $9.0mm$. 99
- FIGURE 35: Simulated PSF of unobstructed beam at the detector surface. The PSF has been normalized to a value of 0.5235. 100

FIGURE 36: Point-spread functions (PSF) of 50mm EFL matched pairs, 101
 The images show the translated matched pair PSF starting at the top with 0.0mm translation and moving down in 1.5mm increments to 9.0mm . (a) BK7 PCX with BK7 PCV normalized to 0.4055, (b) BK7 PCX with FS PCV normalized to 0.3814, (c) FS PCX with BK7 PCV normalized to 0.4642, (d) FS PCX with FS PCV normalized to 0.4324.

FIGURE 37: Profile of beam with no test elements in beam path. The red 105
 line represents the measured beam profile, and the black line represents the computed beam spot size based on Gaussian propagation.

FIGURE 38: Measured (bullets) and calculated (lines) normalized trans- 107
 mission of a FS 50mm EFL PCX/PCV lens pair as functions of radial distance (r) for double-sided AR-coated BK7 PCV lens (black), single-sided rARSS FS PCV lens (red), and uncoated FS PCV lens (blue). (a) TE and (b) TM incident polarization for an AR-coated BK7 PCX lens. (c) TE and (d) TM incident polarization for a rARSS FS PCX lens. (e) TE and (f) TM incident polarization for an uncoated FS PCX lens. The standard deviation of the experimental measurements is the thickness of the bullets if not shown as a vertical bar.

FIGURE 39: Measured (bullets) and calculated (lines) normalized trans- 108
 mission of a FS 75mm EFL PCX/PCV lens pair as functions of radial distance (r) for double-sided AR-coated BK7 PCV lens (black), single-sided rARSS FS PCV lens (red), and uncoated FS PCV lens (blue). (a) TE and (b) TM incident polarization for an AR-coated BK7 PCX lens. (c) TE and (d) TM incident polarization for a rARSS FS PCX lens. (e) TE and (f) TM incident polarization for an uncoated FS PCX lens. The standard deviation of the experimental measurements is the thickness of the bullets if not shown as a vertical bar.

FIGURE 40: Measured (bullets) and calculated (lines) normalized trans- 109
 mission of a FS 100mm EFL PCX/PCV lens pair as functions of radial distance (r) for double-sided AR-coated BK7 PCV lens (black), single-sided rARSS FS PCV lens (red), and uncoated FS PCV lens (blue). (a) TE and (b) TM incident polarization for an AR-coated BK7 PCX lens. (c) TE and (d) TM incident polarization for a rARSS FS PCX lens. (e) TE and (f) TM incident polarization for an uncoated FS PCX lens. The standard deviation of the experimental measurements is the thickness of the bullets if not shown as a vertical bar.

FIGURE 41: Transmission efficiency of doublet lenses. Blue data are from AR-coated BK7 pairs, and red data are from rARSS pairs. The solid lines are from comparison computations for in-situ doublets, and the dashed lines are from constructed doublets (doublets formed from singlet transmission measurements). The lighter square/circle markers are from in-situ doublets, and the darker square/circle markers are from constructed doublets. The right column of plots are from TE-mode source polarization, and the left column of plots are from TM-mode source polarization. (a) and (b) are data from $50mm$ EFL lens pairs, (c) and (d) are from $75mm$ EFL lens pairs, and (e) and (f) are from $100mm$ EFL lens pairs.

FIGURE 42: Measured normalized beam spot sizes as a function of radial distance for $50mm$ EFL doublets. In each plot, AR-coated BK7 PCV lenses are shown as black squares, rARSS FS PCV lens samples are shown as red circles, and uncoated FS PCV lenses are shown as blue triangles. lighter markers indicate data evaluated using the Gaussian fit method, and darker markers indicate data using the FWHM method. Simulated data are shown as lines with the colors corresponding to the same PCV lenses as for the measured data. Dotted lines correspond to modeling performed in OSLO ray trace software. The top plot is for an AR-coated BK7 PCX lens, the middle plot is for a rARSS FS PCX lens, and the bottom plot is for an uncoated FS PCX lens.

FIGURE 43: Measured normalized beam spot sizes as a function of radial distance for $75mm$ EFL doublets. In each plot, AR-coated BK7 PCV lenses are shown as black squares, rARSS FS PCV lens samples are shown as red circles, and uncoated FS PCV lenses are shown as blue triangles. Lighter markers indicate data evaluated using the Gaussian fit method, and darker markers indicate data using the FWHM method. Simulated data are shown as lines with the colors corresponding to the same PCV lenses as for the measured data. Dotted lines correspond to modeling performed in OSLO ray trace software. The top plot is for an AR-coated BK7 PCX lens, the middle plot is for a rARSS FS PCX lens, and the bottom plot is for an uncoated FS PCX lens.

FIGURE 44: Measured normalized beam spot sizes as a function of radial distance for 100mm EFL doublets. In each plot, AR-coated BK7 PCV lenses are shown as black squares, rARSS FS PCV lens samples are shown as red circles, and uncoated FS PCV lenses are shown as blue triangles. Lighter markers indicate data evaluated using the Gaussian fit method, and darker markers indicate data using the FWHM method. Simulated data are shown as lines with the colors corresponding to the same PCV lenses as for the measured data. Dotted lines correspond to modeling performed in OSLO ray trace software. The top plot is for an AR-coated BK7 PCX lens, the middle plot is for a rARSS FS PCX lens, and the bottom plot is for an uncoated FS PCX lens. 116

FIGURE 45: "Sister" doublet configuration sample. A: PCX uncoated FS lens followed by a PCV AR-coated BK7 lens, B: PCX AR-coated BK7 lens followed by a PCV uncoated FS lens. 120

FIGURE 46: Measured beam spot sizes as a function of radial distance for mixtures of AR-coated BK7 lenses and uncoated FS lenses. Black square markers indicate AR-coated BK7 PCX lenses matched with uncoated FS PCV lenses. Red circle markers indicate uncoated FS PCX lenses and AR-coated BK7 PCV lenses. Lighter markers indicate data evaluated using the Gaussian fit method, and darker markers indicate data evaluated using the FWHM method. The top plot is for 50mm EFL lenses, the middle plot is for 75mm EFL lenses, and the bottom plot is for 100mm EFL lenses. 121

FIGURE 47: Measured beam spot sizes as a function of radial distance for mixtures of AR-coated BK7 lenses and rARSS lenses. Black square markers indicate AR-coated BK7 PCX lenses matched with rARSS PCV lenses. Red circle markers indicate rARSS PCX lenses and AR-coated BK7 PCV lenses. Lighter markers indicate data evaluated using the Gaussian fit method, and darker markers indicate data evaluated using the FWHM method. The top plot is for 50mm EFL lenses, the middle plot is for 75mm EFL lenses, and the bottom plot is for 100mm EFL lenses. 122

FIGURE 48: Measured beam spot sizes as a function of radial distance for mixtures of rARSS lenses and uncoated FS lenses. Black square markers indicate rARSS PCX lenses matched with uncoated FS PCV lenses. Red circle markers indicate uncoated FS PCX lenses and rARSS PCV lenses. Lighter markers indicate data evaluated using the Gaussian fit method, and darker markers indicate data evaluated using the FWHM method. The top plot is for $50mm$ EFL lenses, the middle plot is for $75mm$ EFL lenses, and the bottom plot is for $100mm$ EFL lenses.

LIST OF TABLES

TABLE 1: Seidel wavefront terms	48
TABLE 2: Rated uncertainty and tolerance for utilized equipment	54
TABLE 3: Specifications of lens samples. All values are given in mm. BK7 samples are AR-coated, FS samples are uncoated. R_1 is the curved-side radius of curvature, T_c is the center thickness, and T_e is the edge thickness.	58
TABLE 4: Mean percent difference of measured transmission values for planar substrates	75
TABLE 5: Mean percent difference of measured transmission values for PCX lens samples for TE polarization	75
TABLE 6: Mean percent difference of measured transmission values for PCX lens samples for TM polarization	75
TABLE 7: Mean percent difference of measured transmission values for PCV lens samples for TE polarization	83
TABLE 8: Mean percent difference of measured transmission values for PCV lens samples for TM polarization	83
TABLE 9: EFLs of doublet configurations	97
TABLE 10: Seidel wavefront errors for $+50mm$ EFL matched pairs	101
TABLE 11: Mean percent difference of measured transmission values for doublet lens samples for TE polarization	110
TABLE 12: Mean percent difference of measured transmission values for doublet lens samples for TM polarization	110
TABLE 13: Normalized size ranges for beam spot measurements for $75mm$ EFL matched pairs with an AR-coated BK7 PCX lens.	118
TABLE 14: Normalized size ranges for beam spot measurements for $75mm$ EFL matched pairs with a rARSS FS PCX lens.	118

TABLE 15: Normalized size ranges for beam spot measurements for $75mm$ EFL matched pairs with an uncoated FS PCX lens.	118
TABLE 16: Normalized size ranges for beam spot measurements for $100mm$ EFL matched pairs with an AR-coated BK7 PCX lens.	119
TABLE 17: Normalized size ranges for beam spot measurements for $100mm$ EFL matched pairs with a rARSS FS PCX lens.	119
TABLE 18: Normalized size ranges for beam spot measurements for $75mm$ EFL matched pairs with an uncoated FS PCX lens.	119
TABLE 19: Parameters of interest and values used to test and analyze transmission of rARSS on spherical surfaces.	126

CHAPTER 1: INTRODUCTION

1.1 Introduction to Random Anti-Reflection Surface Structures

Broad-band anti-reflection (AR) coatings are important to many optical systems, from power sensor windows to imaging. These are typically designed for a specified spectral range and peak transmission wavelength. Optical component performance can be improved by using complex multi-layer films [1, 2]. These can increase the spectral and angular bandwidth through careful layer thickness and index specification to the necessary performance level. With complexity come more design and manufacturing challenges, making multilayer AR thin film design a major area of investigation as well as a source of motivation for AR alternatives [3–15].

A major challenge to multilayer thin film design is the index of refraction specifications. Ideal materials needed in a design that do not exist in nature or cannot be manufactured must be dealt with by either adding a layer or set of layers with realistic indices. A simple loss of transmission at that location, in difficult cases such as microlens arrays (MLA), may be the only solution. The design of these multilayers is not trivial. For more complex multilayers where constraints may be too numerous, designers may have to take a more heuristic approach, rather than a computational one, in order to reduce reflections for a given substrate material and set of operating conditions [1].

Additionally, it is difficult to maintain thin film coating viability in harsh environments and high-power laser applications [6–9, 12, 13, 16–23]. The viability of a single layer is compounded in a multilayer design, and can become bulk mechanical and thermal failures. Some failures in these cases can be attributed to phenomena like layer index mismatch when operated far from optimum design conditions. Layer index mismatch can cause unwanted reflections between layers to accumulate and cause thermal damage. Systems where temperatures can fluctuate will also cause damage because of thermal expansion mismatch, resulting in delamination of the thin film layers from the substrate and other layers. The field effects of the EM wave on the film layers can also cause the layer to lose viability [24]. Node/anti-nodes in the thin films can also cause damage [25]. Laser sources incident on the film layers may create anti-nodes in layers when operating at a wavelength or angle-of-incidence (AOI) different from design parameters. This will result in an absorption of laser energy in the layer and eventual irreparable damage to the multilayer itself. It is due to this result that many AR multilayer coatings suffer from low laser-induced damage threshold (LIDT), making them unsuitable for high-power laser applications.

In mathematical simulations of AR thin film designs, it has been shown an subwavelength inhomogeneous thin film to be a comparable (and in some cases superior) alternative to traditional homogeneous thin films [15]. These inhomogeneous thin films act as a gradient index layer. The incident wave intercepts more of the film material as it travels to the substrate material, thereby observing the average index to gradually increase to that of the substrate. One physical interpretation of these inhomogeneous thin films are AR structured surfaces, or ARSS, where the inhomogeneous thin film

elements are etched from the substrate material itself. The advantages of these types of structures have been reported on in many works [5–9, 11–13, 16, 17, 19, 21, 26–32]. Shapes of these elements include 1D binary gratings, square columns, and tapered pillars, the last of which has been shown to have the best performance for AR applications. These elements maintain high transmission for wide AOI, from 0° to $\pm 30^\circ$. Due to the subwavelength size of these features, there are no diffractive effects present in the resulting transmitted wave. ARSS also have reported high broadband capabilities.

ARSS are especially promising as well for use in environments where a thin film coating would not maintain integrity due to the nature of fabrication [5, 8, 9, 23, 32]. The structure, having been etched directly from the substrate material, possesses a higher durability than thin films due to lack of thermal and mechanical mismatching between the film materials and the substrate. Many of the same specific issues that plague thin films do limit the functionality or stability of ARSS.

While the majority of investigation concerning ARSS is on periodic ordered structures, work on randomly sized and arranged structures is becoming more prevalent [7, 10, 29, 32–37]. The major advantage to using random structures is the ease of fabrication. Unlike periodic surface structures, many rARSS fabrication methods do not require a lithographic masking step in fabrication, making rARSS simpler to implement directly on the optical elements. The design of rARSS is also simpler, as there is no need to determine geometry prior to fabrication, making the optimization of etching parameters the primary design portion.

Currently, rARSS are highly optimized and well-characterized for planar optical

interfaces and elements [33, 34]. Optical elements with non-planar surfaces, such as lenses, can increase their spectral and field-of-view (FOV) performance through the implementation of rARSS on these surfaces [38, 39]. Multi-element optical systems contain spherical, aspherical and/or other curved interfaces, which traditionally have multilayered AR coatings with limiting spectral specifications or high cost. Multi-layered AR coated lenses have angular incidence sensitivity, since the optical path difference (OPD) changes through the coating layers, as a function of AOI. In addition, multi-layered AR-coated lenses are challenging to manufacture due to their non-planar surface topography, especially if radii of curvature are short and have low $F/\#$. Lenses with rARSS may have increased spectral and angular bandwidth, comparable to traditional broadband AR coatings. Structuring the surfaces of such elements with rARSS can result in extending their bandwidth of performance and FOV functionalities. Treating a lens with rARSS may also be carried out with more ease and less resource cost than a traditional multilayer coating.

1.2 Fabrication of Surface Structure

Anti-reflection surface structures, both ordered and random, have been fabricated using a number of different processes in other work. The fabrication process consists of two main stages, a writing stage and an etching stage. The writing stage is where a mask is applied to direct the etching process in creating an ARSS. Common writing processes include electron-beam lithographic writing [9, 12, 13, 17, 28, 30, 40] and holographic writing [13, 28]. The etch process can be of two major varieties, a wet etch [16] or a dry etch, of which there are several types. Common dry etch pro-

cesses include reactive-ion etching (RIE) [7,8,13,17,28,30,41–44], inductively-coupled plasma etching (ICP) [28,36], and fast-atom beam etching (FAB) [9,12,13,26]. RIE and ICP processes were used to create rARSS in this work, and will be discussed in greater detail.

It is important to note a couple of methods that do not follow the write-etch process. One of the most common is imprinting/embossing [10,11,21,27–29,31,45], where the initial write-etch process is used on a master and then stamped onto a secondary material, most likely a optical polymer. Another common method is UV curing [28], where a sol-gel is deposited and cured in such a way as to create surface structures. Both of these methods have advantages in industry due to being more easily transferable to a mass-production process, but often do not produce high resolution copies.

RIE and ICP are types of dry plasma etching [46–50]. This technique is a non-contact process, as opposed to wet chemistry etching. Wet chemistry etching is a process by which substrates are immersed into a specific chemistry. It is useful for designs requiring an isotropic process, or a process where material is removed on all surfaces in contact with the chemistry at similar removal rates. It is difficult, however, to use this process in developing closely-packed micron and nanometer scale semiconductor devices, in particular integrated circuits (IC), due to the isotropic nature of wet etching. In the late 1960s and early 1970s, dry plasma etching was developed as an anisotropic process, or a process where the etch is highly-directionalized, typically in top-down configuration. Dry plasma etching allowed for minimum size limits for modern ICs to shrink and is a common manufacturing tool in semiconductor device

production today.

Dry plasma etching chambers differ between manufacturers, but all share similar characteristics. Two parallel plates act as electrodes, with a chamber between, usually at low vacuum. A gas chemistry is present, predominately a fluorine or chlorine mixture, and is designed to chemically interact with a given substrate and/or mask placed in the chamber. As power is applied, the electrodes arc and provide collision mechanics necessary to etch out the material of the substrate. RIE processes specifically have an RF-powered bottom plate on which the substrate material is placed, while the top plate is grounded. The different charge densities on each plate causes the arc process to proceed. ICP is similar to the RIE configuration with the addition of multiple coil generators. These additional generators act to drive the plasma in the chamber to a higher density, thus producing faster etch rates. Each method can and does produce rARSS structure capable of high transmission under the same test constraints.

For this work, uncoated fused silica (FS) plano-convex (PCX) and plano-concave (PCV) spherical lenses were etched in a ICP/RIE process to create rARSS on the curved surface side. The lens samples were sputtered with a thin Au layer prior to the etching process in an AJA International ATC 1800-F sputter deposition system. This layer functioned as a partial non-patterned mask. In order to create a Au layer optimized for the design wavelength and substrate material on a planar surface, the parameters for length of sputtering, power, and stage rotation were developed. The etching process variables were previously optimized for broadband transmission enhancement from 500 to 1100 nm, reducing the Fresnel reflectivity of a single planar

surface to a value lower than 0.5% [51, 52]. To test optimization, ellipsometry (J. J. Woollam IR Vase System) was used to verify broadband transmission and AOI performance. Two etching systems were used to create the lens samples. For optimized samples, a Plasma-Therm RIE 7000 unit was used. The parameters used to optimize for maximum transmission on planar substrates were electrode power, time length of etch, chamber pressure, gas chemistry and flow rate. For non-optimized samples, a Surface Technology System (STS) III-V ICP Compound Semiconductor Etch System was used. The process parameters used for this system include power of the coil and of the electrode, time length of etch, chamber pressure, gas chemistry and the flow rate. In both systems, a fluorine gas chemistry is used. Due to the proprietary nature of the processes developed in the course of this work, variable values cannot be shared.

The lens set consisted of three 25.4mm diameter PCX of effective focal lengths (EFL) of +50mm, +75mm, and +100mm, and three matching PCV lenses of same diameter and negative respective focal lengths. More information concerning lens parameters can be found in Chapter 2. Two round planar FS substrates (UV-grade, Corning HPFS 7980) [53], 25.4mm in diameter, were also etched alongside the lens set as controls. The transmission test wavelength was chosen at 633nm (HeNe laser), and the transmission of the control samples was measured to confirm the rARSS process fidelity, as shown in Fig. 1.

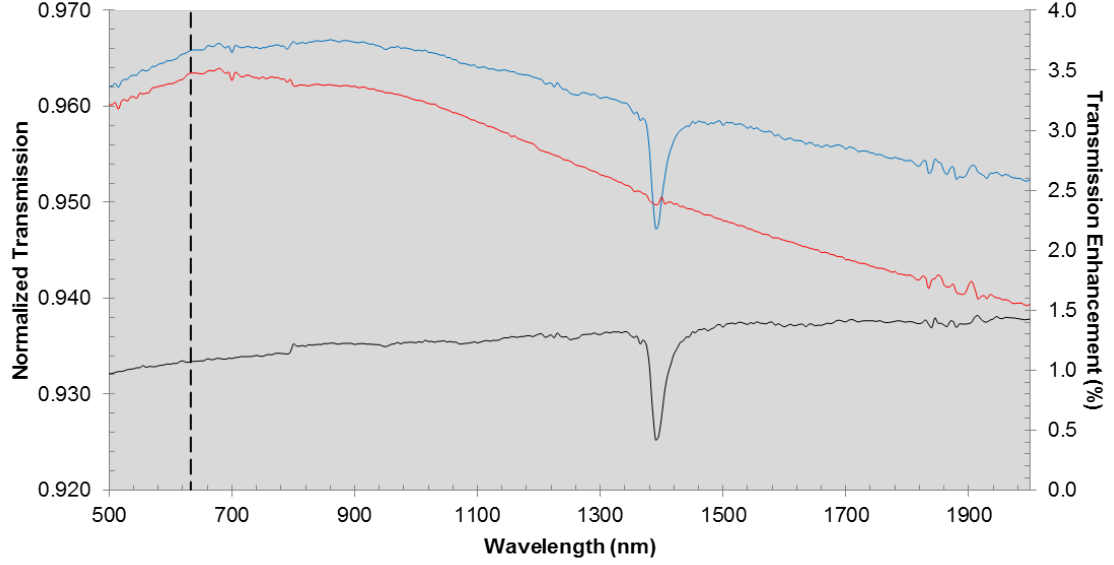


Figure 1: Measured transmission for FS over a wavelength range of 500nm to 2000nm . The black line is the transmission for planar fused silica (FS) with no rARSS, and the blue line is the transmission for planar FS with one side etched with rARSS for peak transmission at 633nm . The red line is the transmission enhancement of the rARSS sample over the unetched sample. The vertical dashed line indicates the design peak wavelength of 633nm . The dip in transmission around 1400nm is due to the absorption of water in the FS.

1.3 Performance Measurement Tools

The measurement of optical performance effects of rARSS on non-planar topology is necessary, since the etching processes used are anisotropic, and thus may vary across optical element surface topography. The fabrication and optimization of rARSS, on both planar and non-planar substrates, requires performance testing under multi-component optical system conditions. To test rARSS transmission performance on planar substrates, ellipsometric and spectroscopic methods are often used. Ellipsometry uses a focused beam on a single spot on the sample to generate angular and spectral bandwidth performance measurements. This single spot should be representative of the entire optical element under test. Conversely, spectrometers use a

large area of the surface to generate spectral performance measurements. The final performance is dependent on a signal averaging over the optical element surface.

Both of these methods, while useful for characterizing a planar surface, fail to provide an adequate performance measurement for rARSS on non-planar surfaces. A single-point transmission measurement on the surface of a spherical lens will not provide enough information to characterize the lens performance entirely; possible structure variations associated with the surface curvature would be missed. More detailed and in-depth performance characterization is required to characterize the dependence of the structure roughness parameters to the steepness of the etched profile. There has been some prior research reported, identifying possible testing solutions for characterization of rARSS on curved surfaces. Previous investigations show the viability of using multiple single point measurements over the component profile, in order to give a measurement indicative of overall performance [36–38]. An extensive test to establish the methodology of such a procedure would be useful to future investigations of rARSS optical effects on curved surfaces.

Curved surfaces with rARSS also provide an opportunity to study the transmission performance as a function of AOI and surface profile location. In the work [36], there is an indication of performance maintenance over the surface for various AOI, but no extensive parameterization was reported. To better understand the relationship between performance, AOI, and the test location on the optical surface, a full study of surface performance must be completed. Furthermore, elements with non-planar topography often change the power distribution and wavefront of the exiting beam due to their non-unity function. For example, lens elements are often used in optical

trains in order to shape Gaussian and Bessel beam profiles. A reasonable expectation of a user is to produce the same wavefront and profile with a lens using rARSS as would be with a conventional multilayer coating. Thus, a characterization of transmission alone does not fully define how rARSS would affect an elements functionality. To produce and improve rARSS treatments for non-planar surfaces, both new beam and transmission performance methodologies are needed.

1.4 Transmission Analysis of Random Anti-Reflection Surface Structure on Singlet Lenses

1.4.1 Transmission Determination of Untreated Lenses

To determine the transmission for an optically-thick PCX or PCV lens without AR surface structures or AR coatings, the Fresnel equations and the exact transmission solution for an optically-thick slab are applied [54]. The Fresnel equations for the reflection and transmission coefficients at a single boundary separating two media with optic indices n_1 and n_2 are

$$r_s = \frac{n_1 \cos \theta_i - n_2 \cos \theta_t}{n_1 \cos \theta_i + n_2 \cos \theta_t}, \quad (1)$$

$$r_p = \frac{n_2 \cos \theta_i - n_1 \cos \theta_t}{n_1 \cos \theta_t + n_2 \cos \theta_i}, \quad (2)$$

$$t_s = \frac{2n_1 \cos \theta_i}{n_1 \cos \theta_i + n_2 \cos \theta_t}, \quad (3)$$

$$t_p = \frac{2n_1 \cos \theta_i}{n_1 \cos \theta_t + n_2 \cos \theta_i}, \quad (4)$$

where r_s and t_s are the reflection and transmission coefficients for polarization perpendicular to the plane of incidence, and r_p and t_p conversely represent reflection and transmission coefficients for polarization parallel to the plane of incidence. The vari-

angles θ_i and θ_t are the incident and transmission angles at the interface. In general, $t_s = 1 - r_s$, but $t_p \neq 1 - r_p$. This formulation assumes no absorption and scattering losses. Reflectance, R_j , is then calculated as

$$R_j = |r_j|^2, \quad (5)$$

where the index j corresponds to either the s - or p -polarized component. This relationship does not hold true with transmission, T_j ; however, once R_j is known, T_j can be found by the use of

$$T_j = 1 - R_j. \quad (6)$$

Thus, it is often more useful to express T_j in terms of the reflection coefficient r_j :

$$T_s = 1 - \left| \frac{n_1 \cos \theta_i - n_2 \cos \theta_t}{n_1 \cos \theta_i + n_2 \cos \theta_t} \right|^2, \quad (7)$$

$$T_p = 1 - \left| \frac{n_2 \cos \theta_i - n_1 \cos \theta_t}{n_1 \cos \theta_t + n_2 \cos \theta_i} \right|^2. \quad (8)$$

As a ray propagates through an interface, the refracted angle with respect to the surface normal is found by use of Snells law,

$$n_1 \sin \theta_i = n_2 \sin \theta_t. \quad (9)$$

Using this relation, the transmitted angle, and thus the transmission for each polarization component, can be calculated for a planar interface.

For a curved interface, such as the surface of a spherical lens, further consideration must be taken to account for the change of the local incidence angle at a given distance from the apex. Generally, the optic axis is rotated to handle the case of a marginal

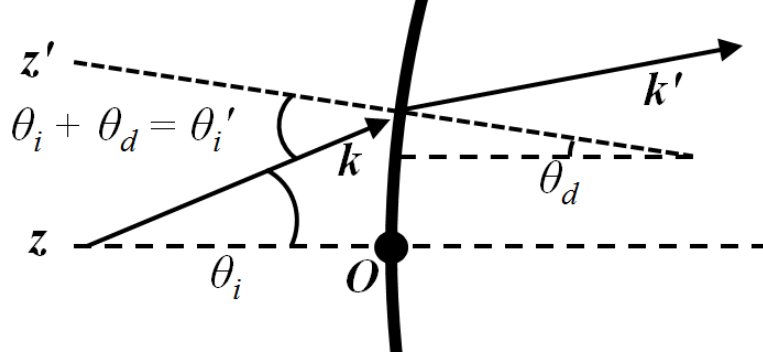


Figure 2: A section of a spherical surface with a ray, k , incident at a non-zero angle θ_i with respect to the optical axis z . A location of interest away from the apex of the surface experiences a further angular deviation, θ_d . A new axis normal to the curved surface, z' , is then used as the reference of z to determine θ_i' .

ray incident at the specific polar angle. The arrangement of this is shown in Fig. 2. The optical axis, z , and the axis normal to the curved surface at the incidence point, z' , have an angular separation of θ_d . This angle, along with the original incidence angle of the ray vector \vec{k} with respect to z , add to the value θ_i' . This angle is then used to calculate the transmission angle and the transmittance itself.

Calculating the angle θ_d of any curved surface requires knowledge of its surface function,

$$s(r) = \frac{r^2}{R(1 + \sqrt{1 - (1 + \kappa)\frac{r^2}{R^2}})} + \alpha_1 r^2 + \alpha_2 r^4 + \alpha_3 r^6 + \dots, \quad (10)$$

where $s(r)$ is the translational sag of the surface a distance r from the optic axis, R is the radius of curvature of the axially symmetric quadric surface and κ is its conic constant [55]. The coefficients $\alpha_1 \dots \alpha_n$ describe the curvature as it deviates away from the reference sphere. In the special case of a spherical lens, shown in Fig. 3, the factors κ and $\alpha_1 \dots \alpha_n$ go to zero and the expression reduces to

$$s(r) = R - \sqrt{R^2 - r^2}, \quad (11)$$

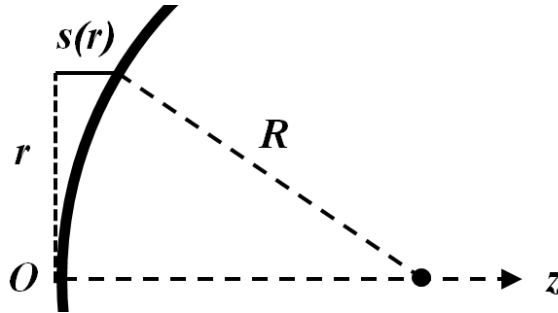


Figure 3: Spherical lens surface sag. $s(r)$ represents the sag of the lens at a distance r from the apex of the lens. R represents the radius of curvature; in the special case of a spherical lens, it is equivalent to the focal length of the front surface.

where R now represents the front focal length of the lens.

Once the sag is determined, the angle between the surface normal and the optic axis can be found through a trigonometric relationship. Using the tangent relationship, the angle is calculated using

$$\theta_d = \tan^{-1} \frac{r}{R - s(r)}. \quad (12)$$

The final angle as seen by the surface is then

$$\theta_{i'} = \theta_i + \theta_d. \quad (13)$$

Plots showing the local angles for each lens sample can be found in Fig. 4.

Using this method, the transmission through the first surface can be found at any point along the spherical boundary. The second surface transmission, since it is planar, only requires a rotation back to the original propagation axis to determine the incidence angle. The back surface transmission angle is then produced by Snell's law, and the Fresnel equations can be applied again.

The total transmission is the product of these two surface transmissions,

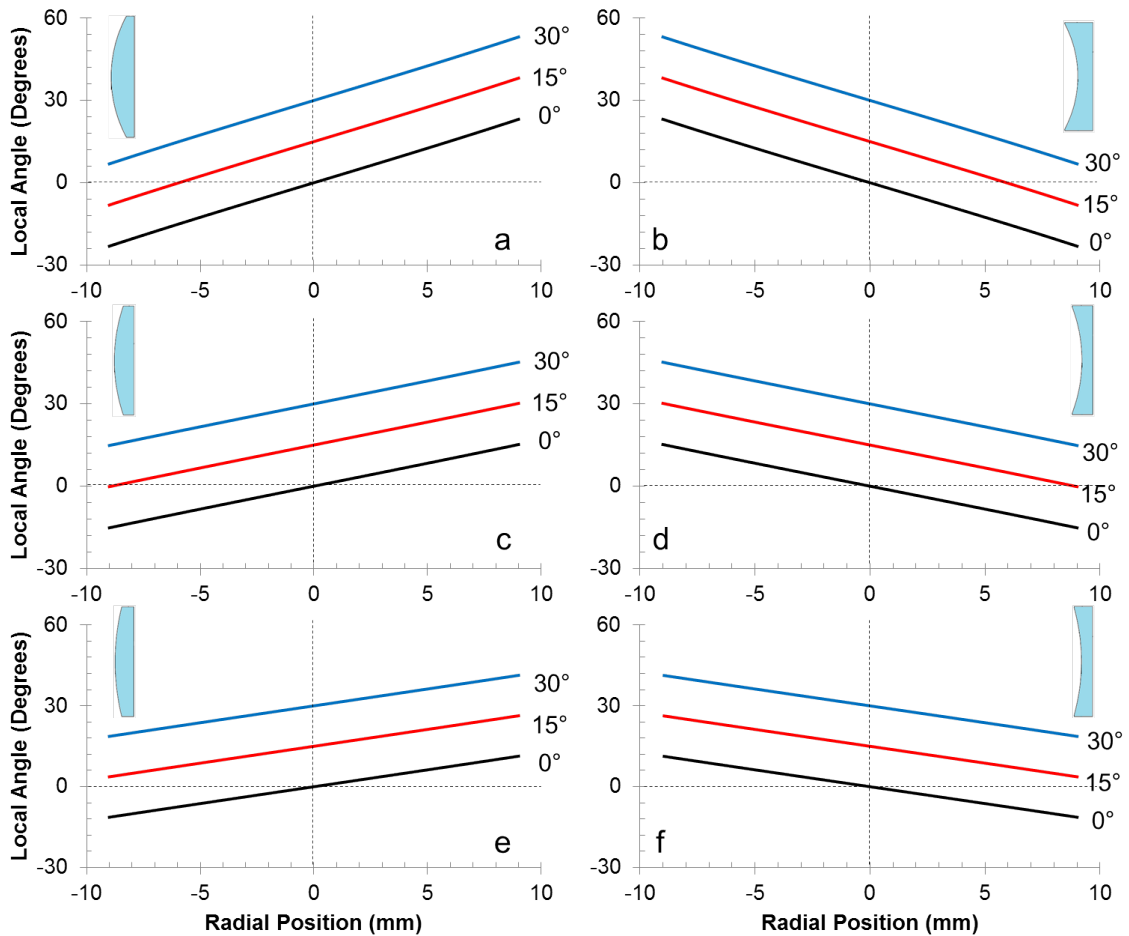


Figure 4: Global and corresponding local angle values over the convex surfaces of PCX and PCV FS test lenses: (a) $+50\text{mm}$ EFL, (b) -50mm EFL, (c) $+75\text{mm}$ EFL, (d) -75mm EFL, (e) $+100\text{mm}$ EFL, (f) -100mm EFL. A graphic of the corresponding lens is shown in each plot. For each, the black line is the 0° global angle, the red line is the 15° global angle, and the blue line is the 30° global. For a given global angle over a clear aperture of 18mm , the local angle has a range of over 45° .

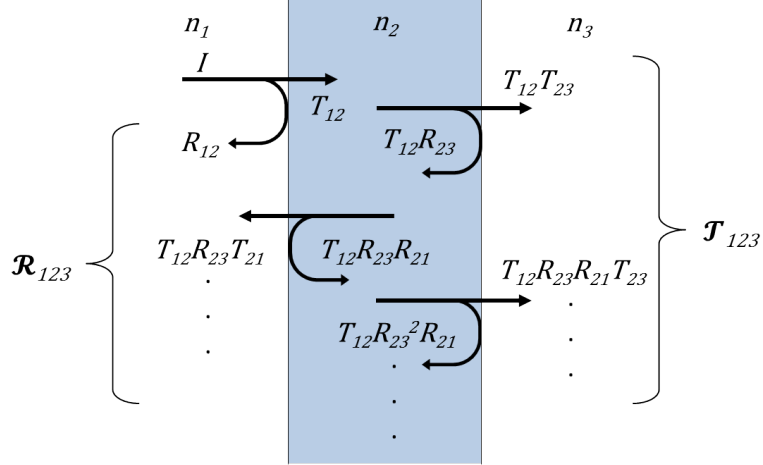


Figure 5: Total intensity transmission for a parallel-surface single slab showing the effect of summing multiple internal incoherent reflections.

$$T_{total} = T_{12}T_{23}, \quad (14)$$

where T_{12} is the transmission through the first surface from incident medium into the substrate, and T_{23} is the transmission through the second surface from the substrate to the exiting medium. The individual transmission values can be found using the appropriate Fresnel transmission defined in equation 7 for s-polarization or equation 8 for p-polarization.

In the case of optically-thick, slab-like elements, multiple internal reflections can arise resulting in a higher output than simply the product of the two surface transmissions (Fig 5). Each transmission that emerges from the second surface as a result of an internal reflection has the form

$$T_m = T_{12}T_{23}(R_{23}R_{21})^m, \quad (15)$$

where m is the number of round-trip internal reflections, ranging from $m = 0$ for the

first transmission, a result of no internal reflections, to $m = \infty$. The total transmission is then the following infinite sum:

$$T_{total} = T_{12}T_{23} \sum_{m=0}^{\infty} (R_{23}R_{21})^m. \quad (16)$$

If $R_{12}R_{23} \ll 1$, then the sum converges to a final form of

$$T_{total} = \frac{T_{12}T_{23}}{1 - R_{23}R_{21}}. \quad (17)$$

Since it is more straightforward to use two variables rather than four, the expression can be re-expressed in terms of transmission only:

$$T_{total} = \frac{T_{12}T_{23}}{1 - (1 - T_{23})(1 - T_{12})}. \quad (18)$$

This is the general expression for total transmission through an optically-thick slab. Using this expression with the Fresnel equations produces the final transmission value for ray propagation at marginal incidence for an untreated spherical lens.

1.4.2 Transmission Determination of Anti-reflection Coated Lenses

For an AR coated spherical lens, determination of the transmission requires more examination than the untreated version. For instance, adding a thin film requires an analysis of interference effects. The number of surface interfaces has doubled from two to four. It is now required to consider a more general approach by propagating the wave transmission through the various media [54].

Before calculation of wave transmission, a simplification that can be made at this point is to assume a sufficiently small incident wave profile such that the curved interface of the lens surface can be approximated as a planar interface. The lens

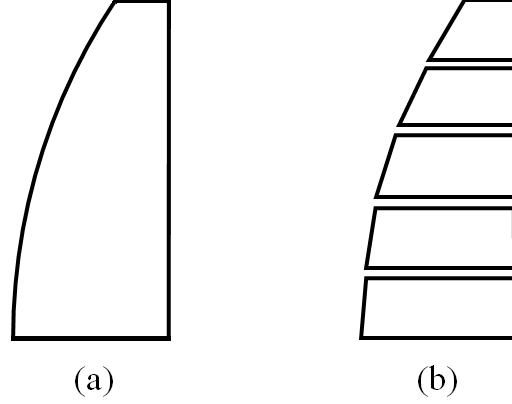


Figure 6: Representation of spherical surface as adjacent planar trapezoid segments. (a) Spherical surface to be modeled, (b) trapezoidal arrangement condensing surface to planar segments. If an incident wave possesses a sufficiently small profile, then the simpler trapezoidal model can be used to determine transmission through the element as a whole.

surface can then be treated as a series of trapezoids (Fig. 6). Thus, small curvatures over the propagation area can be ignored and the more straight-forward model of planar stratified media can be used. A final assumption is no scattering or absorption losses will be present in the system.

To begin, formalism is given in order to describe the wave as it travels through each interface. The Maxwell equations are the starting point. The equations formulated for travel through an isotropic material with no other sources are the most appropriate.

These are:

$$\epsilon \vec{\nabla} \cdot \vec{E} = 0, \quad (19)$$

$$\vec{\nabla} \times \vec{E} = \frac{i\omega\mu}{c} \vec{H}, \quad (20)$$

$$\vec{\nabla} \cdot \vec{H} = 0, \quad (21)$$

$$\vec{\nabla} \times \vec{H} = -\frac{i\omega\epsilon}{c} \vec{E}. \quad (22)$$

In this representation, \vec{E} represents the electric field and \vec{H} represents the magnetic field in the material. The variables ε and μ represent the permittivity and permeability, respectively. These will be considered functions of distance traveled into a medium in anticipation of managing transmission through a stratified media such that

$$\varepsilon = \varepsilon(z), \mu = \mu(z), \quad (23)$$

where z is the axis of propagation. Finally, ω is the angular frequency of the wave in the medium and c is the speed of light in vacuum.

For this investigation, the source is a linearly-polarized wave. Given a Cartesian coordinate system arranged such that z is in the direction of propagation, and y is in the plane of propagation, then a linearly-polarized transverse electric (TE) field will oscillate in the $x - z$ plane. Likewise, a linearly-polarized transverse magnetic (TM) field will oscillate in the $y - z$ plane. Since different results will be obtained from TE and TM polarizations, it is necessary to consider both. Starting with the TE case,

$$\vec{E} = E_x \hat{x}, E_y = E_z = 0. \quad (24)$$

Applying these to the Maxwell equations, the scalar relations are then

$$\frac{\partial H_z}{\partial y} - \frac{\partial H_y}{\partial z} + \frac{i\omega\varepsilon}{c} E_x = 0, \quad (25)$$

$$\frac{\partial H_x}{\partial z} - \frac{\partial H_z}{\partial x} = 0, \quad (26)$$

$$\frac{\partial H_y}{\partial x} - \frac{\partial H_x}{\partial y} = 0, \quad (27)$$

$$\frac{i\omega\mu}{c} H_x = 0, \quad (28)$$

$$\frac{\partial E_x}{\partial z} - \frac{i\omega\mu}{c} H_y = 0, \quad (29)$$

$$\frac{\partial E_x}{\partial y} + \frac{i\omega\mu}{c} H_z = 0. \quad (30)$$

A scalar expression in terms of E_x can be derived from these relations:

$$\frac{\partial^2 E_x}{\partial y^2} + \frac{\partial^2 E_x}{\partial z^2} + n^2 k_0^2 E_x = \frac{d(\ln \mu)}{dz} \frac{\partial E_x}{\partial z}. \quad (31)$$

In this expression, factors of ε , μ , ω , and c have been represented as index n and wavenumber k using the relations

$$n^2 = \varepsilon\mu, \quad (32)$$

and

$$k_0 = \frac{\omega}{c}. \quad (33)$$

To solve this differential equation, the term E_x can be expressed as a product of individual functions of y and z :

$$E_x(y, z) = Y(y)U(z). \quad (34)$$

Subsequent substitution of this trial function into equation 31 and isolating factors of y and z produce

$$\frac{1}{Y} \frac{d^2 Y}{dy^2} = -\frac{1}{U} \frac{d^2 U}{dz^2} - n^2 k_0^2 + \frac{d(\ln \mu)}{dz} \frac{1}{U} \frac{dU}{dz}. \quad (35)$$

In order to solve equation 35, each side of the expression must be equal to a constant.

An appropriate choice is K^2 , where this factor can be set to

$$K^2 = k_0^2 \alpha^2, \quad (36)$$

producing a functional form of

$$Y(y) = Ae^{ik_0\alpha y}, \quad (37)$$

where A is an amplitudinal constant and α is a factor yet to be determined. Thus, the functions of E_x , H_y , and H_z are defined more explicitly as

$$E_x = U(z)e^{i(k_0\alpha y - \omega t)}, \quad (38)$$

$$H_y = V(z)e^{i(k_0\alpha y - \omega t)}, \quad (39)$$

$$H_z = W(z)e^{i(k_0\alpha y - \omega t)}. \quad (40)$$

Through the application of equations 25, 29, and 30, relations between the functions of z can be constructed:

$$\frac{dV}{dz} = ik_0(\alpha W + \varepsilon U), \quad (41)$$

$$\frac{dU}{dz} = ik_0\mu V, \quad (42)$$

$$\alpha U + \mu W = 0. \quad (43)$$

Eliminating W from this system results in a pair of simultaneous first-order differential equations:

$$\frac{dU}{dz} = ik_0\mu V, \quad (44)$$

$$\frac{dV}{dz} = ik_0\left(\varepsilon - \frac{\alpha^2}{\mu}\right)U. \quad (45)$$

Separating factors of U and V creates the following set of second-order linear differential equations:

$$\frac{d^2U}{dz^2} - \frac{d(\ln \mu)}{dz} \frac{dU}{dz} + k_0^2(n^2 - \alpha^2)U = 0, \quad (46)$$

$$\frac{d^2V}{dz^2} - \frac{d[\ln(\varepsilon - \frac{\alpha^2}{\mu})]}{dz} \frac{dV}{dz} + k_0^2(n^2 - \alpha^2)V = 0. \quad (47)$$

Starting from the Maxwell equations once more for a wave with the form

$$\vec{H} = H_x \hat{x}, H_y = H_z = 0, \quad (48)$$

will produce the corresponding results for the TM polarization case. Upon arriving at the expressions analogous to equations 46 and 47, the only differences between these will be the swapped uses of ε and μ . Thus, for any solutions of wave propagation through a medium using this formalism, one can find the TM case if the TE case is known and vice versa by simply exchanging the permittivity and permeability coefficients.

Equations 38 - 40 show that the functions of U , V , and W have the possibility of being complex, with phase factor $\phi(z)$. If E_x is of constant amplitude, then

$$|U(z)| = \text{constant}, \quad (49)$$

and if of constant phase,

$$\phi(z) + k_0 \alpha y = \text{constant}. \quad (50)$$

Only in special cases does E_x possess both constant phase and amplitude. A way to take advantage of both of these properties is to first consider the case of infinitesimal displacement some dy , dx along the phase surface. It can then be said that

$$\phi'(z)dz + k_0 \alpha dy = 0, \quad (51)$$

and the angle this displacement makes with the original position is

$$\tan \theta = -\frac{dz}{dy} = \frac{k_0 \alpha}{\phi'(z)}. \quad (52)$$

Then, a homogeneous plane wave, which has constant amplitude across the wavefront, will have phase of the form

$$\phi(z) = k_0 n z \cos \theta. \quad (53)$$

Using this expression with equation 52, one finds that

$$\alpha = n \sin \theta, \quad (54)$$

implying that this factor is a constant for this special case. Thus, both U and V amplitudinal functions of equations 38 and 39 are now defined for a general homogeneous plane wave. A system can then be constructed to propagate the field forward through a media interface.

The coupled solutions of the functions U and V can be expressed satisfying equations 46 and 47. A system can be created to express these in a general form:

$$\frac{dU_1}{dz} = ik_0 \mu V_1, \quad (55)$$

$$\frac{dV_1}{dz} = ik\left(\varepsilon - \frac{\alpha^2}{\mu}\right)U_1, \quad (56)$$

$$\frac{dU_2}{dz} = ik_0 \mu V_2, \quad (57)$$

$$\frac{dV_2}{dz} = ik\left(\varepsilon - \frac{\alpha^2}{\mu}\right)U_2. \quad (58)$$

Thus

$$V_1 \frac{dU_2}{dz} - V_2 \frac{dU_1}{dz} = 0, \quad (59)$$

and

$$U_1 \frac{dV_2}{dz} - U_2 \frac{dV_1}{dz} = 0. \quad (60)$$

Combining and simplifying these produces the expression

$$\frac{d}{dz}(U_1 V_2 - U_2 V_1) = 0. \quad (61)$$

If this function was then expressed in matrix form, then

$$D = \begin{vmatrix} U_1 & V_1 \\ U_2 & V_2 \end{vmatrix}. \quad (62)$$

would imply that the determinant is a constant, and thus invariant. To determine appropriate solutions, the matrix elements can be expressed as functions of z :

$$U_1 = f(z), \quad (63)$$

$$U_2 = F(z), \quad (64)$$

$$V_1 = g(z), \quad (65)$$

$$V_2 = G(z), \quad (66)$$

such that

$$f(0) = G(0) = 0 \quad (67)$$

and

$$F(0) = g(0) = 1. \quad (68)$$

Finally, solutions at $z = 0$ have amplitude

$$U(0) = U_0, \quad (69)$$

$$V(0) = V_0, \quad (70)$$

producing solutions of U and V :

$$U = FU_0 + fV_0, \quad (71)$$

$$V = GU_0 + gV_0. \quad (72)$$

In matrix notation, this system can be expressed as

$$\overleftarrow{Q} = \overleftarrow{N}\overleftarrow{Q}_0 \quad (73)$$

where

$$\overleftarrow{Q} = \begin{bmatrix} U(z) \\ V(z) \end{bmatrix}, \overleftarrow{Q}_0 = \begin{bmatrix} U_0 \\ V_0 \end{bmatrix}, \overleftarrow{N} = \begin{bmatrix} F(z) & f(z) \\ G(z) & g(z) \end{bmatrix}. \quad (74)$$

Alternately, U_0 and V_0 can be expressed in terms of $U(z)$ and $V(z)$:

$$\overleftarrow{Q}_0 = \overleftarrow{M}\overleftarrow{Q}, \quad (75)$$

where

$$\overleftarrow{M} = \overleftarrow{N}^{-1} = \begin{bmatrix} g(z) & -f(z) \\ -G(z) & F(z) \end{bmatrix}. \quad (76)$$

This matrix is considered the characteristic matrix of a layer or layers in a stratified medium. Thus, the wave at some arbitrary distance along the z -axis can be found.

The characteristic matrix of interest is that of a single dielectric layer. First, considering a homogeneous layer:

$$\varepsilon = \mu = \text{constant}. \quad (77)$$

This reduces the second-order differential equations 46 and 47, along with equation 54

to

$$\frac{d^2U}{dz^2} + (k_0^2 n^2 \cos^2 \theta)U = 0, \quad (78)$$

$$\frac{d^2V}{dz^2} + (k_0^2 n^2 \cos^2 \theta)V = 0, \quad (79)$$

General solutions of these more condensed expressions are

$$U(z) = A \cos(k_0 n z \cos \theta) + B \sin(k_0 n z \cos \theta), \quad (80)$$

$$V(z) = \frac{1}{i} \sqrt{\frac{\varepsilon}{\mu}} \cos \theta [B \cos(k_0 n z \cos \theta) - A \sin(k_0 n z \cos \theta)]. \quad (81)$$

Applying the boundary conditions 67 and 68 to 63 - 66 produces the solutions

$$U_1 = f(z) = \frac{i}{\cos \theta} \sqrt{\frac{\varepsilon}{\mu}} \sin(k_0 n z \cos \theta), \quad (82)$$

$$V_1 = g(z) = \cos(k_0 n z \cos \theta), \quad (83)$$

$$U_2 = F(z) = \cos(k_0 n z \cos \theta), \quad (84)$$

$$V_2 = G(z) = i \sqrt{\frac{\varepsilon}{\mu}} \cos \theta \sin(k_0 n z \cos \theta). \quad (85)$$

The characteristic matrix is thus

$$\overleftrightarrow{M}_{TE} = \begin{bmatrix} \cos(k_0 n z \cos \theta) & -\frac{i}{\cos \theta} \sqrt{\frac{\varepsilon}{\mu}} \sin(k_0 n z \cos \theta) \\ -i \sqrt{\frac{\varepsilon}{\mu}} \cos \theta \sin(k_0 n z \cos \theta) & \cos(k_0 n z \cos \theta) \end{bmatrix}. \quad (86)$$

This expression is for a TE incident wave. The TM case, described by equation 48,

is obtained from the TE case by an exchange of ε and μ . The re-expressed TM

characteristic matrix is then

$$\overleftrightarrow{M}_{TM} = \begin{bmatrix} \cos(k_0 n z \cos \theta) & -\frac{i}{\cos \theta} \sqrt{\frac{\mu}{\varepsilon}} \sin(k_0 n z \cos \theta) \\ -i \sqrt{\frac{\mu}{\varepsilon}} \cos \theta \sin(k_0 n z \cos \theta) & \cos(k_0 n z \cos \theta) \end{bmatrix}. \quad (87)$$

To find the reflected and transmitted amplitudes of a dielectric slab from the propagation matrix, the electric and magnetic field amplitudes must be defined. For a TE wave, the electric field amplitude before and after the slab can be generally given as

$$U_0 = I + R \quad (88)$$

and

$$U(z_{slab}) = T, \quad (89)$$

where I is the incident amplitude, R is the reflected amplitude, T is the transmitted amplitude, and z_{slab} is the thickness of the dielectric slab layer. The magnetic amplitudes can be derived from these using the relation

$$\vec{H} = \sqrt{\frac{\epsilon}{\mu}} \hat{s} \times \vec{E}, \quad (90)$$

along with the boundary conditions across the medium. This produces the magnetic field amplitudes

$$V_0 = p_1(I - R) \quad (91)$$

and

$$V(z = h) = p_n T, \quad (92)$$

where h is the thickness of the layer and p_1 and p_n are factors defined by the expression

$$p_l = \sqrt{\frac{\epsilon_l}{\mu_l}} \cos \theta_l, l = 0, 1, 2, \dots, q. \quad (93)$$

In this expression, l corresponds to the appropriate layer in the stratified media: ϵ_l and μ_l are material constants, and θ_l is the ray angle in the medium. Utilizing the

matrix relationship in equation 75, relative amplitude expressions can be constructed:

$$r = \frac{R}{I} = \frac{p_1(m_{11} + m_{12}p_n) - (m_{21} + m_{22}p_n)}{p_1(m_{11} + m_{12}p_n) + (m_{21} + m_{22}p_n)}, \quad (94)$$

$$t = \frac{T}{I} = \frac{2p_1}{p_1(m_{11} + m_{12}p_n) + (m_{21} + m_{22}p_n)}. \quad (95)$$

The factors m_{ij} are the elements of the propagation matrix. To express these elements more condensely, a factor, β , will be defined:

$$\beta = \frac{2\pi}{\lambda_0} n_2 h \cos \theta_2, \quad (96)$$

where λ_0 is the wavelength of the incident light in vacuum, n_2 is the index of the dielectric layer, and θ_2 is the ray angle in the dielectric layer. It will also be helpful to constrain the single-layer dielectric medium as homogeneous and non-magnetic.

Thus, $\mu = 1$. Adding these simplifications in, along with equation 93, the matrix is now

$$\overleftrightarrow{M} = \begin{bmatrix} \cos \beta & -\frac{i}{p_2} \sin \beta \\ -ip_2 \sin \beta & \cos \beta \end{bmatrix}. \quad (97)$$

Recalling the Fresnel formulae for a TE wave:

$$r_{ij} = \frac{n_i \cos \theta_i - n_j \cos \theta_j}{n_i \cos \theta_i + n_j \cos \theta_j}, \quad (98)$$

$$t_{ij} = \frac{2n_i \cos \theta_i}{n_i \cos \theta_i + n_j \cos \theta_j}, \quad (99)$$

where i is the incident material and j is the transmitted material. Using these and the relative amplitude expressions in equations 94 and 95, the relationship for the

reflection coefficient through the dielectric layer is

$$r = \frac{r_{12} + r_{23}e^{2i\beta}}{1 + r_{12}r_{23}e^{2i\beta}}. \quad (100)$$

Squaring the reflection coefficient produces the reflection intensity. As with the case of an untreated lens, it is often simpler to express the transmitted intensity in terms of reflection,

$$T = 1 - R. \quad (101)$$

Thus, the transmission through a dielectric film at the substrate layer is given by

$$T = 1 - |r|^2 = 1 - \frac{r_{12}^2 + r_{23}^2 + 2r_{12}r_{23} \cos 2\beta}{1 + r_{12}^2r_{23}^2 + 2r_{12}r_{23} \cos 2\beta}. \quad (102)$$

There has been no consideration so far for the thickness of the dielectric layer and choice of medium, producing the general expression above. Since the Fresnel formulae do not take interference into account, the factor β will be the only variable affected by layer thickness itself. Values of β are such that

$$\beta_m = \beta_0 + m\pi, m = 0, 1, 2, \dots \quad (103)$$

produces identical reflection and transmission values. Solving for height and choice of layer medium gives

$$n_2h = \frac{\beta + m\lambda_0}{2\pi \cos \theta_2}. \quad (104)$$

To simplify this expression further, the optimized case of the ideal AR thin film will be taken to operate under normal incidence. Thus, $\cos \theta_2 = 1$. Finally, finding the maximum or minimum of the reflection constrains $\beta = m\pi/2$. The medium and

thickness are then

$$n_2 h = \frac{m \lambda_0}{4}. \quad (105)$$

Values of h and n_2 cannot be 0, so m is now constrained to values of $1, 2, \dots$, but a choice of m will determine either a minimum or maximum. Odd values of m produce layers equivalent to multiples of a quarter of the wavelength in the medium, and even values of m produce layers equivalent to multiples of half. In the case of odd values of m ,

$$\cos 2\beta = -1, \quad (106)$$

and

$$R = \left(\frac{n_1 n_3 - n_2^2}{n_1 n_3 + n_2^2} \right)^2. \quad (107)$$

The reflection in this case can be suppressed by a choice of

$$n_2 = \sqrt{n_1 n_3}. \quad (108)$$

In the case of even m , the reflection intensity becomes

$$R = \left(\frac{n_1 - n_3}{n_1 + n_3} \right)^2. \quad (109)$$

There is no selection of the dielectric layer in this case to suppress all reflection.

Thus, the case producing an AR layer is a quarter-wave index-matched thin film. For

a general expression at any AOI,

$$\beta = \frac{\pi \cos \theta_2}{2}, \quad (110)$$

and substitution into equation 102 will produce the transmitted intensity. This same

model can be used to give any AR thin film transmission with general AOI, regardless of wavelength and material considerations, as long as the quarter-wave conditions are met in the physical element being modeled.

To find the transmission for the same constraints in the TM case, the only change need be made is the exchange of the Fresnel formulae to those for the TM case. The same quarter-wave index-matched layer will also be optimized for TM waves.

As a last note, there are, in cases where the incident source is Gaussian, Goos-Hänchen shifts manifesting as additional reflected orders if the AOI is non-normal [56, 57]. The reflected orders may not only change in terms of directionality, but also in intensity, and add non-trivial complexities to the present model. If the quarter-wave criteria for a thin film is kept, the changes in the reflected orders made by the shift cancel out, and the model can be used as is given in this section. For a more complex film geometry, this must be taken into account.

1.5 Transmission and Beam Profile Determination of Performance of Random Anti-Reflection Surface Structures on Doublet Lenses

1.5.1 Transmission Determination of Doublet Lenses

Much like the singlet lens samples, the transmission of the doublets were determined with the use of the Fresnel equations along with the exact transmission solution for an optically-thick slab. No new analytical tools are needed to expand the Fresnel equations for two lens rather than one; a simple propagation through the two additional surfaces is all that is necessary. To stitch these new transmission values together, an adjustment must be made to the total transmission expression.

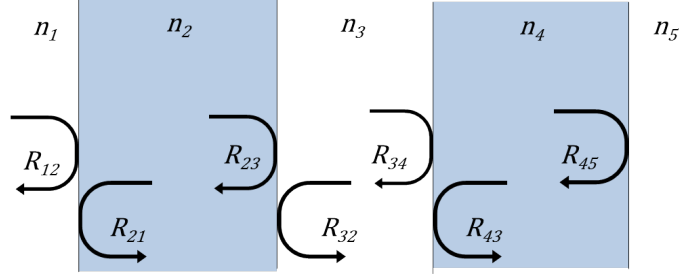


Figure 7: Doublet slab layout showing the additional surface reflections added by the second lens.

If all multiple reflections are assumed to make it to the detector, then the transmission expression for the two lenses would consist of the three infinite sums; two for each slab of substrate, and one for the "slab" of air separating the two lenses (Fig. 7). Again, assuming the multiple reflections are much less than unity, the sums converge, and the final form is

$$T_{total} = \frac{T_{12}T_{23}T_{34}T_{45}}{1 - (1 - T_{45})(1 - T_{34})(1 - T_{23})(1 - T_{12})}. \quad (111)$$

Using this expression along with the appropriate Fresnel expression for the given surface, the transmission through the doublet lenses can be calculated.

To evaluate cascading elements, the transmission efficiency can be used. The efficiency is defined as

$$eff = \frac{T_{L1+L2}}{T_{uncFS+uncFS}}, \quad (112)$$

where T_{L1+L2} is the transmission of two matched test lenses and $T_{uncFS+uncFS}$ is the transmission of two uncoated FS matched lenses. This expression mirrors that of the transmission enhancement analysis from Chapter 2.

1.5.2 Gaussian Beam Propagation Through Multi-Element Systems

A Gaussian beam is defined as a beam having a transverse spatial electromagnetic profile described by a Gaussian function distribution and is bounded as a paraxial wave. To define a generalized Gaussian beam, the paraxial wave equation must be established.

To begin, the general scalar wave equation is defined as

$$[\nabla^2 + k^2]\tilde{E}(x, y, z) = 0, \quad (113)$$

where \tilde{E} is the complex phasor amplitude of the wave containing a Ae^{-ikz} spatial function with a transverse profile in x and y [58, 59]. Physical wave effects, such as diffraction or propagation, will change the profile amplitude distribution. The wave can then be defined as having complex phasor amplitude

$$\tilde{E}(x, y, z) \equiv \tilde{u}(x, y, z)e^{-ikz}. \quad (114)$$

The function \tilde{u} is the complex scalar wave amplitude. Equation 114 is substituted into equation 113

$$[\nabla^2 + k^2][\tilde{u}(x, y, z)e^{-ikz}] = 0, \quad (115)$$

which then reduces to

$$\frac{\partial^2 \tilde{u}}{\partial x^2} + \frac{\partial^2 \tilde{u}}{\partial y^2} + \frac{\partial^2 \tilde{u}}{\partial z^2} - i2k \frac{\partial \tilde{u}}{\partial z} = 0. \quad (116)$$

The second order terms are the effects from diffraction, and the first order term is the effect from propagation.

The next step is to remove unneeded terms and orders for a paraxial system. Given a plane wave traveling paraxially in the x-z plane (that is, the ray propagation makes a small angle with respect to the z-axis), the complex phasor amplitude is given as

$$\tilde{E}(x, z) = \tilde{u}(x, z)e^{-ikz} = e^{-ikx \sin \theta - ikz \cos \theta}. \quad (117)$$

The complex scalar wave amplitude is then

$$\tilde{u}(x, z) = e^{-ikx \sin \theta - ikz(1 - \cos \theta)}. \quad (118)$$

Using the small angle approximation, equation 118 can be re-expressed as

$$\tilde{u}(x, z) \approx e^{-ikx\theta - \frac{ikz\theta^2}{2}}. \quad (119)$$

The z-dependent diffraction term will evolve more slowly than the z-dependent propagation term and the transverse plane diffraction terms. In order to compare terms to show this effect in equation 113, the normalized first and second derivatives are taken. The normalized first derivative is

$$\frac{-i2k}{\tilde{u}} \frac{\partial \tilde{u}}{\partial z} = 2k^2(1 - \cos \theta) \approx k^2\theta^2, \quad (120)$$

and the normalized second derivatives are

$$\frac{1}{\tilde{u}} \frac{\partial^2 \tilde{u}}{\partial x^2} = -k^2 \sin^2 \theta \approx -k^2\theta^2 \quad (121)$$

and

$$\frac{1}{\tilde{u}} \frac{\partial^2 \tilde{u}}{\partial z^2} = k^2(1 - \cos \theta)^2 \approx k^2 \frac{\theta^4}{4}. \quad (122)$$

For $\theta \leq 30^\circ$, the second-order θ terms will dominate the expression, and the fourth-

order term is negligible. Thus,

$$\left| \frac{\partial^2 \tilde{u}}{\partial z^2} \right| \ll \left| 2k \frac{\partial \tilde{u}}{\partial x} \right| \text{ or } \left| \frac{\partial^2 \tilde{u}}{\partial x^2} \right| \text{ or } \left| \frac{\partial^2 \tilde{u}}{\partial y^2} \right|. \quad (123)$$

The paraxially-approximated expression is now given as

$$\frac{\partial^2 \tilde{u}}{\partial x^2} + \frac{\partial^2 \tilde{u}}{\partial y^2} - i2k \frac{\partial \tilde{u}}{\partial x} = 0. \quad (124)$$

This can be re-expressed in a general form as

$$\nabla_t^2 \tilde{u}(\mathbf{s}, z) - i2k \frac{\partial \tilde{u}(\mathbf{s}, z)}{\partial z} = 0, \quad (125)$$

where subscript t refers to an operation on the transverse coordinates and \mathbf{s} is the transverse coordinate pair for a system of interest. Thus, a system is not restricted to Cartesian coordinates.

The paraxial approximation has been defined for a plane wave; the same assumptions will hold when developing a spherical wave. The next step is then to implement this system in order to create the Gaussian amplitudinal profile. A general spherical wave can be defined as

$$\tilde{E}(\mathbf{r}, \mathbf{r}_0) = \frac{e^{-ik\rho(\mathbf{r}, \mathbf{r}_0)}}{\rho(\mathbf{r}, \mathbf{r}_0)}, \quad (126)$$

where \tilde{E} is the field at point \mathbf{r} due to a point source located at \mathbf{r}_0 and ρ is the distance between these two points. In Cartesian coordinates,

$$\rho(\mathbf{r}, \mathbf{r}_0) \equiv \sqrt{(x - x_0)^2 + (y - y_0)^2 + (z - z_0)^2}. \quad (127)$$

To accommodate a paraxial system, this expression can be converted to a Taylor

series as a function of z

$$\rho(\mathbf{r}, \mathbf{r}_0) = z - z_0 + \frac{(x - x_0)^2 + (y - y_0)^2}{2(z - z_0)} + \dots \quad (128)$$

In order to drop the higher order terms, a paraxial system must be constructed. Given a wave with $\tilde{u}_1(x_1, y_1)$ at $z = z_1$ and $\tilde{u}_2(x_2, y_2)$ at $z = z_2 = z_1 + L$ where L is some distance propagated by the beam, the paraxial bounds would dictate the beam is confined to a finite width of $2a$. Thus, the transverse profiles of both \tilde{u}_1 and \tilde{u}_2 are negligible at transverse coordinates $x > a$ and $y > a$. In such a system, the exponential terms in equation 126 must be smaller than $\frac{\pi}{2}$ for higher-order Taylor series terms to be dropped. To describe this, the inequality

$$\left| \frac{k(x_2 - x_1)^4}{4(z_2 - z_1)^3} \right| \approx \left| \frac{k(2a)^4}{4L^3} \right| = \left| \frac{2\pi(2a)^4}{\lambda 4L^3} \right| \leq \frac{\pi}{2} \quad (129)$$

can be used. Through some algebraic rearrangement, a new constraint emerges, stating that

$$\left(\frac{2a}{\lambda} \right)^{\frac{1}{3}} \leq \frac{L}{2a}. \quad (130)$$

As long as the distance propagated by the beam is sufficiently large as compared to the beam width while simultaneously the wavelength is sufficiently small as compared to the beam width, higher-order terms can be dropped. For most physical beams, including the source and experimental arrangement used for this study, these constraints are met; the wavelength of the source used is 632.8 nm , the size of the beam width over the travel of the beam ranges from $\sim 100 \text{ }\mu\text{m}$ to nearly 1 mm , and the propagation distance of interest is 100 mm . A similar case can be made for dropping the quadratic terms in the denominator of equation 126.

The field is now

$$\tilde{E}(x, y, z) = \frac{e^{-ik(z-z_0) + \frac{(x-x_0)^2 + (y-y_0)^2}{2(z-z_0)}}}{z - z_0}. \quad (131)$$

As a result, the amplitude is

$$\tilde{u}(x, y, z) = \frac{1}{z - z_0} e^{-ik \left[\frac{(x-x_0)^2 + (y-y_0)^2}{2(z-z_0)} \right]}. \quad (132)$$

For the paraxial spherical wave, the wavefront at any point $z = z_0$ is an arc section of a sphere. Then the distance $z - z_0$ is the radius of curvature,

$$R(z) = z - z_0. \quad (133)$$

Substitution into the amplitude gives

$$\tilde{u}(x, y, z) = \frac{1}{R(z)} e^{-ik \left[\frac{(x-x_0)^2 + (y-y_0)^2}{2R(z)} \right]}. \quad (134)$$

The phase of this wave can then be defined as

$$\phi(x, y, z) \equiv k \frac{(x-x_0)^2 + (y-y_0)^2}{2(z-z_0)} = \frac{\pi}{2} \frac{(x-x_0)^2 + (y-y_0)^2}{R(z)}. \quad (135)$$

For most physical systems, z_0 is a secondary source point, and thus the radius of curvature of the wavefront can be more generally defined as

$$R(z) = R_0 + z - z_0. \quad (136)$$

A real radius of curvature implies that the wavefront is not paraxially-conforming, since the wavefront by this definition can then extend beyond the transverse bounds for a paraxial system. A complex radius of curvature can account for a paraxial system where propagation can continue indefinitely in the z-axis, but the transverse

profile will be bounded. Using a simple substitution, the complex radius of curvature is

$$\tilde{q}(z) = \tilde{q}_0 + z - z_0. \quad (137)$$

Assuming the initial transverse coordinates are on-axis ($x_0 = 0, y_0 = 0$), the amplitude for a complex spherical paraxial wave is

$$\tilde{u}(x, y, z) = \frac{1}{\tilde{q}(z)} e^{-ik \left[\frac{x^2 + y^2}{2\tilde{q}(z)} \right]}. \quad (138)$$

By extracting the real and imaginary components of the complex radius of curvature, the physical beam properties can be obtained. The separation,

$$\frac{1}{\tilde{q}(z)} \equiv \frac{1}{q_r(z)} - i \frac{1}{q_i(z)}, \quad (139)$$

is then substituted into the amplitude,

$$\tilde{u}(x, y, z) = \frac{1}{\tilde{q}(z)} e^{-ik \left[\frac{x^2 + y^2}{2q_r(z)} - i \frac{x^2 + y^2}{2q_i(z)} \right]}. \quad (140)$$

The phase front will now propagate in the z-direction but the transverse profile will be limited. The next step is to define $q_r(z)$ and $q_i(z)$. It is clear that $q_r(z)$ is the real radius of curvature

$$\frac{1}{q_r(z)} \equiv \frac{1}{R(z)} \quad (141)$$

This makes $q_i(z)$ the physical limitation of the transverse profile as a function of propagation. The starting expression used to solve for $q_i(z)$ is

$$\frac{k(x^2 + y^2)}{2q_i(z)} = \frac{(x^2 + y^2)}{w^2(z)}, \quad (142)$$

where $w^2(z)$ is the physical size, or waist, of the beam accounted for units. After

algebraic manipulation, the expression for $q_i(z)$ is

$$\frac{1}{q_i(z)} = \frac{\lambda}{\pi w^2(z)}. \quad (143)$$

The final expression for the complex radius of curvature $\tilde{q}(z)$ is

$$\frac{1}{\tilde{q}(z)} \equiv \frac{1}{R(z)} - i \frac{\lambda}{\pi w^2(z)}. \quad (144)$$

This expression of $\tilde{q}(z)$ can be used to extract physical parameters, but not without some difficulty [60]. One must know two of the three parameters to find the third, and in a physical system, the complex and the real radius of curvature are typically unknown. It is also impossible to find the beam waist within an optical element train without invasive measurements that may disturb the system. Therefore, it is necessary to go back to the expression in equation 137. The first step is to solve for \tilde{q}_0 . Assuming a free-space propagation, with a $z_0 = 0$ and no propagation ($z = 0$), then

$$\tilde{q}(z) = \tilde{q}_0 = \left[\frac{1}{R(0)} - i \frac{\lambda}{\pi w^2(0)} \right]^{-1}. \quad (145)$$

This condenses into

$$\tilde{q}_0 = i \frac{\pi w_o^2}{\lambda}, \quad (146)$$

where w_o is the beam waist. The main implications of this are fairly straightforward; since the real radius of curvature is infinite at the primary or secondary source location, the beam waist is then the size of the collimated beam. It also acts as the effective focal point of a Gaussian beam, since the propagating beam must diverge outward from this location.

Referencing a constraint used in equation 130 to construct the transverse profile, it can be reasoned that

$$\frac{\pi w_0^2}{\lambda} = iz_R \quad (147)$$

where z_R , defined as the Rayleigh range, is some physical distance within the transverse profile constraint where the size of the beam can be described by the beam waist. Putting this new parameter into the complex radius of curvature,

$$\tilde{q}(z) = z + iz_R, \quad (148)$$

the complex radius of curvature can be described in well-understood physical parameters.

As stated before, it is difficult, if not impossible, to find the beam waist within an optical element train. It is also necessary to be able to predict the waist as it changes throughout an optical arrangement in order to create simulations for data comparison or experimental design. To find an expression for $w(z)$, an algebraic manipulation of the complex radius of curvature can be carried out. The expression for $\tilde{q}(z)$ is inverted, producing

$$\frac{1}{\tilde{q}(z)} = \frac{z}{z^2 + z_R^2} - i \frac{z_R}{z^2 + z_R^2} = \frac{1}{R(z)} - i \frac{\lambda}{\pi w^2(z)}. \quad (149)$$

The imaginary part is then isolated, producing

$$-i \frac{z_R}{z^2 + z_R^2} = -i \frac{\lambda}{\pi w^2(z)}. \quad (150)$$

After doing so, the expression for the beam waist at some propagation point z is

$$w(z) = w_0 \sqrt{1 + \left(\frac{z}{z_R}\right)^2}. \quad (151)$$

This expression assumes only free-space propagation. With the addition of optical elements, it is not possible to find the beam waist without a consideration of optical power and changing refractive indices. A common method to translate through elements is to apply the geometric ray optics method using the central ray to trace by using a 2x2 matrix propagation method. Another approach is to propagate a physical wave.

The matrix method can give ray propagation and information on how the beam changes in aligned, on-axis paraxial systems; however, this method is unable to produce results in systems with off-axis and tilted elements. A full wave propagation approach gives a multitude of beam information at any propagation location, for any system, but it is difficult to work with and obtain exact solutions for a given experimental arrangement. For the system of interest in the presented work, computations of off-axis and tilted elements are necessary but do not justify the burden of finding an exact solution to a full wave propagation.

A way to take advantage of the ease of use with the matrix method and still obtain beam information produced from a wave propagation process is by combining both. Following the mathematical formulation presented in [60, 61], a 3x3 matrix propagation can be constructed starting from the full wave expression and keeping

terms necessary for tilted and off-axis systems. The general form is given by

$$\begin{pmatrix} v_x(z) \\ [Q_x(z)/k_0(z)]v_x(z) \\ S_x(z)v_x(z) \end{pmatrix} = \begin{bmatrix} A_x(z) & B_x(z) & 0 \\ C_x(z) & D_x(z) & 0 \\ G_x(z) & H_x(z) & 1 \end{bmatrix} \begin{pmatrix} v_x(0) \\ [Q_x(0)/k_0(0)]v_x(0) \\ S_x(0)v_x(0) \end{pmatrix}, \quad (152)$$

where $v_x(z)$ is a test function used to establish the matrix formalism. The beam parameter function $Q_x(z)$ is proportional to the complex radius of curvature $\tilde{q}(z)$ and is defined as

$$Q_x(z) = \frac{2\pi}{\lambda R(z)} - i \frac{2}{w_x^2(z)} \quad (153)$$

and $k_0(z)$ is the wave propagation function. In homogeneous free-space, the wave propagation function is constant. To connect the beam parameter function Q to the complex radius of curvature \tilde{q} , equation 153 is divided through by k_0 , giving

$$\frac{Q_x(z)}{k_0(z)} = \frac{1}{R(z)} - i \frac{\lambda}{\pi w_x^2(z)} = \frac{1}{\tilde{q}}. \quad (154)$$

To find the beam parameter function Q in terms of matrix elements describing the system of propagation, the solutions can be divided to produce

$$\frac{Q_x(z)}{k_0(z)} = \frac{C_x(z) + D_x(z)Q_x(0)/k_0(0)}{A_x(z) + B_x(z)Q_x(0)/k_0(0)}, \quad (155)$$

which is referred to as the Kogelnik transformation. Substitution of \tilde{q} into equation 155 and solving for \tilde{q} gives

$$\tilde{q}(z) = \frac{A_x(z)\tilde{q}_0 + B_x(z)}{C_x(z)\tilde{q}_0 + D_x(z)}. \quad (156)$$

The parameter S is a beam parameter defined as

$$S_x = -Q_x d_{xa} + k_0 d'_{xa}, \quad (157)$$

where d_{xa} is the translational beam displacement from the optic axis and the d'_{xa} is the slope of the wavefront. There is also an expression for S in terms of matrix elements similar to equation 155 given as

$$S_x(z) = \frac{S_x(0)}{A_x(z) + B_x(z)Q_x(0)/k_0(0)} + \frac{G_x(z) + H_x(z)Q_x(0)/k_0(0)}{A_x(z) + B_x(z)Q_x(0)/k_0(0)}. \quad (158)$$

With S and Q , beam propagation through translated elements can be found.

The matrix elements now need definition. Starting with the beam parameter function S , it can be reasoned that a paraxial beam in a system of aligned on-axis elements will not experience a beam amplitude displacement nor will it possess a non-zero beam slope. Thus, in these systems, $G, H = 0$, and the 2x2 matrix method developed for ray optics can be used for Gaussian beam propagation. Outside of this special case, it is necessary to start with a generalized solution to the matrix coefficients [60].

Solutions to A and B are

$$A_x(z) = \cos(\gamma_x z), \quad (159)$$

$$B_x(z) = \frac{1}{\gamma_x} \sin(\gamma_x z), \quad (160)$$

where

$$\gamma_x \equiv \left(\frac{k_{2x}}{k_0} \right). \quad (161)$$

C and D are defined as

$$C_x(z) = -\gamma_x \sin(\gamma_x z), \quad (162)$$

$$D_x(z) = \cos(\gamma_x z). \quad (163)$$

G and H are defined as

$$G_x(z) = -\frac{1}{2} \int_0^z k_{1x}(z') \cos(\gamma_x z') dz', \quad (164)$$

$$H_x(z) = -\frac{1}{2} \frac{1}{\gamma_x} \int_0^z k_{1x}(z') \sin(\gamma_x z') dz'. \quad (165)$$

Now that the matrix elements have been defined for a generalized system, it is clear that to develop a single matrix for an entire optical element train, the propagation vector k will become burdensome to define. A more-manageable method is to define the system piece-wise using arbitrary choices of k to represent different propagation distances and interfaces. The first matrix of interest to this work is for free-space propagation in a homogeneous medium,

$$\overleftrightarrow{M}_p = \begin{bmatrix} 1 & d & 0 \\ 0 & 1 & 0 \\ 0 & 0 & 1 \end{bmatrix}, \quad (166)$$

where d is the distance traveled in the medium. The next matrix of interest is for an aligned boundary,

$$\overleftrightarrow{M}_{ab} = \begin{bmatrix} 1 & 0 & 0 \\ 0 & k_{01}/k_{02} & 0 \\ 0 & 0 & 1 \end{bmatrix}, \quad (167)$$

where k_{01} and k_{02} are the k_0 constants for the incident and substrate media, respec-

tively. Additionally, the matrix for a tilted boundary,

$$\overleftrightarrow{M}_{tb} = \begin{bmatrix} 1 & 0 & 0 \\ 0 & k_{01}/k_{02} & 0 \\ (k_{01} - k_{02}) \tan \theta_t & 0 & 1 \end{bmatrix}, \quad (168)$$

is useful for plano surfaces of PCX and PCV lenses. The θ_t refers to the tilt angle in the tangential plane. The sagittal plane matrix, in cases of a tilted boundary is identical to the matrix for an aligned boundary. Similarly, there are distinct matrices for the tangential and sagittal planes for a spherical boundary. For the tangential plane, the matrix is

$$\overleftrightarrow{M}_{tsb} = \begin{bmatrix} 1 & 0 & 0 \\ (1 - k_{01}/k_{02}) \cos \theta_t / R_t & k_{01}/k_{02} & 0 \\ (k_{01} - k_{02})(\tan \theta_t + t_0 \cos \theta_t / R_t) & 0 & 1 \end{bmatrix}, \quad (169)$$

where R_t is the radius of curvature of the boundary in the tangential plane and t_0 is the translational displacement of the boundary surface away from the optic axis in the tangential plane. The radius of curvature follows the normal sign conventions, where the center of curvature placed before the surface represents a PCV radius and the center of curvature after the surface represents a PCX radius. The term θ_t is still the axial displacement from normal in the tangential plane. The sagittal plane is

$$\overleftrightarrow{M}_{ssb} = \begin{bmatrix} 1 & 0 & 0 \\ (1 - k_{01}/k_{02}) \cos \theta_t / R_s & k_{01}/k_{02} & 0 \\ 0 & 0 & 1 \end{bmatrix}, \quad (170)$$

where R_s is the radius of curvature in the sagittal plane. This means the matrix

method can accommodate different radii of curvature in different planes. For the system of interest in this work, the radii R_t and R_s are equivalent. It is also important to note the coordinate axes in this work consist of a tangential plane in the yz -plane and a sagittal plane in the xz -plane.

To develop the summary matrix, typical matrix method multiplication rules apply. This method uses an assembly by starting with the last propagation matrix in the system and moving through to the first matrix. The summary matrix is then expressed as

$$\overleftrightarrow{M}_s = \overleftrightarrow{M}_l \overleftrightarrow{M}_{l-1} \dots \overleftrightarrow{M}_2 \overleftrightarrow{M}_1, l = 1, 2, \dots, m, \quad (171)$$

where m is the total number of matrices needed to define the system.

For a thick lens with the planar side first, the matrix to describe the lens in the xz -plane is

$$\overleftrightarrow{M}_{tl} = \overleftrightarrow{M}_{ssb} \overleftrightarrow{M}_p \overleftrightarrow{M}_{ab}, \quad (172)$$

and for the yz -plane is

$$\overleftrightarrow{M}_{tl} = \overleftrightarrow{M}_{tsb} \overleftrightarrow{M}_p \overleftrightarrow{M}_{ab}. \quad (173)$$

For a thick lens with the curved surface first, the matrix to describe the system in the xz -plane is

$$\overleftrightarrow{M}_{tl} = \overleftrightarrow{M}_{ab} \overleftrightarrow{M}_p \overleftrightarrow{M}_{ssb}, \quad (174)$$

and for the yz -plane is

$$\overleftrightarrow{M}_{tl} = \overleftrightarrow{M}_{ab} \overleftrightarrow{M}_p \overleftrightarrow{M}_{tsb}. \quad (175)$$

For the system of interest in this work, a PCX lens with the planar surface first is

succeeded by a PCV lens with the curved surface first and separated by a free-space propagation. Another free-space propagation follows the planar side of the PCV lens. The final summary matrix to describe this system is then

$$\overleftrightarrow{M}_s = \overleftrightarrow{M}_{p2} \overleftrightarrow{M}_{t2} \overleftrightarrow{M}_{p1} \overleftrightarrow{M}_{t1}, \quad (176)$$

where $\overleftrightarrow{M}_{p2}$ is the free-space propagation matrix from the planar surface of the PCV lens to the detector surface, $\overleftrightarrow{M}_{t2}$ is the thick lens matrix for a curved surface first and represents the PCV lens, $\overleftrightarrow{M}_{p1}$ is the free-space propagation matrix for the separation between the lens' surfaces, and $\overleftrightarrow{M}_{t1}$ is the thick lens matrix for a planar surface first and represents the PCX lens. Thus, for the arrangements of interest for any translation away from the optic axis, the propagation matrix can be found.

For the work presented in this investigation, it is necessary to find, by use of the propagation matrix, both Q and S . Using Q , the beam size can be determined, but with a translated optic, S along with some simple geometric relations is needed in order to obtain wavefront displacement.

1.5.3 Seidel Wavefront Aberrations

A discussion of wavefronts would be incomplete without including aberrational effects. Given a monochromatic source, chromatic aberration effects will not be considered.

To describe monochromatic aberrations in a given optical system, a Seidel polynomial fit is usually applied [62, 63]. The Seidel polynomial is defined as

$$W = \sum_{i,j,k} W_{ijk} \overline{H}^i \rho^j \cos^k \phi, \quad (177)$$

where W_{ijk} is the wavefront aberration coefficient for the given term. The coefficient is a value of optical path difference (OPD) away from an ideal image plane location. This value is most commonly given in terms of waves, or wavelengths λ of the source. Thus, for a red HeNe source of $632.8nm$, a wavefront coefficient of 2 waves, or 2λ , would be an OPD of $1.266\mu m$ away from the ideal image plane location. The remaining terms in equation 177 are for a unit cylindrical coordinate system, where \bar{H}^i is image height, ρ^j is the pupil radius, and ϕ is the polar angle of the pupil.

The Seidel wavefront aberrations are the collection of aberrations in which $i+j = 4$. These correspond to spherical aberration, coma, astigmatism, field curvature, and distortion. Table 1 summarizes the mathematical expressions for each of these terms.

Spherical aberration (W040) is the defocus of the spot size due to the curvature of a lens. Rays entering the edge of a PCX lens will focus closer to the optical element than those entering near the optic axis. In paraxial approximations, spherical aberration is usually of negligible impact.

Coma (W131) is the distortion at the observation plane coming from off-axis rays with respect to the optical element. This aberration is normally present in tilted systems, and is minimized by using optical elements and detectors normal to the beam path.

Astigmatism (W222) is a defocusing effect where orthogonal transverse axes have different focal points along the optic axis. The effect is commonly found in optics where each axis on the surface of the optical element has a different radius of curvature. For a perfect spherical surface, astigmatism is theoretically non-existent.

Field curvature (W220) is the effect of the focal plane to curve as a ray is propagated

Table 1: Seidel wavefront terms

Name	Coefficient	Term
Spherical	W040	ρ^4
Coma	W131	$\bar{H}\rho^3 \cos \phi$
Astigmatism	W222	$\bar{H}^2 \rho^2 \cos^2 \phi$
Field Curvature	W220	$\bar{H}^2 \rho^2$
Distortion	W311	$\bar{H}^3 \rho \cos \phi$

through a lens at an off-axis trajectory. This can be corrected for in many systems by rectifying the exiting ray from the optical element of interest with additional optical elements.

Finally, distortion (W311) is another focal plane effect where the focal point is transversely displaced from the theoretical focal point, but is still in the same focal plane as opposed to field curvature aberration. Like coma, tilted systems will experience increased distortion.

In following discussion of Seidel wavefront aberrations, the wavefront coefficient term (WIJK) will be used for the sake of brevity.

1.6 Proposed Methodology for Performance Measurement of Random Anti-Reflection Surface Structure on Curved Surfaces

In this work, a set of testing methods are proposed to characterize optical performance of rARSS on spherical lenses of various EFLs. The rARSS on the lenses were prepared by etching in an RIE process using an optimized transmission recipe for FS substrates for use with 633nm sources. In addition to this optimized lens set, a set of lenses were etched in a non-optimized process to provide comparison samples.

The testing procedure proposed consists of measurements of transmission and beam

profile through each lens in singlet and doublet configurations. In order to carry out the testing, a $633nm$ source was focused to a $96\mu m$ spot size at the test site by a $+100mm$ focusing lens. The test mount, which holds the singlet or doublet configurations, was translated vertically away from the optic axis. At each position, the test mount was rotated as transmission measurements were taken in order to provide a reliable sample size at each radial zone.

For the singlet configurations, the test mount was tilted at a number of angles in order to investigate the effect of AOI on the transmission of rARSS on spherically-curved surfaces. For the doublet configuration, in addition to the transmission performance tests at normal incidence, beam profiles at the various radial distances were taken in order to investigate the effect of rARSS on beam shaping. Each testing procedure developed was paired with an appropriate validation test of either FS slabs and/or FS uncoated lenses. AR-coated BK7 lenses were also used to compare with industry-standard solutions to AR applications.

Computations for comparison metrics were also created for transmission and beam profiles for the various test samples and parameters. These proposed computations served not to replicate each sample, but to instead provide a generic and universal comparison standard able to be utilized to grade other AR lenses against rARSS lenses. It can also be used for grading successive generations of rARSS lenses in a optimization feedback process. For the curved surfaces of each rARSS lens and for the front and back of each AR-coated BK7 lens, an ideal single-layer AR (SLAR) coating model at normal incidence for $633nm$ sources was used. Additionally, beam profile propagation metrics were created using the same ideal SLAR coating.

Both the proposed testing and computed metrics were used in order to obtain optical performance data for rARSS on lenses. For the singlet configurations, the transmission data were analyzed primarily by extracting a transmission enhancement value for the rARSS lenses. This value, in which the increase in transmitted light for each rARSS surface as compared to an uncoated surface, was investigated for transmission dependencies. The primary dependency of the transmission through the optimized lenses was discovered to be the AOI as seen by the surface. The transmission of the non-optimized lenses was found to be primarily dependent on height of the lens surface. Thus, for optimized etch recipes, AOI applications need to be considered, and thickness of the substrate is not necessary to account for in order to enhance transmission. As the etch recipe becomes less optimized, the substrate thickness parameter will dominate the transmission enhancement, and AOI dependence will diminish.

Another result extracted from the singlet configuration data indicated the PCV rARSS lenses experienced a lower transmission enhancement than the PCX rARSS lenses for the same parameters. The cause of this transmission enhancement loss is hypothesized as a loss of etch efficiency as a result of the concavity on the PCV lens surface.

The doublet configuration transmission data was analyzed by use of a transmission efficiency figure. The transmission efficiency is a comparison metric developed in order to compare individual element performance in multi-element systems unable to be separated in post-processing from the performance of other elements in the system. The rARSS pair underperformed in comparison to the AR-coated pair. In order to

further understand whether the loss of performance was due to a cascaded effect or due to individual losses at each lens, constructed doublets made of transmission data from the individual singlets were compared to the data from the bulk doublets. The data from the constructed and bulk doublets matched, with comparable transmission losses. This indicates loss is localized at the PCV rARSS lens elements, and is not a result of cascaded effects in the rARSS surfaces.

To further understand the relationship between the transmission performance and the surface structure, scanning electron microscopy (SEM) was performed on both optimized and non-optimized samples. There was a clear difference in surface structure characteristics between each type, with an indication of isotropic structure formation on all samples. Further investigation is recommended to fully understand the nature of structure formation on curved surfaces.

Finally, beam profile investigations were graded by an analysis of beam spot size at the measurement location. These measurements showed, by comparison with the computed metric as well as other combinations, the shorter EFL lenses have a greater effect on beam spot size than longer EFL lenses. This result is unsurprising when considering the evidence already found indicating that thicker lens substrates and higher AOI, factors most prominent in the lower EFL lenses, are dominant factors in transmission performance.

CHAPTER 2: TRANSMISSION PERFORMANCE OF SINGLET LENSES WITH RANDOM ANTI-REFLECTION SURFACE STRUCTURE

2.1 Introduction

In this chapter, a study of the transmission performance of rARSS on spherical lenses is presented. The transmission performance was computed in order to construct a comparison metric for the evaluation of future optical power elements. In addition to rARSS on spherical lenses, commercially-obtained AR-coated BK7 spherical lenses as well as uncoated FS spherical lenses were tested in the same procedure. Another set of rARSS lenses, using a non-optimized etch recipe for the test wavelength, was also tested. Various analyses focusing on surface curvature, thickness of the lens, and AOI from the tilt of the lens and the surface curvature were performed in order to determine the limiting factors of performance for the rARSS on these types of elements.

2.2 Experimental Implementation

A HeNe laser beam (Thorlabs HNL050L) [64] was focused by a +100mm EFL PCX lens (Thorlabs LA1509-A) [65] to form a 96 μm spot at the test element surface as shown in Fig. 8. Transmitted power was then collected by a photodiode detector (Thorlabs S120C) [66].

The testing procedure consisted of measuring the transmitted signal, through the lens under test, as a function of the vertical translation position (y) by use of a

1D translation stage (Thorlabs PT1) [67] of the element at various tilts by use of a rotation stage (Thorlabs RP01) [68] with respect to the vertical. The lens under test was mounted with the convex or concave surface facing the light source and tilted at global angles θ of 0° , 15° , and 30° between the vertical and back planar surface.

Prior to data acquisition, power test data was taken. The set includes data from over 1 hour 45 minutes beginning when the laser is first powered on. This is shown in Fig. 9. This data was used to determine an appropriate wait time to allow for the laser to stabilize before data acquisition. Oscillations of the measured power were attributed to both laser and detector device uncertainties. The uncertainty of each of these values, as well as the translation and rotation mount uncertainties, are shown in Table 2. The photodiode's quotation of uncertainty is NIST traceable. The maximum time tested, 1 hour 45 minutes, was implemented as the wait time before data acquisition due to the observed oscillation of power prior to this timing mark.

Power test data was also used to compare with expected measured results based on instrument uncertainty. The expected range of uncertainty, based on compounded laser and detector limitations, is $\pm 0.342mW$, or $\pm 6.5\%$. The range of 5000-6300 seconds was used to calculate realistic uncertainty expected to be found in future data acquisition. The range of these measurements is $\pm 0.0156mW$. This indicates stable data acquisition can be taken over this time period.

In order to combat further complications arising from laser power oscillation, data sets were taken in small batches. These batches were organized by lens EFL, material, surface treatment, and global angle, with the full range of translation positions. Before each batch, a normalization data set with no lens in the test mount was taken.

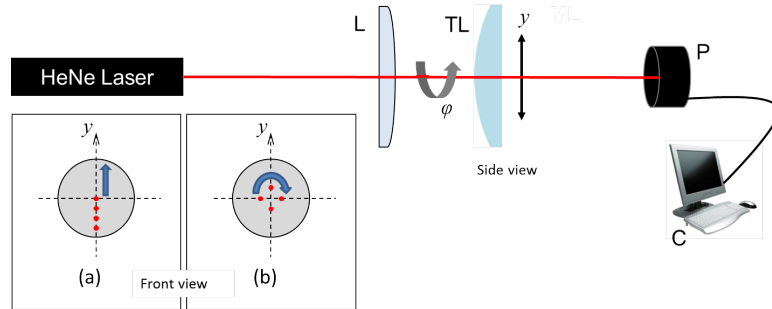


Figure 8: Experimental layout used to measure localized transmission of rARSS lenses: L, $+100\text{mm}$ EFL PCX lens that is focusing the incident beam to a $96\mu\text{m}$ spot size at the front surface of the test lens; TL, lens under test; P, photodiode detector; C, data-collecting PC. TL rests on a kinematic stage, allowing (a) translation along the vertical coordinate y and (b) rotation around the azimuth angle ϕ .

Table 2: Rated uncertainty and tolerance for utilized equipment

Device	Uncertainty Type	Value
Source Laser	Noise	0.2%
	Drift	$\pm 2.5\%$
Photodiode Detector	Resolution	1nW
	Measurement Uncertainty	$\pm 3\%$
	Linearity	0.5%
Translation Mount	Resolution	$\pm 0.0005''$ (0.0127mm)
Rotation Mount	Resolution	$\pm 0.5^\circ$

The data in each batch was then scaled by the corresponding normalization data set.

Figure 11 depicts the spatial orientation of the tested lenses. By stitching together positive (+, Fig. 11(a)) and negative ($-$, Fig. 11(b)) global angular tilt test results, the method provided a test over the full aperture of the lenses without requiring physical travel over the entire arc of the surface. The test positions at each global tilt value were selected starting from the lens center and moving through 7.5mm for the $+50\text{mm}$ EFL and $+75\text{mm}$ EFL lens samples and through 6.0mm for the $+100\text{mm}$ lens samples in increments of 1.5mm . The radial extent was adjusted for PCV lenses such that -75mm and -100mm EFL lens samples were measured out to 7.5mm

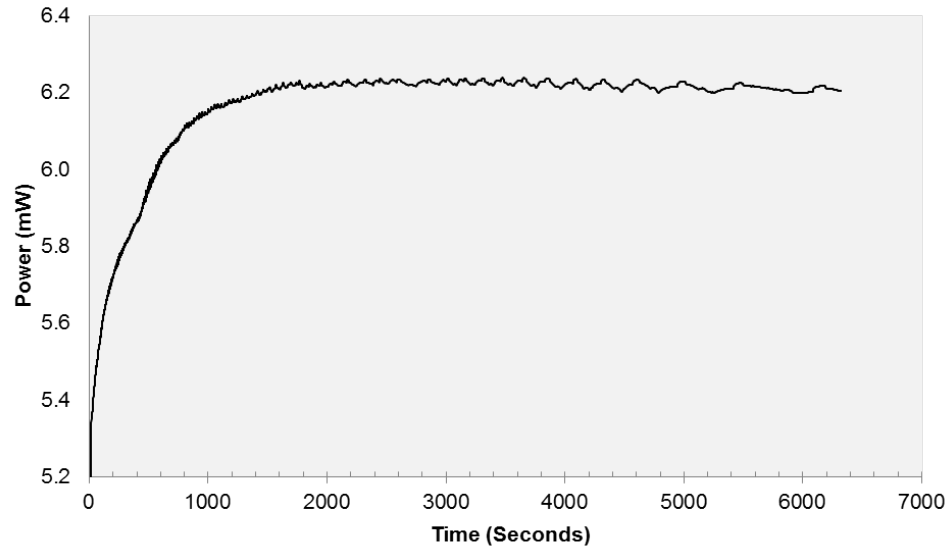


Figure 9: Laser power test data over a time period of approximately 6300 seconds, or roughly 1 hour 45 minutes, beginning at laser start-up.

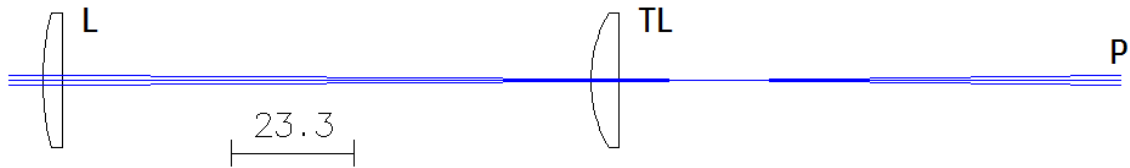


Figure 10: OSLO sample ray trace diagram of the focusing lens L used to create the $96\mu\text{m}$ spot size on the test lens TL. Sample shown is $+50\text{mm}$ EFL BK7 lens. Ray pencil from L to detector plane P is shown in blue. Diagram is to scale and is in mm .

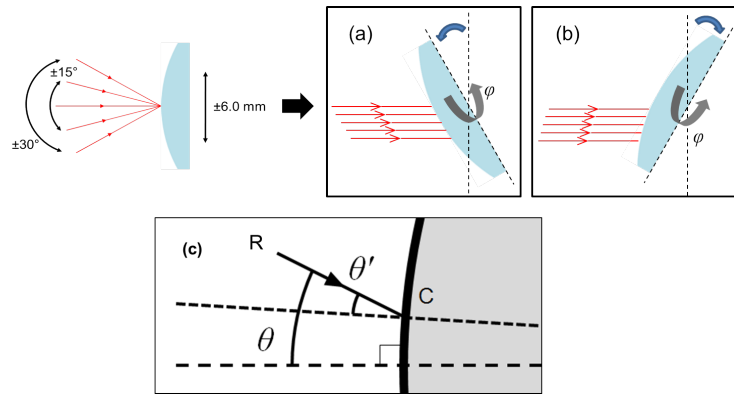


Figure 11: Global angle θ and corresponding local angle θ' . A global 60° field-of-view can be tested by tilting the element with respect to the back planar surface across a test full aperture of $12\text{--}15\text{mm}$. (a) PCX lens tilted at global 0° , 15° , and 30° , with respect to the planar back surface. (b) PCX lens tilted at global -0° , -15° , and -30° , with respect to the planar back surface. The translated rays are shown in both cases. The localized rays are accessed by translating the lens holder along the vertical direction. The local angle is between the incoming ray and the curved surface normal. (c) Ray R incident on a curved surface C will have a different local angle θ' with respect to the surface normal when compared to the optic axis global angle θ . This angle will continue to change as the ray is translated across the open aperture. PCV lenses were measured in with the same arrangement.

and the -50mm EFL lens samples were measured out to 6.0mm from the optic axis. Each radial increment was taken with respect to the back planar surface to ensure the same radial zone at each global angle tilt. These positions created a zonal map of transmission measurements over the lens surface. Given the increment of 1.5mm and a resolution of $\pm 0.0254\text{mm}$, the variance of radial positions is expected to be negligible.

The positive or negative global angle tilt of the lens under test resulted in different AOI, referred to as the local angle θ' , over the lens surface. For example, Fig. 12 shows the local angle as a function of global angle and radial position for the $+50\text{mm}$ FS PCX sample lens. As such, the transmission results were not expected to be symmetric about the chief ray orientation. The total FOV is then expected to be

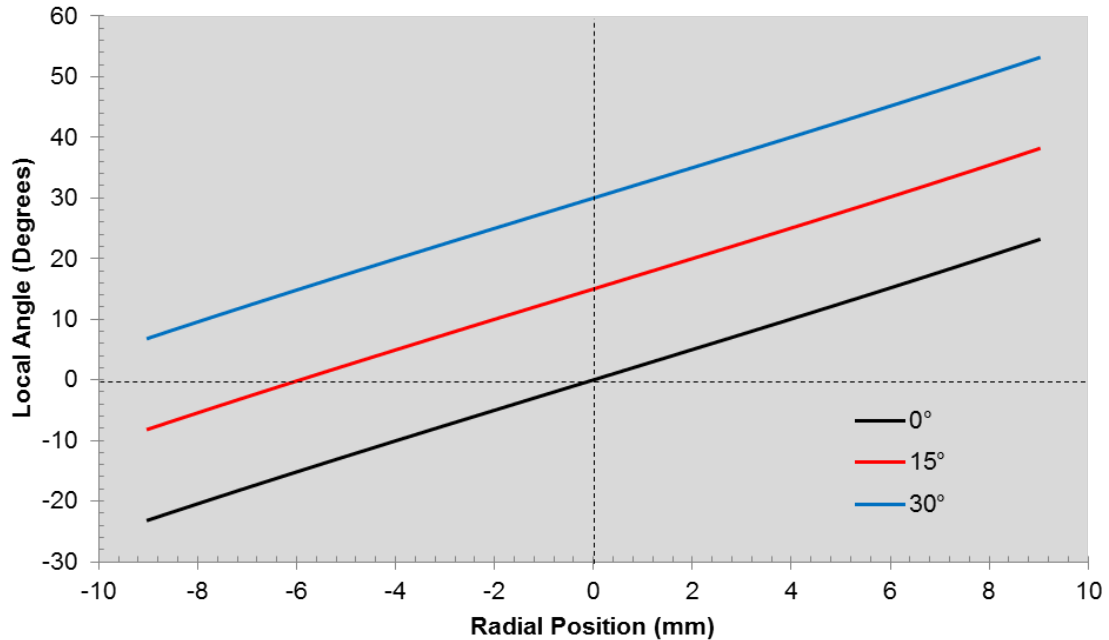


Figure 12: Global and corresponding local angle variation over the convex surface of $+50\text{mm}$ EFL FS lens. The black line is the 0° global angle, the red line is the 15° global angle, and the blue line is the 30° global. For a given global angle over a clear aperture of 18mm , the local angle has a range of over 45° . The dashed lines represent the axes of radial position and local angle for ease of comparison.

$> 70^\circ$. Measurement uncertainty compounded from both the rotation mount and the translation stage will produce a negligible range of uncertainty (1.01°) in comparison to the rated FOV.

At each new radial position, the element was rotated around the optic axis, measuring eight equally-spaced azimuthal positions. In order to verify this sampling selection, four azimuthal intervals (45° , 30° , 20° , and 10°), shown in Fig. 13, were used to gather transmission performance measurements for a 75mm EFL AR-coated BK7 lens sample. The results of this testing are shown in Fig. 14. Observations proved 45° would provide sufficiently-sampled data at a lower level of required labor. At each azimuthal position, 100 power readings at 1-second time intervals were

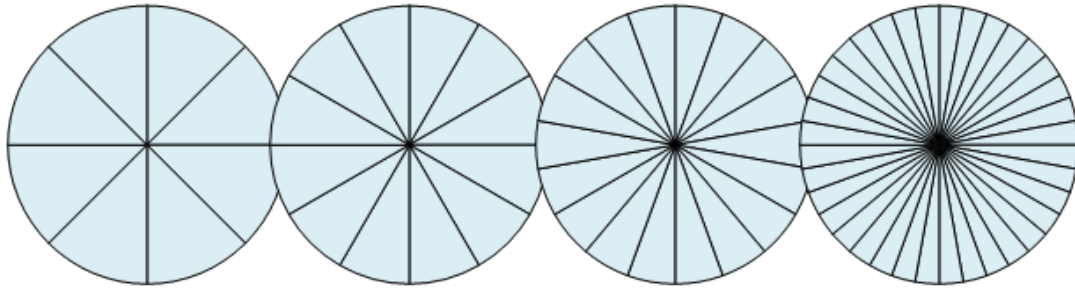


Figure 13: Azimuthal intervals used to verify azimuthal sampling value. From left to right: 45° , 30° , 20° , 10° .

Table 3: Specifications of lens samples. All values are given in mm. BK7 samples are AR-coated, FS samples are uncoated. R_1 is the curved-side radius of curvature, T_c is the center thickness, and T_e is the edge thickness.

EFL	Lens	Manufacturer	R_1	T_c	T_e
+50	BK7	Thorlabs	$25.8 \pm 1\%$	5.3 ± 0.1	2.0 ± 0.1
	FS	Edmund Optics	$22.92 \pm 1\%$	5.84 ± 0.1	2.13 ± 0.1
-50	BK7	Thorlabs	$-25.7 \pm 1\%$	3.5 ± 0.1	6.9 ± 0.1
	FS	Edmund Optics	$-22.92 \pm 2\%$	2.0 ± 0.2	5.52 ± 0.2
+75	BK7	Thorlabs	$38.6 \pm 1\%$	4.1 ± 0.1	2.0 ± 0.1
	FS	Edmund Optics	$34.39 \pm 1\%$	4.43 ± 0.1	2.0 ± 0.1
-75	BK7	Thorlabs	$-38.6 \pm 1\%$	3.5 ± 0.1	5.6 ± 0.1
	FS	Edmund Optics	$-34.38 \pm 2\%$	2.5 ± 0.2	4.74 ± 0.2
+100	BK7	Edmund Optics	$51.68 \pm 1\%$	4.3 ± 0.1	2.77 ± 0.1
	FS	Edmund Optics	$45.85 \pm 1\%$	3.79 ± 0.1	2.05 ± 0.1
-100	BK7	Edmund Optics	$-51.68 \pm 1\%$	3.50 ± 0.1	4.85 ± 0.1
	FS	Edmund Optics	$-45.84 \pm 2\%$	2.50 ± 0.2	4.15 ± 0.2

taken for a total of 800 power readings over the radial zone. The normalization data consisted of 100 power readings at 1-second intervals.

Control measurements were made with unprocessed FS and AR-coated BK7 [69–71] PCX and PCV lenses. Two planar FS windows before and after etching one side of the window were also tested. These can be seen in Fig. 15 and 18 in section 2.4.

Table 3 shows specifications from each lens used.

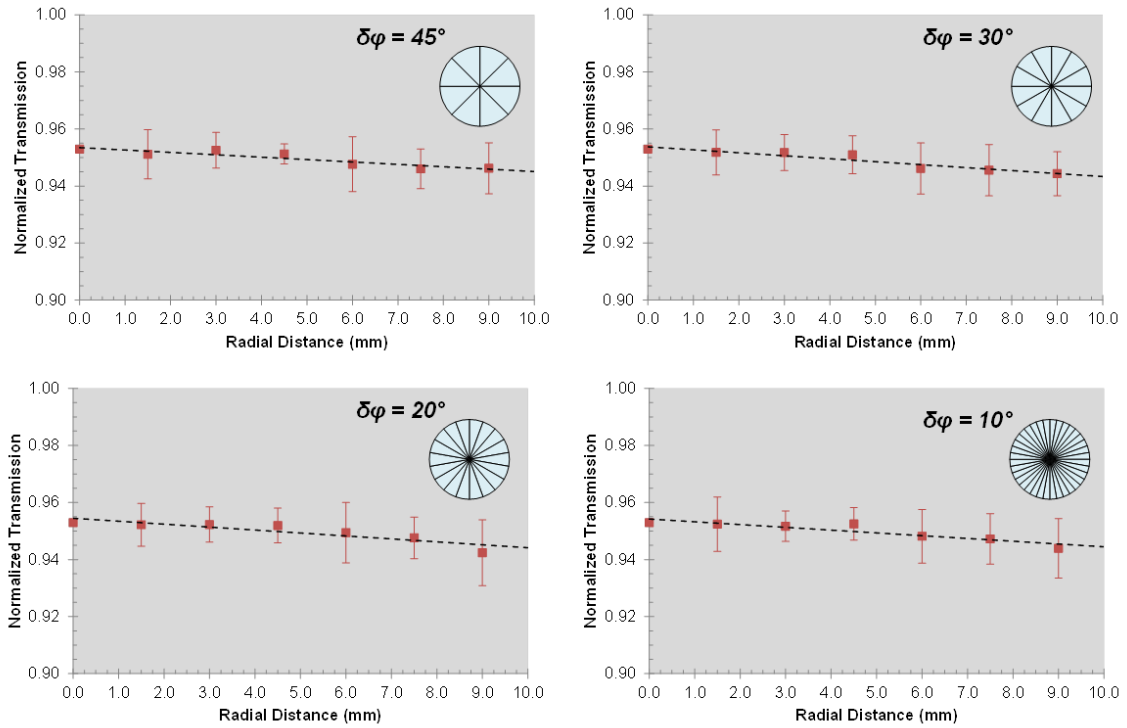


Figure 14: Comparison of transmission performance based on azimuthal zone interval. (a) 45° interval, (b) 30° interval, (c) 20° interval, and (d) 10° interval. The performance measurement and error is consistent between 45° and 10° azimuthal intervals.

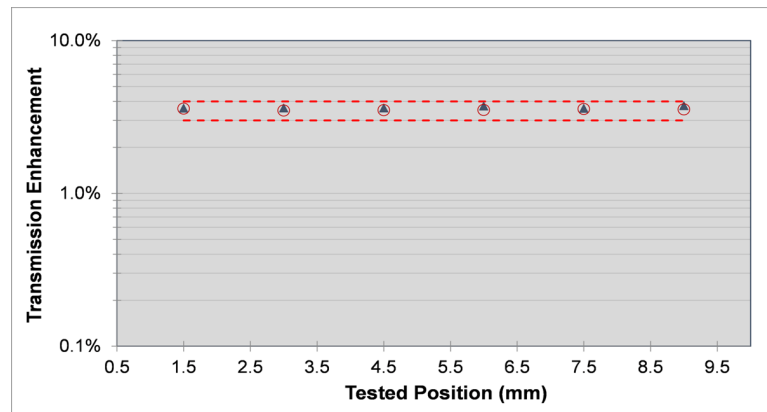


Figure 15: Two sets (\blacktriangle, \circ) of normalized transmission enhancement measurements $\tau_{123}(r)$ at normal incidence through a FS flat substrate with a thickness of 2 mm and diameter of 25.4 mm and a single rARSS surface using the test layout shown in Fig. 8. Each point shown is an average of 100 measurements on a single location using 45° linearly-polarized light. The standard deviation is the thickness of the circles shown. The +3% and +4% framing values are shown for comparison as dashed lines. The overall average transmission enhancement of the slabs is +3.6%, corresponding to a single-surface AR.

2.3 Computation of Transmission of Lens Elements

To calculate ideal-case transmission values for comparison with measured results, a model was constructed in Matlab to compute the transmission over the profile of user-specified lens focal lengths, AOI, and radial intervals.

User-defined values are the indices of the surrounding and substrate media, the range and increment of focal lengths, radial positions from center, and AOI. These values are then used to iterate through a series of nested loops. A lens from the specified range is chosen first. Next, a radial position from the range is chosen. Finally, the AOI from the range is chosen. With these variables, the transmission is determined. The loop proceeds to the next AOI until all have been determined. This process is repeated for all radial positions, and then for each specified focal length. This data is then saved on disk.

The transmission subroutine for the curved surface portion follows the determination of sag and rotation of coordinate plane to find the transmission. It then rotates the coordinate system back to the reference of the optical axis, and outputs these values for the program to find the back surface and total transmission.

In reality, it is difficult to meet the conditions for an ideal SLAR, as discussed in Chapter 1. For wavelengths in the visible and UV range, deposition of a thin film at an integer value of a quarter-wave requires precision techniques and can drive resource costs up. Materials useful as substrates for lenses and other optical elements rarely, if ever, have realistic index-matched coatings when in common incident media such as vacuum, air, water, and immersion oils. A common solution is to create layered

thin film systems of available coating media in order to compute a matched layer. Thus, the ideal SLAR criteria is often not exactly met; however, it is this standard by which all AR solutions may be graded by.

To create a model of an ideal AR-coated lens, much of the source code for the untreated lens was utilized. The front and back transmission intensities were stitched together using the optically-thick slab exact solution for transmission as a result of successive internal reflections. Instead of treating the front and back as single interfaces with a straight-forward reflection and transmission given by the Fresnel formulae, the general solution for an AR dielectric thin film was used. At normal incidence, the model gives 100% transmission, as expected.

To benchmark the process performance measurements, transmission measurements of planar FS slabs at normal incidence and 45° polarization orientation were taken before and after etching with a recipe optimized for maximum transmission at $633nm$. The control measurements consisted of averaged sets of 100 measurements per location. Six locations on the slabs were chosen in order to validate the performance of the rARSS sample versus the plain slab. The results were compared to the theoretical maximum transmission enhancement (+3.65%) for FS at a wavelength of $633nm$ shown in Fig. 15 in subsection 1.4.1. This step verified that the etching recipe was producing high transmission enhancement on flat substrates at the testing wavelength and that the proposed sampling method would not introduce mechanical errors. In order to verify this result, the fractional transmission enhancement (τ_{123}) due to a single interface AR was computed. This value is defined as the deviation from the unit of the ratio between the total transmittance of the processed substrate (T_{AR23})

to the transmittance of the original slab (T_{123})

$$\tau_{123}(r, \theta') = \frac{T_{AR23}(r, \theta')}{T_{123}(r, \theta')} - 1. \quad (178)$$

With the definition of Eq. 178, a one-sided processed substrate with measurable AR performance will have transmission enhancement $\tau > 0$. However, if the processed surface is not performing well as an AR boundary or introduces scatter, the transmission enhancement will be $\tau < 0$. The definition of τ is more than a practical convenience since to a first approximation the expansion of the transmittance ratio leads to the expression

$$\begin{aligned} \tau_{123} &= \frac{T_{AR}(1 - R_{12}R_{23})}{T_{12}(1 - R_{AR}R_{23})} - 1 \\ &\cong \left(\frac{T_{AR}}{T_{12}} - 1 \right) (1 - R_{23}(R_{21} - R_{AR})) - 1 \\ &= \left(\frac{T_{AR}}{T_{12}} \right) - \left[\left(\frac{T_{AR}}{T_{12}} \right) R_{23}(R_{21} - R_{AR}) \right] \\ &= \tau_{12}(r) - g_{AR23}, \end{aligned} \quad (179)$$

where R_{AR} is the reflectance of the processed boundary, and R_{12} and R_{23} are as previously defined in Fig. 5. Nonlinear terms in reflectance (R_{23})² have been omitted due to their negligible contribution. This approximation is valid for transparent substrates where $R_{23} < 0.1$ and assumes only that R_{AR} is much less than unity, which is the case of an AR-coated surface. The final result isolates the transmission enhancement of the first (front) boundary from the second slab boundary and allows for the term g_{AR23} in equation 179 to account for other losses such as scattering. It should be noted that if $R_{AR} = R_{12}$, it implies there are no additional losses due to scattering. Additionally, if $\tau_{123} = 0$, there is no enhanced transmission compared to

an uncoated substrate. If R_{AR} approaches 0 due to excessive off-axis reflective losses, the transmission term T_{AR} determines the deviation from enhancement. In this latter case, the specular losses are increased due to the presence of the second interface. The computational advantage of Eq. 179 is that it separates the enhancement of the AR surface from the combined slab transmittance and gives a term as a specular transmission enhancement loss metric.

The theoretical values of Fresnel reflection on a single silica interface at normal incidence vary smoothly from +3.7% at 550nm to +3.6% at 700nm. These are calculated using the refractive index values provided by the manufacturer of the FS substrates [72]. The measured values were found to have a mean of +3.6% over six locations on the tested silica flat windows. Due to the curvature of the lenses tested and the global angle of the elements, some subsequent internal reflections exiting the back surface will not arrive at the detector. As a result of this beam walk, the final transmission is simply the product of the front and back transmissions. To deduce what situations may give rise to this case for this experimental setup, empirical observations were gathered for each element and global angle.

To rate the performance of the tested lenses with rARSS, the results were compared to a SLAR. Neglecting losses for a perfectly polished thin film, Eqs. 179 and 102 can be used to arrive at

$$\tau_{123}(r, \theta) \cong \tau_{12}(r, \theta) = \left(\frac{T_{1f2}(r, \theta)}{T_{12}(r, \theta)} \right) - 1. \quad (180)$$

Equation 180 allows the parametrization of measurements and calculations to quantities only dependent on the first interface of the substrates and on the AOI. Further,

the location variables r and θ are coupled for curved interfaces, resulting in unique values of θ' , the local AOI. For planar substrates, unless there are localized interface variations, the coordinate r is redundant, and $\theta = \theta'$. Thus, for curved interfaces, it is necessary to parameterize in terms of the local AOI θ' , accounting for the lens curvature. Fig. 16 shows the functional dependence of Eq. 180 to local AOI for both incident light polarizations as well as for a perfectly matched normal incidence SLAR on FS using the refractive index values dictated by Eq. 108. The AR film thickness is $131nm$ at a wavelength of $633nm$, and only values for positive transmission enhancement are plotted ($\tau_{12}(\theta') > 0$) in the semi-logarithmic scale. The vertical asymptote for the TM incident light (p-polarization state) occurs at the Brewster angle (53.66°) since the uncoated interface transmission value becomes unity. Beyond the Brewster angle, TM incident light passing through the AR coating does not have a value greater than that of the uncoated surface. Thus, the transmission enhancement can only be 0 or negative for larger AOI. For the TE incident light, the vertical asymptote occurs at 77.3° , and the TE transmission enhancement is greater than the normal incidence value for all AOI below that value. These curves are useful in rating the rARSS performance in direct comparison to a quarter-wave SLAR. For rARSS boundary surfaces, measuring $T_{1f2} = T_{rARSS}$ and using Eq. 180 will result in curves that can be compared directly with Fig. 16.

The vertical asymptote of the s polarization at 77.3° has no physical meaning comparable to the validity of the Brewster's angle. The graph displays transmission enhancement, which is a fractional deviation from unit value (1) of the transmission ratio between an AR-coated surface and the Fresnel boundary. Therefore, if the s-

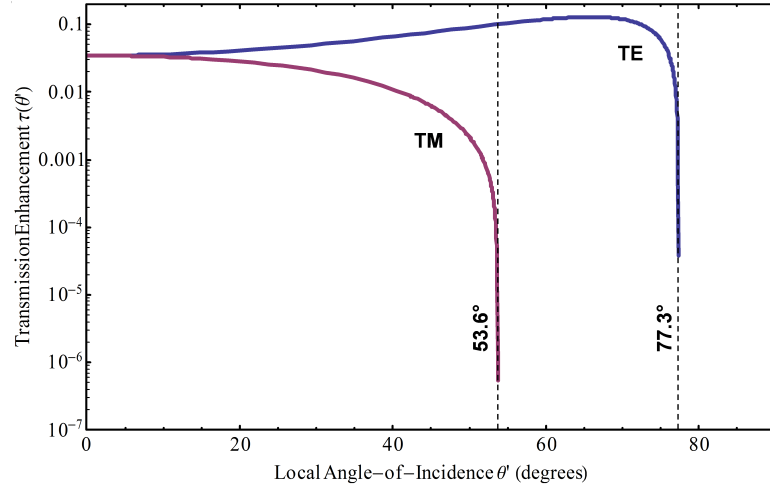


Figure 16: TE and TM transmission enhancement for a SLAR on FS as a function of AOI. The curves were obtained using Eqs. 102 and 180, and the specific thin-film values are given in the text. The vertical asymptote of the TM curve indicates the location of the Brewster's angle for the uncoated boundary.

polarized beam passing through a thin-film AR boundary produces a transmission value equal to the value of the same polarization without the film, the value of the enhancement will be equal to 0 and in a logarithmic scale will become a vertical asymptote. This does not preclude that the transmission is maximized, or otherwise affected because of the value of the angle. Simulating different multi-layered thin-film AR coatings satisfies this condition at different angle values. The same concept holds for the p polarization except that in this case $T = 1$ at Brewsters angle for the Fresnel surface. Thus, if the AR transmission is also 1, the result is a vertical asymptote as well. In that case, the transmission is maximum due to the Brewster's angle property $\tan(\theta) = n(\text{substrate})$.

Equation 180 can be normalized to the normal (0°) AOI transmission enhancement value so that the ratio becomes a comparison to that particular design benchmark. The result is then expressed as a fraction of the 0° AOI value for fused silica, in this

case 3.65%, and the dependence of the TE and TM values can be tested numerically because the SLAR thickness and the index of refraction vary above and below the optimum values. Figure 17 shows the results from such calculations using a variable index of refraction bound by the superstrate (air) and substrate (FS) values and a variable thin-film layer thickness from null to a half-wavelength value. The contours shown indicate values of equal ratios of $\tau_{12}(r, \theta')$ to the quarter-wavelength thickness and the Eq. 108 index value as the normalization constant. Figure 17(a) shows the fractional transmission enhancement at normal incidence ($\text{AOI} = 0^\circ$), and Fig. 17(b) shows the TM fractional transmission enhancement at an incidence of 34.02° . The contours can be used as indicators or figures of merit for the SLAR parameters. If the figure of merit for a SLAR coating is 50% of the total possible transmission enhancement from a single silica boundary value, then at an AOI of 34.02° , there will be a narrow choice of film thickness (~ 0.28 waves) and refractive index (~ 1.205) values that will satisfy such a design requirement, as shown in Fig. 17.

For lower AOI, the 50% transmission enhancement ratio will be met with increasingly more choice values of film thickness and index. For larger AOI, the requirement will not be satisfied even though there will be transmission enhancement of a lesser ratio. This value is imposed as the requirement for the SLAR performance and in extension for the rARSS boundary performance. Given this choice, the full FOV of the perfect SLAR-coated optic is $\pm 34.02^\circ$, rated at 50% of maximum enhancement for silica. Note that other designers can make different choices, and this choice is based on a possible realistic rating of the AR-inclusive boundary in order to rate the rARSS optical components tested. For lenses, this is a useful comparison since lens systems

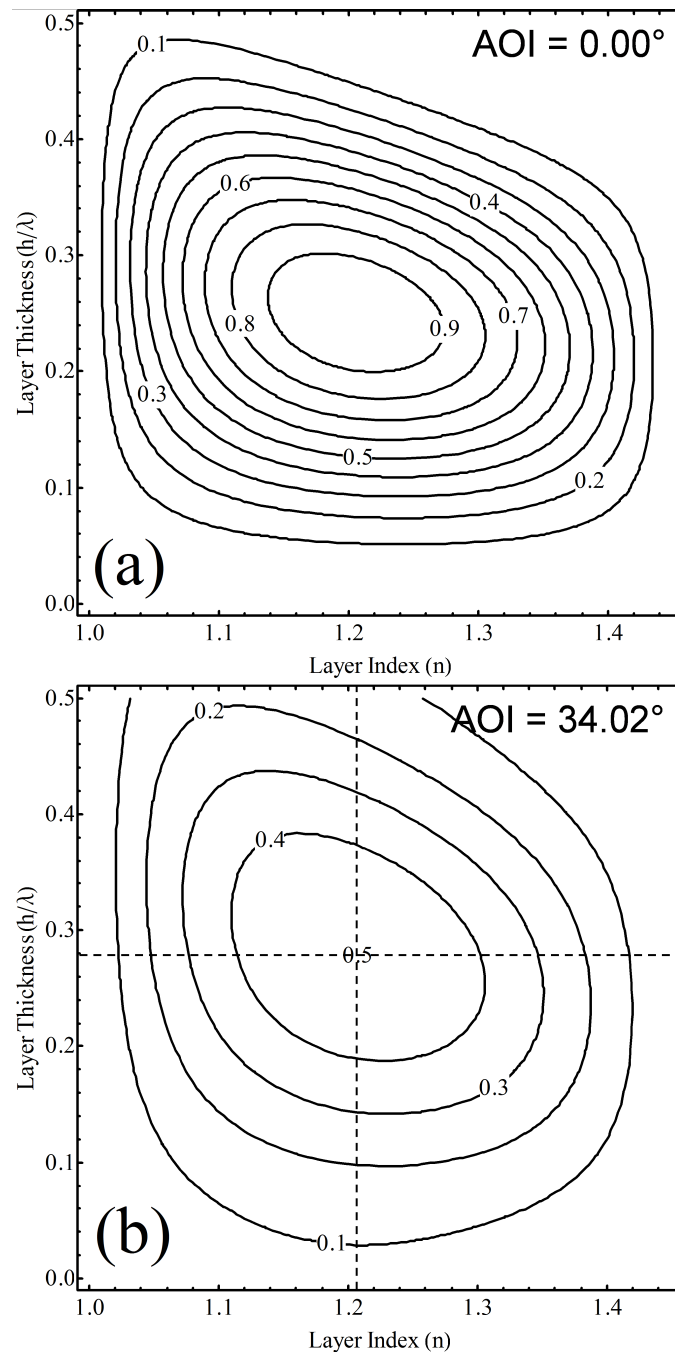


Figure 17: Contour plots showing transmission enhancement $[\tau_{12}(\theta')]$ of equal relative values to the maximum possible (3.65%) obtained for a SLAR on FS as functions of the layer thickness in wavelength units and the layer index of refraction. (a) Equal transmission enhancement contours for AOI at 0° . (b) Equal transmission enhancement contours for AOI at 34.02° . In the latter case, the maximum transmission enhancement is 50% of the Fresnel losses due to a single airsilica boundary, occurring only at the center of the contours shown here.

are rated based on their numerical aperture and thus their full FOV capabilities.

The transmission values in Eqs. 102 and 180 can be computed using the ideal thin-film model. In practice, modeling rARSS as such is not correct since the random surface is not stratified. Furthermore, the single-sided rARSS transmittance is not a directly measurable quantity since the substrates are finite in thickness and total transmittance, rather than reflectance, of the surface is measured. In practice, Eq. 16 is measured for both rARSS and non-rARSS substrates. Next, the result of Eq. 178 is calculated, which allows the backside Fresnel boundary to be divided through. A comparison of the computed values for the ideal thin film (Eq. 180) can be compared to the measured ratio of Eq. 179.

The transmission of all uncoated and perfect AR-coated single-boundary lenses was determined next using material indices and optomechanical design values obtained from the lens manufacturer. The optical transmission matrix propagation method was used for all calculations. Each lens was evaluated for the three global AOI (0° , 15° , 30°) used for the actual tests as well as for both TE and TM polarizations. Simulations were processed for an aperture diameter ($2r$) of $15.0mm$ with $+50mm$ and $+75mm$ EFL lens samples and for a diameter of $12.0mm$ with $+100mm$ EFL lens samples.

The results of these computations are shown alongside the respective results from the testing of the planar sample and of the lens samples in section 2.4. Some deviation of the results from the AR-coated BK7 and etched FS lenses is expected when compared with the computed models. The computations serve two purposes: first, in the case of the AR-coated BK7 samples, the inherent losses between the ideal thin film

and the realistic thin film are compared; second, as a reference to the etched rARSS, a comparison is made to the AR effectiveness of the textured surface. To verify and compare these results, global angle measurements were also taken for planar FS flat substrates before and after etching rARSS on a single side. In order to achieve as direct a comparison as possible, the same procedure designed for the lens elements was used for the flats.

2.4 Transmission Performance Results of Spherical Lenses with random Anti-Reflection Surface Structure

To verify and compare results, transmission measurements were taken for planar FS flat substrates before and after etching rARSS on a single side. In order to achieve as direct a comparison as possible, the same procedure designed for the lens elements was used for the flats. The averaged results and standard deviations from measurements for the planar substrates are shown in Fig. 18, and the mean percent differences of the results from the theoretical values are listed in Table 4. The mean percent difference between the measured and calculated values for the planar substrate transmission with rARSS is on the order of $< 0.5\%$, which is comparable to the same measurements performed with plain FS substrates.

The measured transmission plots for the PCX lenses are shown in Figs. 19– 21. The AR-coated BK7 lenses are shown with black square markers, the rARSS lenses are shown with red circle markers, and the uncoated lenses are shown with blue triangle markers. Markers represent expected (mean) values of each 800 data point set. Standard deviation of each set of 800 data points is indicated as an error bar. In

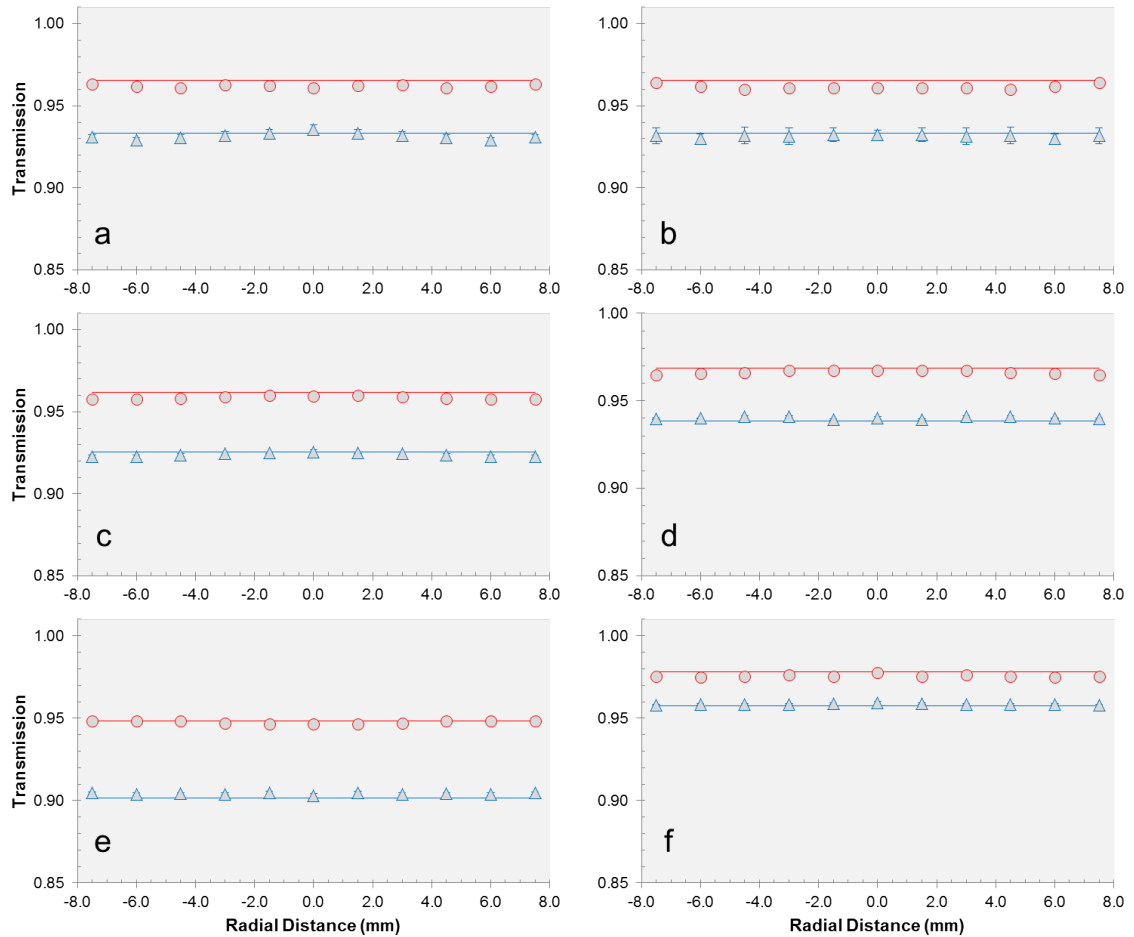


Figure 18: Measured (bullets) and calculated (lines) normalized transmission of a FS planar substrate as functions of radial distance (r) for double-sided AR-coated BK7 lens (black), single-sided rARSS FS lens (red), and uncoated FS lens (blue). (a) TE and (b) TM incident polarization at global angle $\theta = 0^\circ$. (c) TE and (d) TM incident polarization at $\theta = 15^\circ$. (e) TE and (f) TM incident polarization at $\theta = 30^\circ$. The standard deviation of the experimental measurements is the thickness of the bullets if not shown as a vertical bar.

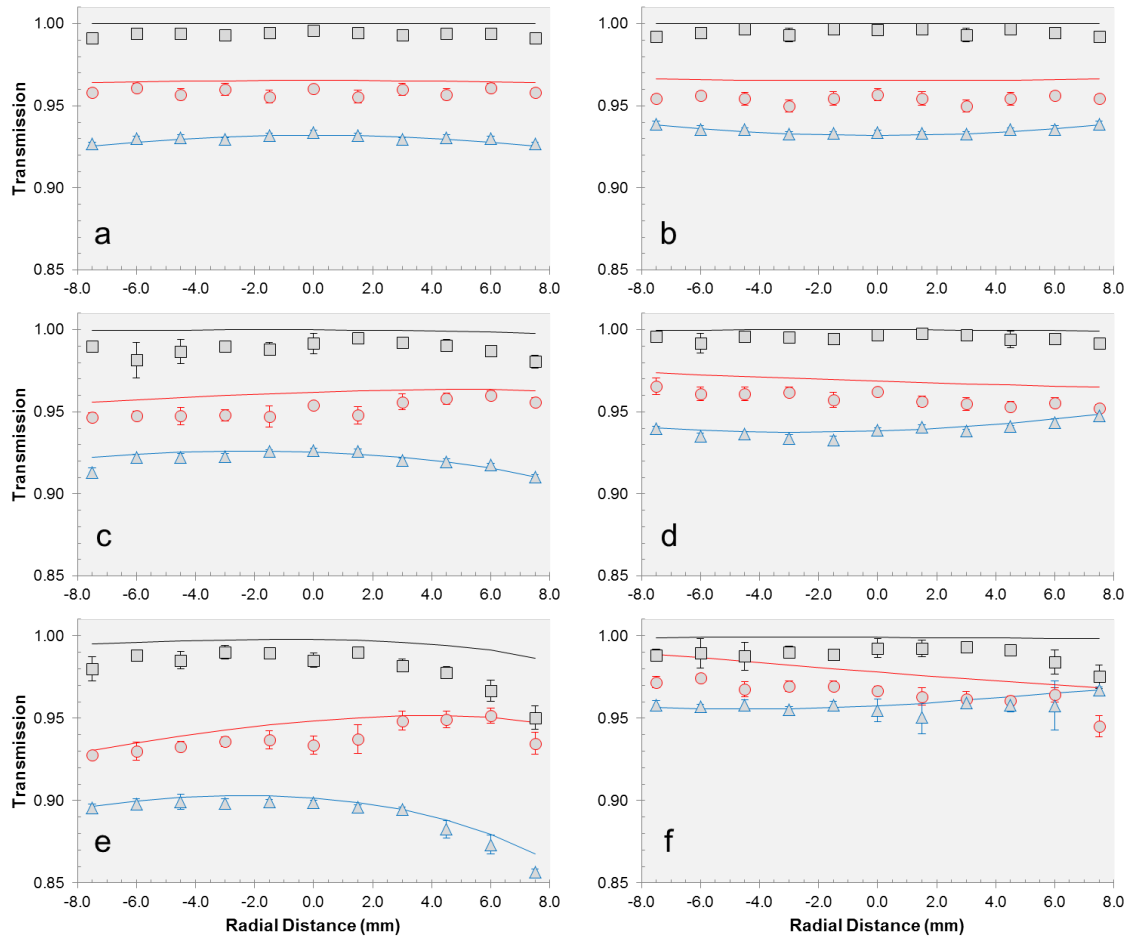


Figure 19: Measured (bullets) and calculated (lines) normalized transmission of a FS +50mm EFL PCX lens as functions of radial distance (r) for double-sided AR-coated BK7 lens (black), single-sided rARSS FS lens (red), and uncoated FS lens (blue). (a) TE and (b) TM incident polarization at $\theta = 0^\circ$. (c) TE and (d) TM incident polarization at $\theta = 15^\circ$. (e) TE and (f) TM incident polarization at $\theta = 30^\circ$. The standard deviation of the experimental measurements is the thickness of the bullets if not shown as a vertical bar.

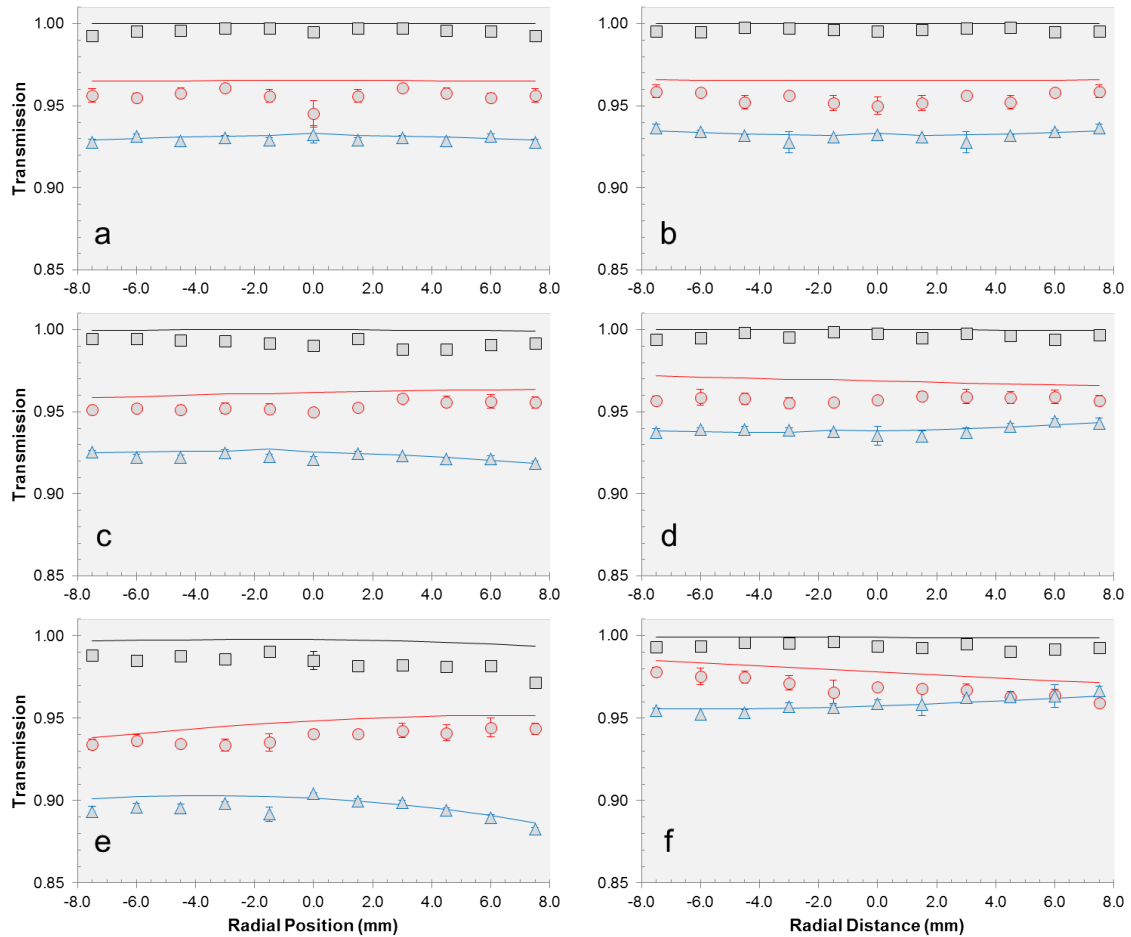


Figure 20: Measured (bullets) and calculated (lines) normalized transmission of a FS +75mm EFL PCX lens as functions of radial distance (r) for double-sided AR-coated BK7 lens (black), single-sided rARSS FS lens (red), and uncoated FS lens (blue). (a) TE and (b) TM incident polarization at $\theta = 0^\circ$. (c) TE and (d) TM incident polarization at $\theta = 15^\circ$. (e) TE and (f) TM incident polarization at $\theta = 30^\circ$. The standard deviation of the experimental measurements is the thickness of the bullets if not shown as a vertical bar.

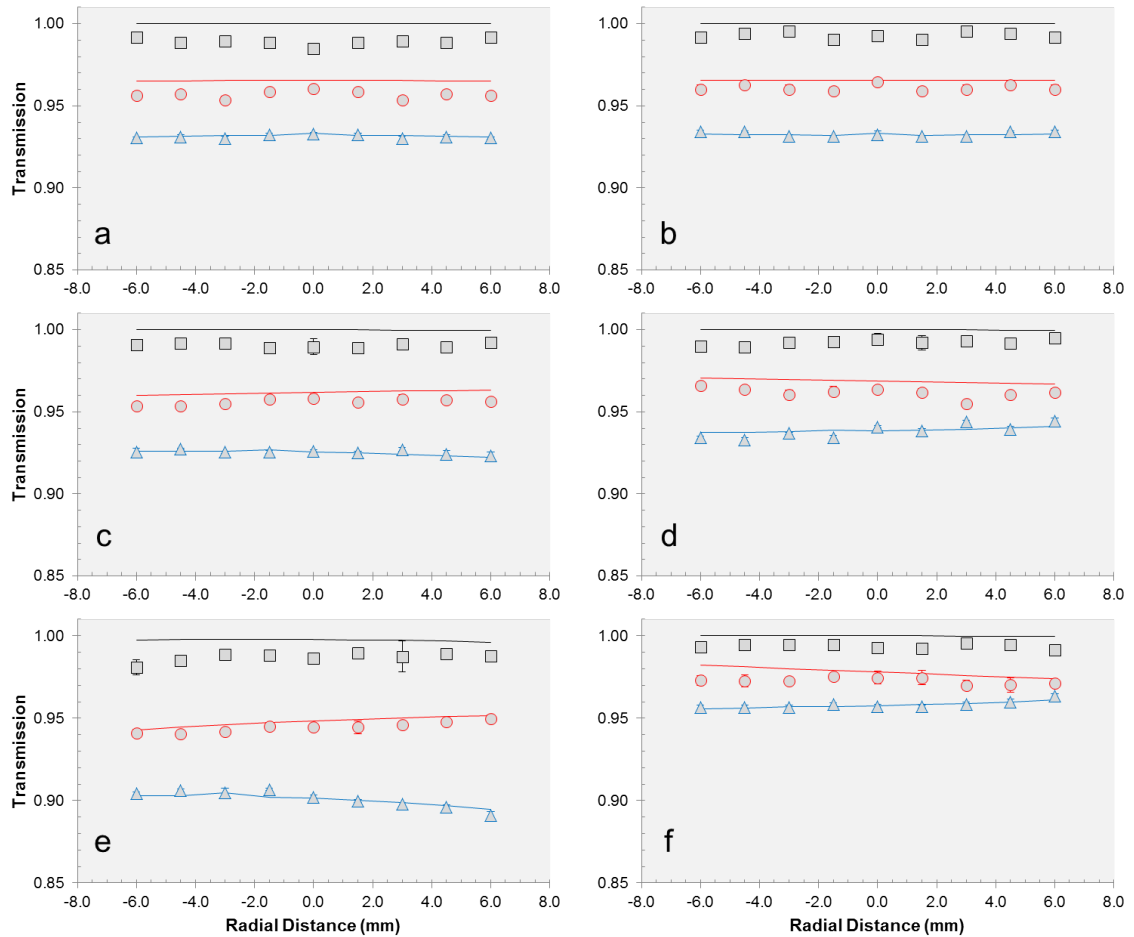


Figure 21: Measured (bullets) and calculated (lines) normalized transmission of a FS +100mm EFL PCX lens as functions of radial distance (r) for double-sided AR-coated BK7 lens (black), single-sided rARSS FS lens (red), and uncoated FS lens (blue). (a) TE and (b) TM incident polarization at $\theta = 0^\circ$. (c) TE and (d) TM incident polarization at $\theta = 15^\circ$. (e) TE and (f) TM incident polarization at $\theta = 30^\circ$. The standard deviation of the experimental measurements is the thickness of the bullets if not shown as a vertical bar.

many cases, the error bars are not visible. These error bars are present but are low enough to be obfuscated by the marker itself, and are well-below quoted measurement uncertainties.

In each plot, the uncoated, unprocessed FS lenses performed to the computation curve within the measurement uncertainty. These measurements provided further validation for the testing procedure and the computation method. In Table 5, for the TE case, the percent difference for all samples is below 1%, ranging from 0.347% for 100mm EFL at $\theta = 30^\circ$ to 0.965% for 50mm EFL at 15° . In Table 6, for the TM case, the percent difference ranges from 0.459% for 100mm EFL at $\theta = 0^\circ$ to 1.36% for 50mm EFL at 30° .

The deviation of the AR-coated BK7 lens' results from the computation curve is reduced as the curvature relaxes from +50mm to +100mm. A possible reason for this behavior may be a lack of thin film uniformity over the surface of the lens. The reduction in deviation from the +50mm to +100mm can then be attributed to the fact that maintaining thin film uniformity over a surface with higher curvature is more challenging than one with a lower curvature. It is also possible that the thin film does not match the constraints on the index of refraction and/or the thickness of the film layer for an ideal AR thin film. Since the computation model assumes these constraints to be met, and it is physically difficult to do so, it follows that the results not only may experience a deviation from the computation curve, but should be expected to do so within an acceptable tolerance. The manufacturer quotation of transmission for the AR lenses used is $> 99\%$ for up to 8° [70, 71]; the lenses perform to this tolerance for all EFLs at 0° AOI. Additionally, in each case, the results do

Table 4: Mean percent difference of measured transmission values for planar substrates

$\theta(^{\circ})$	TE		TM	
	Uncoated	rARSS	Uncoated	rARSS
0	1.58E 01	3.49E 01	1.62E 01	3.98E 01
15	1.59E 01	3.47E 01	1.94E 01	2.34E 01
30	2.95E 01	8.60E 02	9.53E 02	2.42E 01

Table 5: Mean percent difference of measured transmission values for PCX lens samples for TE polarization

Sample	$\theta(^{\circ})$	TE		
		Uncoated	rARSS	AR-coated
50mm EFL	0	8.69E-02	6.72E-01	6.27E-01
	15	1.48E-01	9.65E-01	1.10E+00
	30	4.21E-01	7.21E-01	1.48E+00
75mm EFL	0	1.34E-01	9.43E-01	4.33E-01
	15	1.70E-01	8.41E-01	7.82E-01
	30	3.83E-01	8.67E-01	1.31E+00
100mm EFL	0	5.01E-02	8.79E-01	1.08E+00
	15	4.55E-02	5.86E-01	9.24E-01
	30	4.68E-02	3.47E-01	1.05E+00

Table 6: Mean percent difference of measured transmission values for PCX lens samples for TM polarization

Sample	$\theta(^{\circ})$	TM		
		Uncoated	rARSS	AR-coated
50mm EFL	0	8.08E-02	1.21E+00	5.00E-01
	15	1.97E-01	1.10E+00	4.65E-01
	30	1.80E-01	1.36E+00	1.03E+00
75mm EFL	0	8.16E-02	1.10E+00	3.65E-01
	15	4.28E-02	1.13E+00	3.56E-01
	30	4.57E-02	9.67E-01	5.17E-01
100mm EFL	0	2.95E-02	4.59E-01	7.16E-01
	15	5.47E-02	7.20E-01	7.57E-01
	30	2.05E-02	5.51E-01	6.19E-01

follow the same trend as the computed curve. While the results may not match the transmission values of the computation, a match in trend indicates an appropriate choice of model for the AR-coated BK7 lenses.

Much like the AR-coated BK7 lenses, the etched FS lens' results show similar trends as the computed curves, but display numerically-significant deviation. As previously stated, this is an expected result due to the lack of an appropriate model for the etched surface. As the curvature relaxes from the $+50mm$ EFL lens to the $+100mm$ EFL lens, the deviation between computation and experimental results is reduced. Unlike the AR-coated BK7 lenses, it could indicate a more complicated functional relation between the lens parameters and transmission in addition to effective structure layer thickness non-uniformity over the surface as a result of the etching process.

To further investigate any complexities arising from lens parameters, the transmission enhancement of the etched surface over the bare FS substrate was determined for the lens elements as well as the flat (Eq. 102). Although the global angle, denoted by θ , was constricted to a maximum of 30° , the curvature of the surface provided additional angular deviation. The total local angle as seen by the surface is denoted by θ' . For each θ , nearly 40° of the FOV was accessed, with a total of 70° over all three θ values. Expressing the measurements in terms of θ' instead of θ allows for comparison without specifying the lens type used to obtain them. The results can be seen in Fig. 22. For a θ of 0° , the transmission enhancement results span from -20° to 20° and show symmetric curvature with growing deviation between TE and TM modes past $+15^\circ$. The values over the angular range are generally in good agreement with the theoretical expectation of 3.6%, shown as a dashed line. For a θ of 15° ,

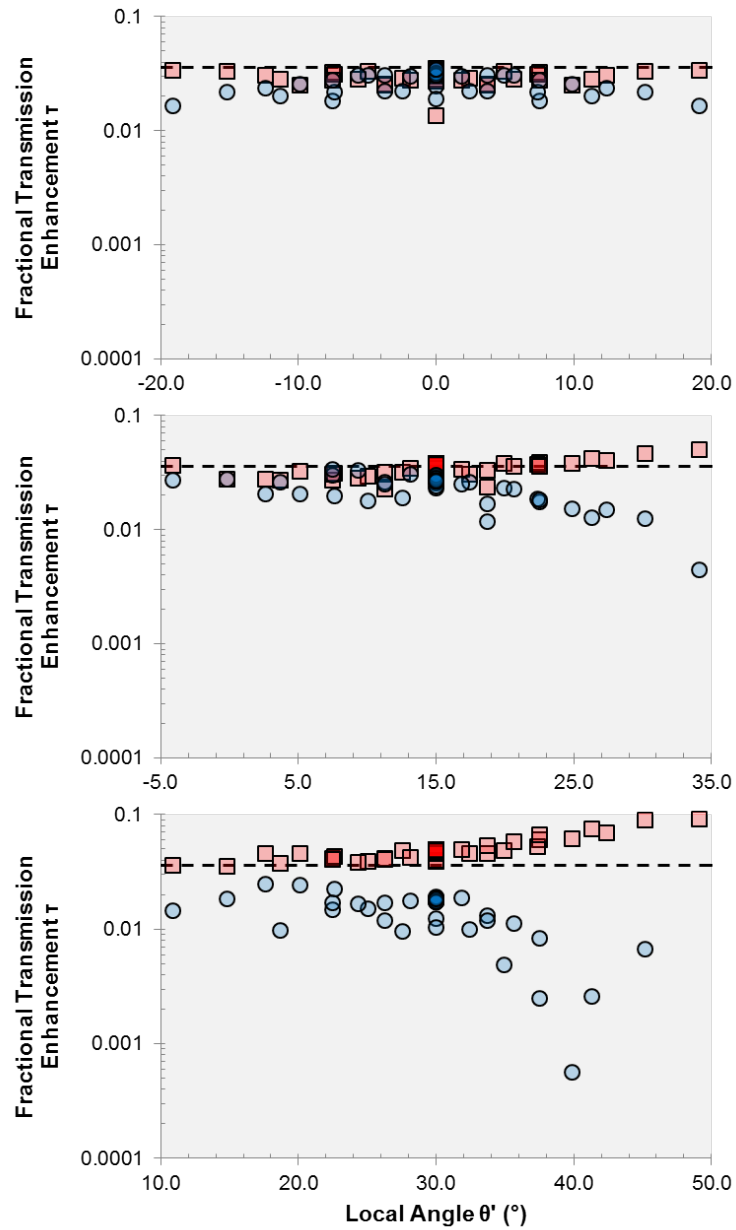


Figure 22: Plots showing fractional transmission enhancement τ as a function of θ' for a θ of 0° , 15° , and 30° across all PCX lens samples; TE mode (squares), and TM mode (circles). The dashed line represents 3.6% transmission enhancement, the theoretical limit for normal incidence of FS.

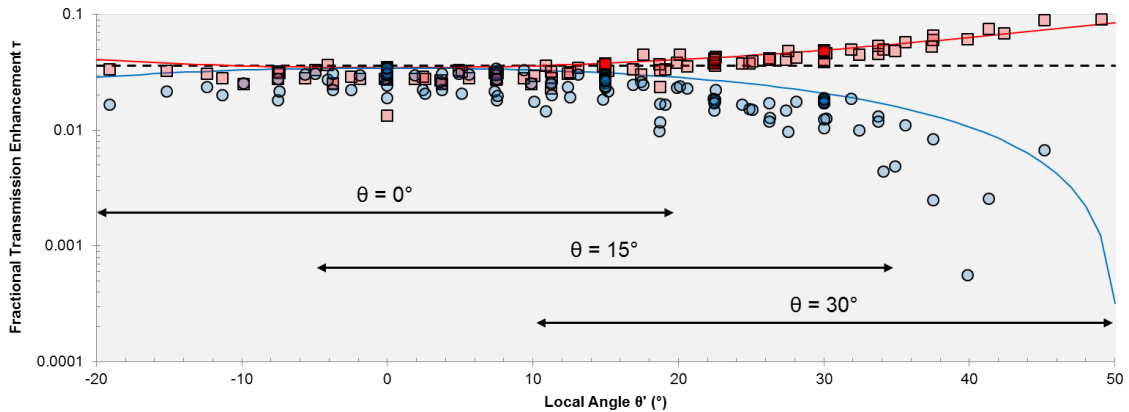


Figure 23: Transmission enhancement τ as a function of the local angle θ' across all PCX lenses tested; TE-mode enhancement (squares) and TM mode (circles). The dashed line represents the theoretical limit +3.6% transmission enhancement for normal incidence of a FS planar surface. The red line represents the TE-mode theoretical enhancement for a single-sided ideal AR thin-film-coated planar substrate over the θ' range. The blue line represents the TM mode for the same computed parameters. The θ measurement set ranges are indicated as well.

the transmission enhancement results span from -5° to $+35^\circ$. These results show an asymmetric curve with significant bifurcation between TE and TM modes, with the TE improving while the TM loses enhancement. For a θ of 30° , the results span from 10° to 50° . The TE mode is showing increased significant transmission enhancement over the normal incidence threshold of 3.6%, up to $\sim 10\%$. The TM quickly drops off as the θ' approaches the Brewster's angle of 55.5° for FS.

In order to further understand the effect of θ versus θ' on transmission enhancement, all transmission enhancement data were plotted together according to θ' . The results of this arrangement are shown in Figs. 23. Due to repeated θ' in each θ set, the results in the range of -5° to $+35^\circ$ may have data from all three θ values. It is important to note the range of 10° to 20° contains data from all three θ . The plot, when arranged in this fashion, shows no discernible plot discontinuities, nor can individual datum be

interrogated as belonging to a specific EFL or θ . Instead, a smooth transition over the whole range of -20° to $+50^\circ$ is observed.

The PCV lens samples were analyzed using the same method as the PCX lens samples. Figs. 24 – 26 show the plotted transmission values. The same comments for the coated and uncoated samples and the corresponding computed values for the PCX lenses can be made for the PCV lenses. For the lens samples with rARSS, these results differ from the PCX lens samples. There is significant deviation from the one-sided AR-coated model. This is confirmed by Tables 7 and 8, where the mean percent difference is predominately $> 1\%$ for both TE and TM polarizations and is outperformed by the AR-coated BK7 samples. These values fall within measurement uncertainty.

Again, a more appropriate metric of rARSS performance to use for comparison is the transmission enhancement. In Fig. 27 the transmission enhancement is given for all PCV lenses and grouped by θ . In Fig. 28 the transmission enhancement is presented all together along with computed transmission enhancement values from a one-sided AR-coated model. This plot shows an enhanced transmission from the bare substrate, but less effective than rARSS on a PCX lens surface. It also shows a greater spread of enhancement values as compared to PCX lens performance.

Finally, the full set of non-optimized lenses ($+50mm$, $+75mm$, $+100mm$, $-50mm$, $-75mm$, and $-100mm$ EFL) were tested in the same procedure as the PCV and PCX lenses. The transmission enhancement was found and plotted according to the θ' . The results are shown in Fig. 29. It can be observed that the results do not indicate a clear relationship with θ' as a determining parameter. Instead, the data

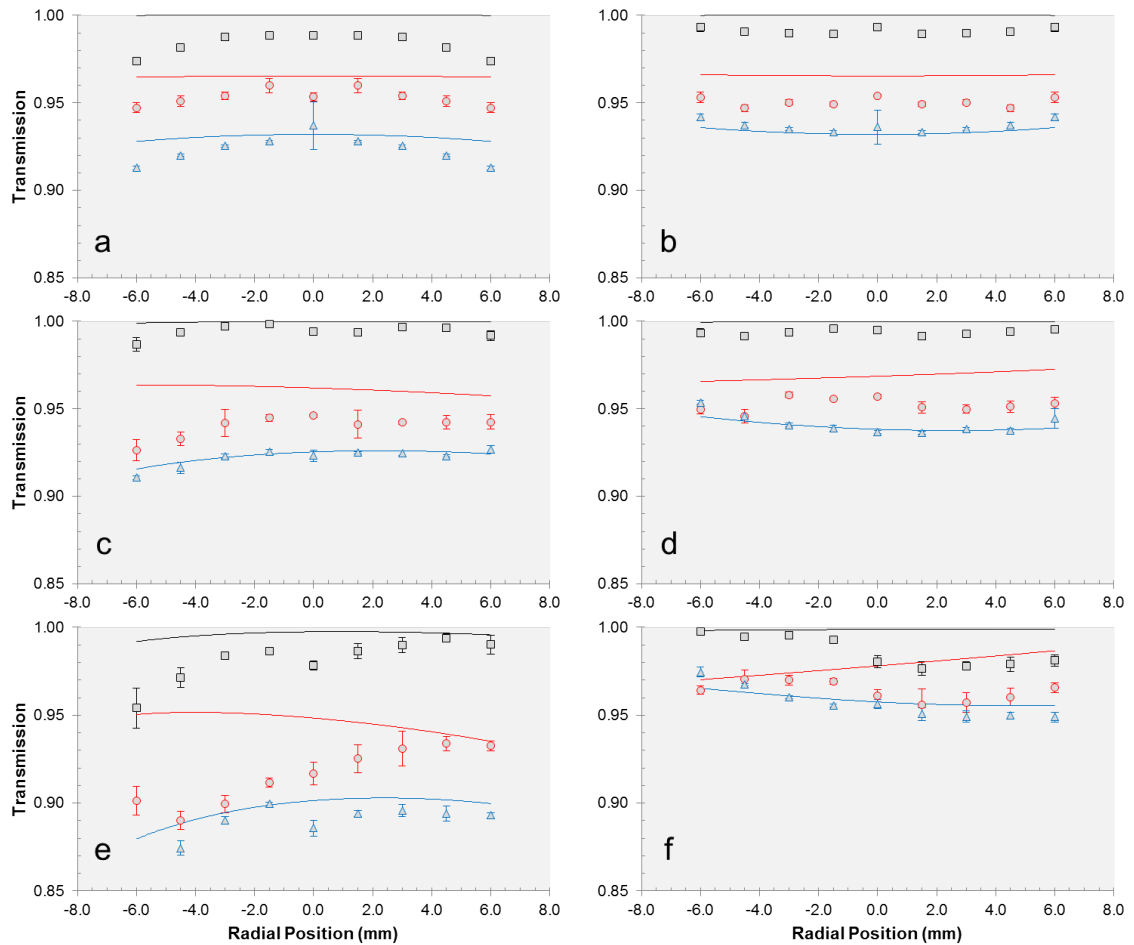


Figure 24: Measured (bullets) and calculated (lines) normalized transmission of a FS -50mm EFL PCX lens as functions of radial distance (r) for double-sided AR-coated BK7 lens (black), single-sided rARSS FS lens (red), and uncoated FS lens (blue). (a) TE and (b) TM incident polarization at $\theta = 0^\circ$. (c) TE and (d) TM incident polarization at $\theta = 15^\circ$. (e) TE and (f) TM incident polarization at $\theta = 30^\circ$. The standard deviation of the experimental measurements is the thickness of the bullets if not shown as a vertical bar.

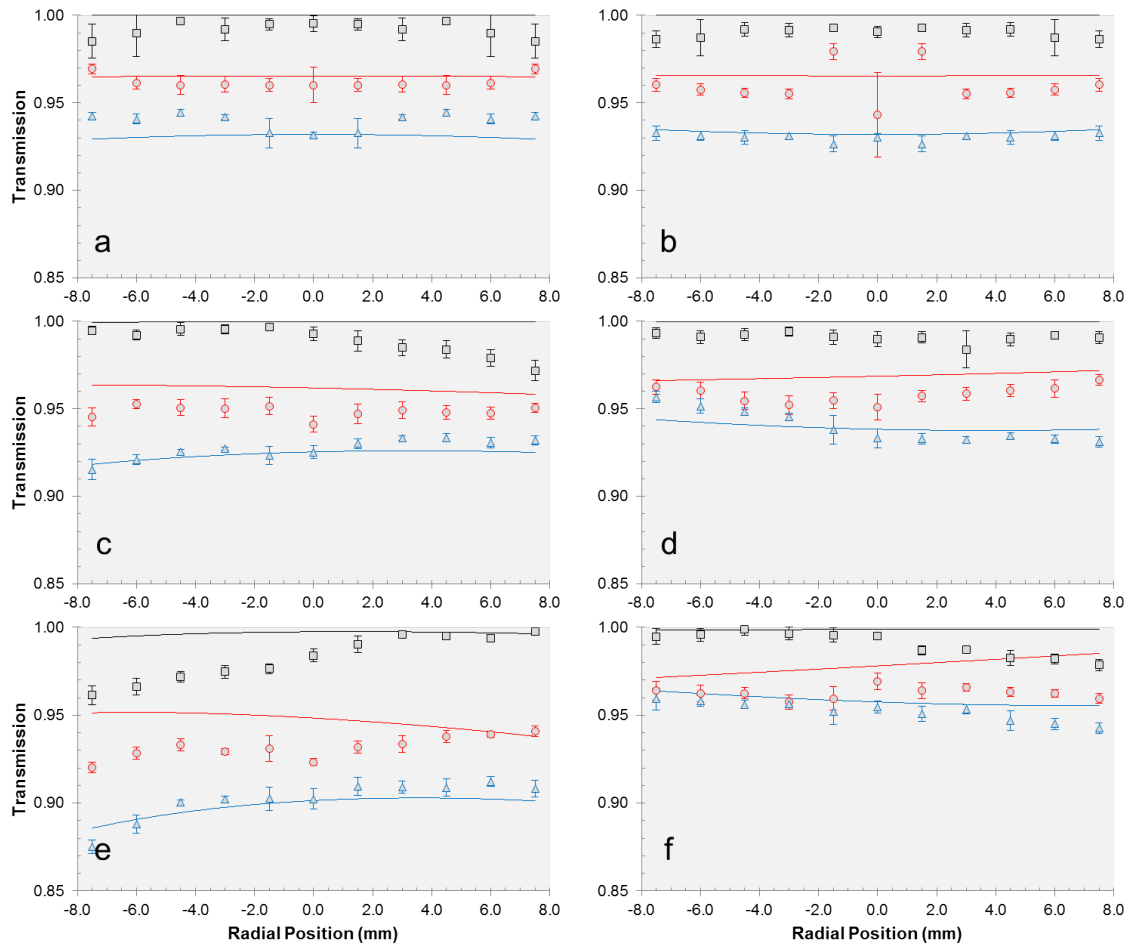


Figure 25: Measured (bullets) and calculated (lines) normalized transmission of a FS -75mm EFL PCX lens as functions of radial distance (r) for double-sided AR-coated BK7 lens (black), single-sided rARSS FS lens (red), and uncoated FS lens (blue). (a) TE and (b) TM incident polarization at $\theta = 0^\circ$. (c) TE and (d) TM incident polarization at $\theta = 15^\circ$. (e) TE and (f) TM incident polarization at $\theta = 30^\circ$. The standard deviation of the experimental measurements is the thickness of the bullets if not shown as a vertical bar.

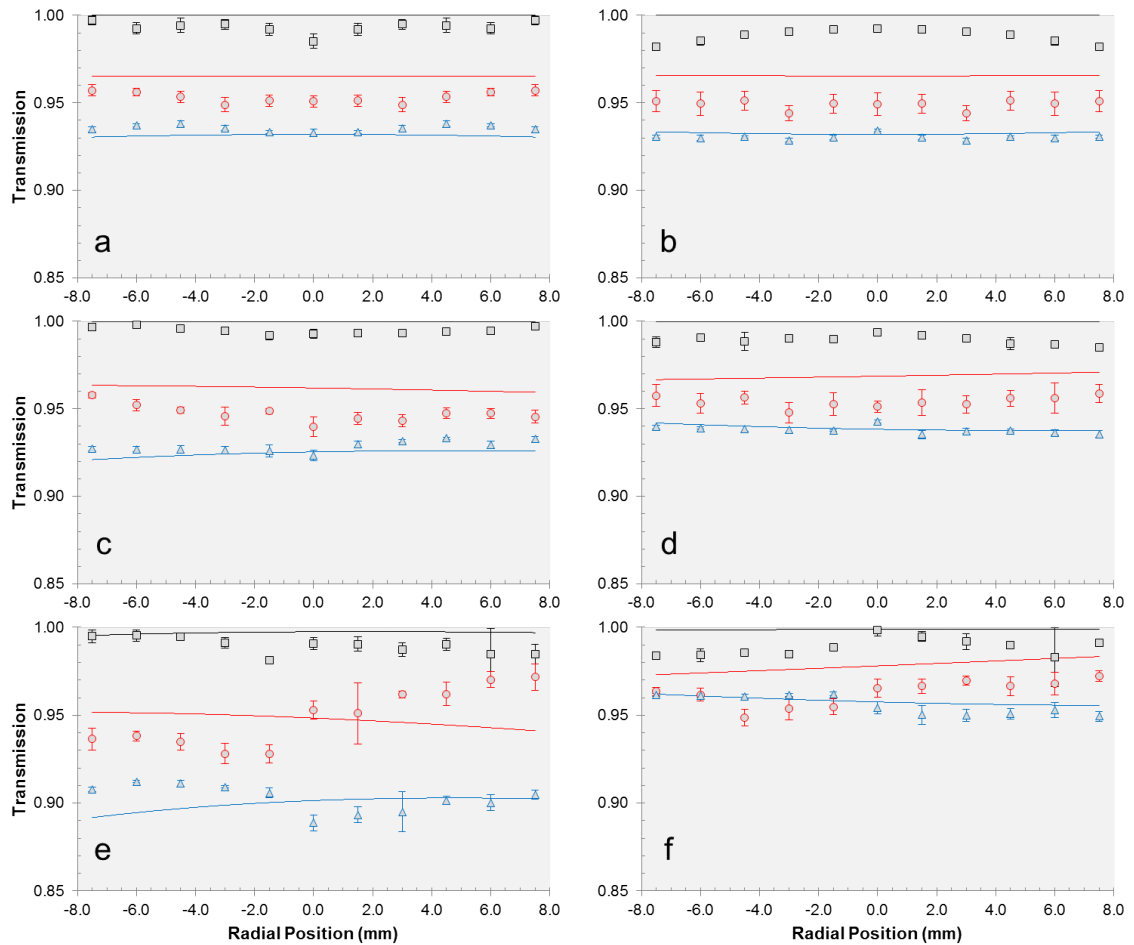


Figure 26: Measured (bullets) and calculated (lines) normalized transmission of a FS -100mm EFL PCX lens as functions of radial distance (r) for double-sided AR-coated BK7 lens (black), single-sided rARSS FS lens (red), and uncoated FS lens (blue). (a) TE and (b) TM incident polarization at $\theta = 0^\circ$. (c) TE and (d) TM incident polarization at $\theta = 15^\circ$. (e) TE and (f) TM incident polarization at $\theta = 30^\circ$. The standard deviation of the experimental measurements is the thickness of the bullets if not shown as a vertical bar.

Table 7: Mean percent difference of measured transmission values for PCV lens samples for TE polarization

Sample	$\theta(^{\circ})$	TE		
		Uncoated	rARSS	AR-coated
$-50mm$ EFL	0	8.86E-01	1.25E+00	1.66E+00
	15	2.24E+00	2.36E-01	5.37E-01
	30	1.30E+00	3.27E+00	1.46E+00
$-75mm$ EFL	0	9.47E-01	4.77E-01	8.01E-01
	15	4.18E-01	1.36E+00	1.11E+00
	30	6.44E-01	1.68E+00	1.45E+00
$-100mm$ EFL	0	4.45E-01	1.26E+00	6.69E-01
	15	4.55E-01	1.50E+00	5.06E-01
	30	1.01E+00	1.80E+00	7.44E-01

Table 8: Mean percent difference of measured transmission values for PCV lens samples for TM polarization

Sample	$\theta(^{\circ})$	TM		
		Uncoated	rARSS	AR-coated
$-50mm$ EFL	0	3.44E-01	1.60E+00	9.00E-01
	15	2.50E-01	1.71E+00	6.09E-01
	30	5.02E-01	1.48E+00	1.26E+00
$-75mm$ EFL	0	2.95E-01	1.11E+00	1.00E+00
	15	6.42E-01	1.10E+00	9.10E-01
	30	6.42E-01	1.59E+00	8.50E-01
$-100mm$ EFL	0	2.77E-01	1.71E+00	1.18E+00
	15	1.86E-01	1.51E+00	1.05E+00
	30	3.70E-01	1.58E+00	1.01E+00

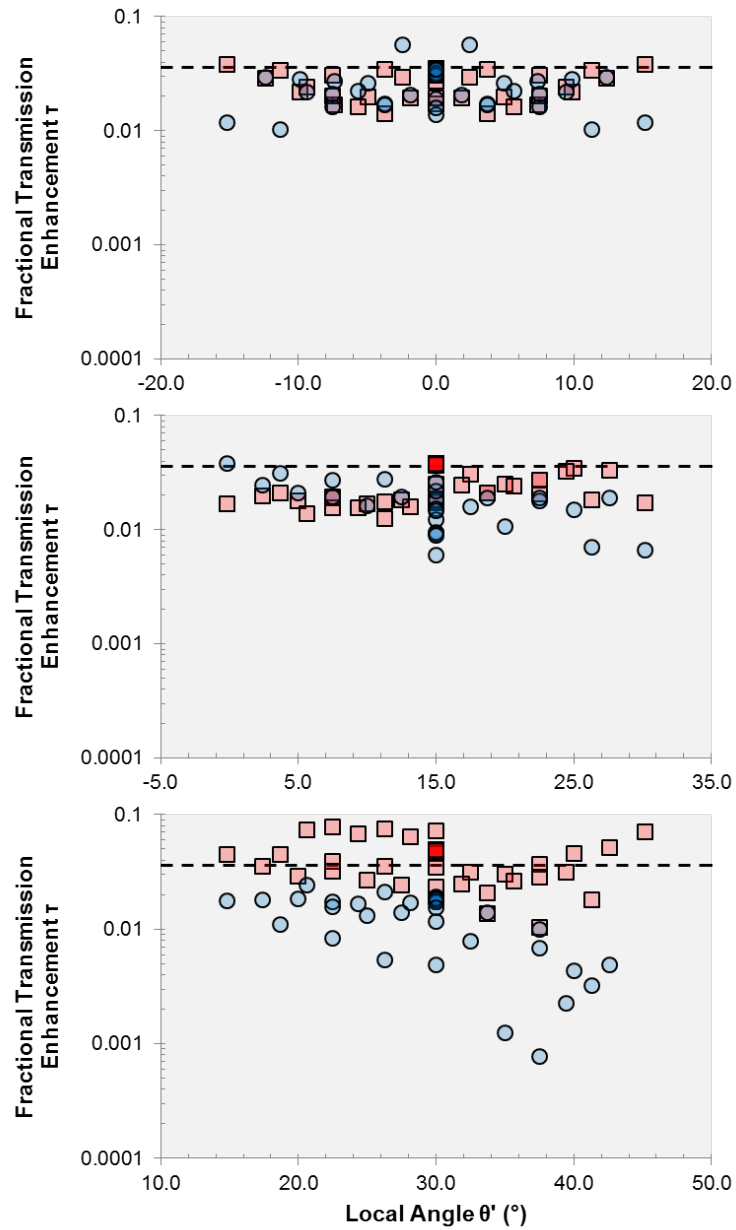


Figure 27: Plots showing fractional transmission enhancement τ as a function of θ' for a θ of 0° , 15° , and 30° across all PCV lens samples; TE mode (squares), and TM mode (circles). The dashed line represents 3.6% transmission enhancement, the theoretical limit for normal incidence on FS.

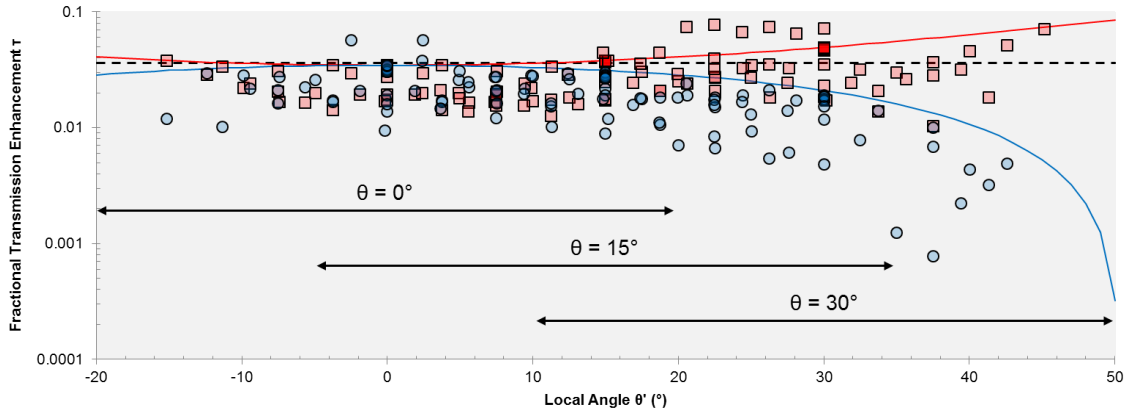


Figure 28: Transmission enhancement as a function of θ' across all PCV lenses tested; TE-mode enhancement (squares) and TM mode (circles). The dashed line represents the theoretical limit +3.6% transmission enhancement for normal incidence of a FS planar surface. The red line represents the TE-mode theoretical enhancement for a single-sided ideal AR thin-film-coated planar substrate over the θ' range. The blue line represents the TM mode for the same computation parameters. The θ measurement set ranges are indicated as well.

for the non-optimized lenses, along with the optimized cases, were re-plotted as a function of lens height. The results of this analysis are shown in Fig. 30. In this plot, the results of the optimized cases show consistent transmission enhancement over the height variable, indicating the leading parameter is θ' . For the case of the non-optimized lenses, there is a steep drop-off in transmission enhancement beginning around a lens height of 4.0mm . This would indicate the leading parameter for non-optimized lens transmission enhancement is the height of the lens rather than the θ' .

Images from SEM (Raith 150 E-Beam Lithography System) were obtained from the surface of the $\pm 50\text{mm}$ lenses in order to empirically ascertain any differences between structures across each lens from center to edge as well as across different lenses of the same EFL. These can be seen in Figs. 31 and 32.

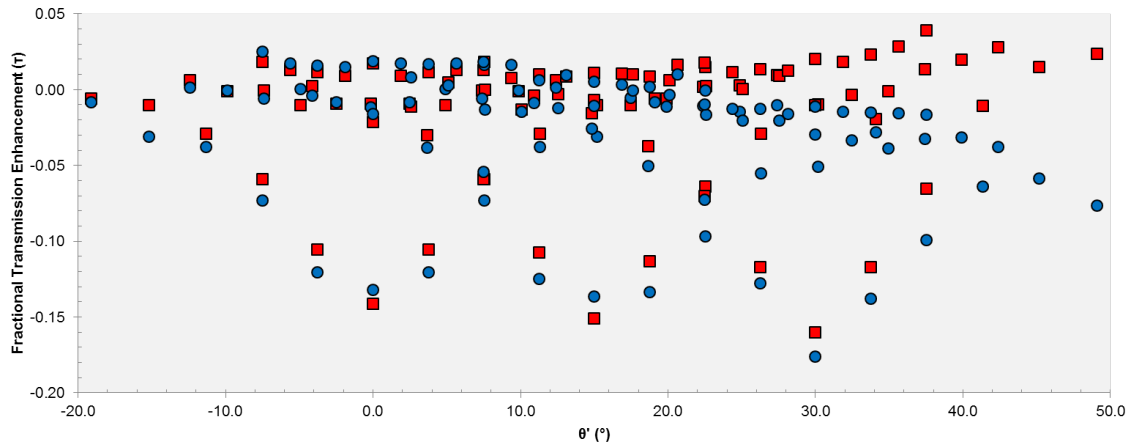


Figure 29: Fractional transmission enhancement as a function of θ' for non-optimized lenses. Enhancement data are shown with red indicating TE-mode polarization and blue indicating TM-mode polarization.

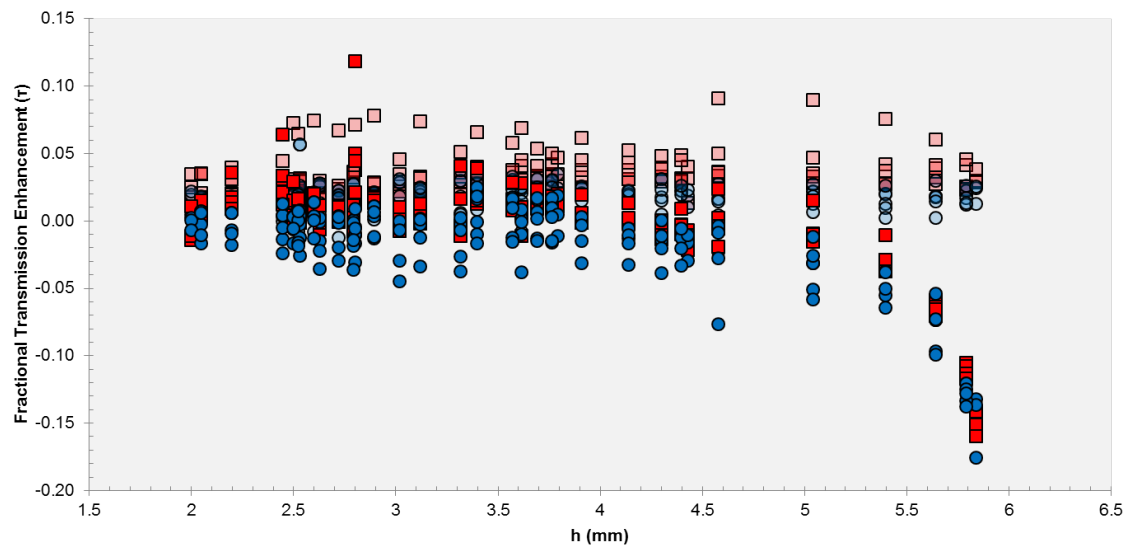


Figure 30: Fractional transmission enhancement as a function of lens surface height at the measurement locations for both optimized and non-optimized lenses. Enhancement data for the optimized lenses are shown as transparent markers with red indicating TE-mode polarization and blue indicating TM-mode polarization. Enhancement data for non-optimized lenses are shown as solid markers with the same color indicators as for the optimized lenses.

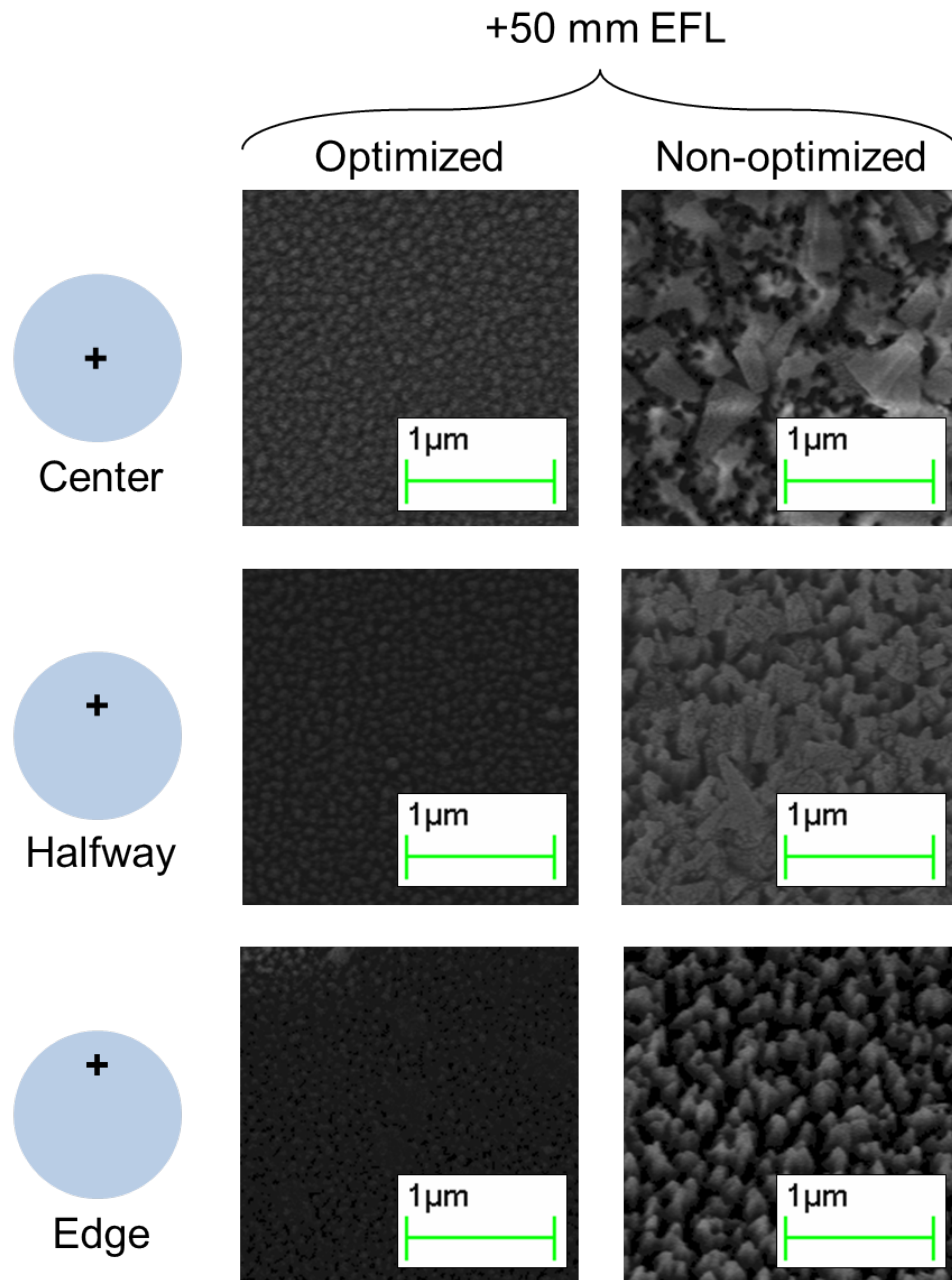


Figure 31: SEM images showing center, halfway between center and edge, and edge surface structure on +50mm EFL lenses. The left column shows the optimized sample, and the right column shows the non-optimized sample.

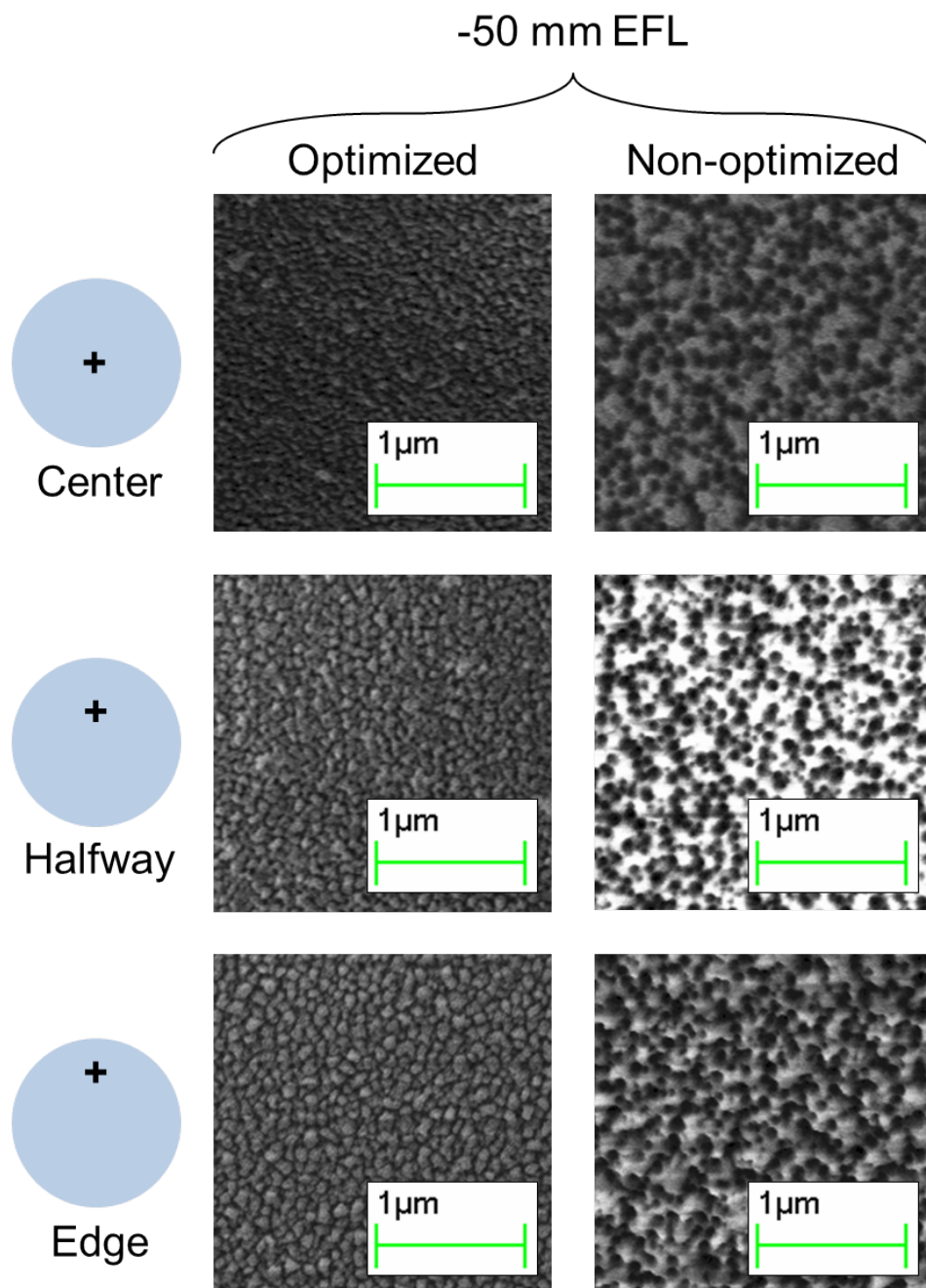


Figure 32: SEM images showing center, halfway between center and edge, and edge surface structure on -50mm EFL lenses. The left column shows the optimized sample, and the right column shows the non-optimized sample.

Starting with the $+50\text{mm}$ EFL lenses, the structures on the optimized sample do not appear to vary in size across the lens surface. Small differences of the pillar direction with respect to the center sample can be observed, faintly in the halfway sample and more so in the edge sample. These directionality differences are more exaggerated in the non-optimized sample. For both samples, the pillars are isotropically-formed. In the non-optimized samples, the center image shows plateau-like peaks with large debris sitting on top of the structure. The shape of the debris, along with the structures, indicate peaks may have originally formed and then were broken off. Similar debris is also found in the halfway image. Plateaus are still visible, but appear to have more variation in topography. The edge shows no debris, and pillars closer to those found on the optimized sample are starting to form. All structures found on the non-optimized sample are much larger than the structures found on the optimized sample.

The SEM images from -50mm EFL lenses, like the $+50\text{mm}$ EFL lenses, vary greatly between optimized and non-optimized. The optimized sample shows a small variation in size across the lens. Structures in the center are visibly smaller than halfway and edge structures. Edge structures are larger than halfway structures. The shape, density, and overall size of structures on the -50mm EFL lens matches that found on the $+50\text{mm}$ EFL lens. Orientation of the structures are difficult to see due to the density of the structures. The PCV non-optimized sample images show no debris compared to the PCX non-optimized sample images. The structure formation between the center, halfway, and edge images grows in height from flatter plateaus to small peaks. The same isotropic orientation is observed in the -50mm

EFL non-optimized lens as was observed in both $+50mm$ EFL lenses.

2.5 Conclusions of Performance of Random Anti-Reflection Surface Structure on Singlet Lenses

The viability of rARSS as a surface treatment to reduce Fresnel reflectivity at the surface of spherical lens elements has been compared to ideal SLAR thin-film coatings at various AOI and both TE and TM source polarization orientations. Theoretical ideal SLAR coating performance was shown to be a useful metric for rARSS on these surfaces. Further, a methodology has been designed and tested in order to evaluate the scalar polarized transmission properties of rARSS on spherical lens topography. This methodology is also scalable to other topographies, for example with combinations of surfaces such as microlens arrays.

To perform this work, six FS lenses of EFLs ± 50 , ± 75 , and $\pm 100mm$ were etched in an RIE-ICP process to develop rARSS optimized for 633 nm with planar substrates. These lenses and planar substrates were tested alongside unprocessed FS lenses and planar substrates as well as commercially available AR-coated thin-film lenses of identical EFL for transmission over most of the profile of the substrates and a range of AOI. Measured transmission and transmission enhancement were compared against theoretical values as both a method to evaluate results and to establish a metric for comparison. In addition, six additional FS lenses of the same EFLs were etched in a non-optimized process for the test parameters.

While realistic SLAR coatings can meet the physical criteria to produce 50% transmission enhancement at a FOV of $\pm 34^\circ$, there are nontrivial manufacturing challenges

to overcome in order to create such thin films optical power elements. The rARSS process used here has only been optimized for planar substrate transmission enhancement and was not specifically optimized using considerations to accommodate nonplanar topography. The results show that the isotropic plasma etch is forming random features that can perform as AR layers without large deviations due to the radius of curvature of the optical elements. Thus, rARSS is a good candidate for spherical lens AR surface treatment for wide-angle FOV applications.

It has also been shown that the rARSS transmission enhancement approaches that of a SLAR coating for both incident polarizations over a minimum of $\pm 30^\circ$ FOV for PCX spherical lenses. The advantages of using a rARSS surface treatment, such as ease of fabrication and resistance to laser and thermal damage, make this solution a realistic alternative to coatings when coupled to the performance shown here. Results have been presented showing rARSS treatments to be insensitive to curvature differences between PCX spherical lens elements and primarily dependent on the AOI at the local surface normal.

For PCV lens elements, transmission enhancement has been found for rARSS on these surfaces. While it does not approach the enhancement found for a PCX lens, performance does improve over the untreated surface. The loss of enhancement compared to a PCX lens with rARSS is most likely due to the concave topography. More importantly, the testing method and metrics used to create and compare these measurements have shown to be able to give useful performance information critical to an optimization feedback loop for maximizing transmission enhancement.

For non-optimized lens elements, the transmission enhancement was found and

compared to elements from an optimized process. While the θ' was found to be a controlling parameter in the transmission enhancement of optimized lens elements, the height of the lens was the controlling parameter for the non-optimized lens. This would indicate that an optimized etch recipe for a planar substrate can be transferred to a curved surface, but optimized parameterization is limited by the height of the substrate to be etched.

Monitoring the performance of the TM-polarized light transmission enhancement enabled direct comparisons between the performance of rARSS lenses, SLAR computations, and commercially available AR coatings. The choices of these metrics can be adjusted to the specific application and can define a practical value for FOV evaluations.

Empirical observations were made from SEM images collected from $\pm 50mm$ EFL optimized and non-optimized lenses. Structures on both optimized $50mm$ EFL lenses were similar in shape, density, and size. Small size changes were observed across the optimized lens samples. The non-optimized samples each had unique structure. Both optimized and non-optimized lens samples showed evidence of isotropic pillar formation.

The similarity of the pillar formation on both optimized lenses and minimized variations between center and edge indicate substrate thickness may not affect the structure in the etching process for optimized etch recipes. This supports earlier conclusions based on the lack of a relationship between substrate thickness and transmission enhancement for the same recipes. The observed effect of substrate thickness on the structure formation for the non-optimized samples is unclear, but a few comments can

be made. The debris arrangement, variation of shape and size, and breakage evenness on the PCX non-optimized lens would indicate size of the pillars before breaking off shrunk from center to edge. The observation of height growth from center to edge in the PCV non-optimized lens mirrors the PCX lens. The substrate thickness can then be inversely correlated to pillar size; however, without further investigation, no causal affects can be validated.

Given the empirical trend towards isotropy of the pillar orientation, the optimized samples indicate the transmission enhancement for a normally-incident source over the profile of the lens behaves as a planar substrate with varying AOI may be because the structure on the surface of the lens is oriented as it would be on a planar substrate. To restate, if a planar substrate with rARSS on the surface could be spherically curved with structures intact, it would be expected to look and perform similarly to a spherical lens with rARSS. Like the substrate thickness, this is only a correlated affect, and cannot be claimed to be the sole dependency.

While the individual contributions of surface orientation and substrate thickness cannot be de-correlated, it can be said the etching process used in this work to produce rARSS on curved substrates is not anisotropic as previous investigations on planar substrates claim, but rather isotropic. To validate this further, the non-optimized samples show this effect on a larger scale. In each non-optimized lens, the orientation of the pillars follow the normal to the surface curvature.

In order to fully de-correlate surface orientation and substrate thickness as a dependency in structure formation and subsequent transmission enhancement, the same testing procedure should be performed on prisms of varying angle with rARSS in the

same etching process. Comparisons within and across prism samples would provide isolation of variables sufficient to determine contributions to transmission enhancement and begin to allow for full optimization of etch recipes for optical power elements.

Scattering losses from random surface structures are important as well. In particular, the bi-directional (forward and reflected) scatter determination is very valuable in order to quantify wide-angle and near-focus optical intensity distribution as well as for comparison to thin-film performance. Weathering of rARSS is of concern to field users because of possible contamination and alteration of the rough surfaces in the presence of harsh environments or standard laboratory conditions. Some of these issues are addressed in recent work [13].

CHAPTER 3: TRANSMISSION AND BEAM PROFILE PERFORMANCE OF DOUBLET LENSES

3.1 Introduction

In this chapter, a study of the transmission performance of multiple surfaces of rARSS on spherical lenses in doublet configurations is presented. The transmission performance was computed in order to construct a comparison metric for the evaluation of future optical power elements. In addition to rARSS spherical lenses, commercially-obtained AR-coated BK7 spherical lenses and uncoated FS spherical lenses were tested with the same procedure. Previous analysis of performance of the singlet lenses allowed for additional comparison in order to identify deviation from expected values.

Beam profile performance was tested for the same doublet configurations. Beam propagation computations provided a comparison metric. Beam spot sizes were used to compare profile performance across samples. Two evaluation methods were applied in analysis, allowing for the minimization of systematic deviation from expected values.

3.2 Experimental Implementation

The set of lenses used in the singlet experimental measurements were also used to create pairs of lenses in a doublet lens configuration. Instead of single lens elements, each PCX lens was matched with an equivalent EFL PCV lens of either AR-coated

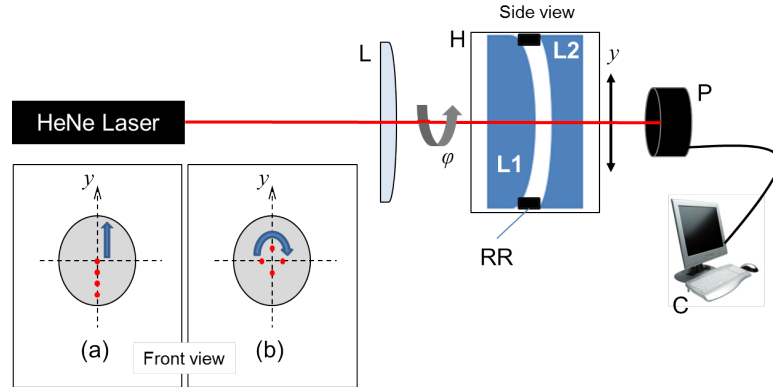


Figure 33: Experimental layout used to measure localized transmission of rARSS lens doublets: L, $+100\text{mm}$ EFL PCX lens that is focusing the incident beam to a $96\ \mu\text{m}$ spot size at the front surface of the test lens; H, the test lens holder; L1, positive lens under test; RR, a retaining ring with a thickness of 2.0mm ; L2, negative lens under test; P, photodiode detector; C, data-collecting PC. H rests on a kinematic stage, allowing (a) translation along the vertical coordinate y and (b) rotation around the azimuth angle ϕ .

BK7, PCV rARSS FS, or plain FS. This arrangement created a set of results identifying any relationships between multiple optical elements with and without rARSS surfaces. This also allowed for smaller beam walk in order to avoid detector adjustment.

To ascertain beam performance with transmission and beam profile measurements, the experimental implementation remained the same as with the singlet transmission measurements. A few changes were made to accommodate the doublet. The plano side of each PCX lens faces the incident beam at the test site. A 2.0mm retaining ring (RR) was then sandwiched between the curved surfaces of the PCX and the PCV lens elements. The beam was then allowed to propagate a short distance to the photodiode used in measurements of singlet lenses. The altered experimental arrangement is shown in Fig 33. EFLs of doublet configurations are shown in Table 9. This shows the doublets do not act as non-powered elements when placed in combination.

Table 9: EFLs of doublet configurations

Singlet EFL (mm)	Lens Pair Material	Doublet EFL (mm)
50	BK7-BK7	907.96
	BK7-FS	773.00
	FS-BK7	1213.5
	FS-FS	897.03
75	BK7-BK7	2313.6
	BK7-FS	1878.5
	FS-BK7	2981.5
	FS-FS	2296.3
100	BK7-BK7	4354.5
	BK7-FS	4032.7
	FS-BK7	4684.5
	FS-FS	4314.2

Transmission measurements followed the same protocol as singlet lenses. Since extensive AOI testing has already been performed for the singlet lenses, the doublet configuration testing was restricted to normal incidence only. Data acquisition parameters used in singlet measurements were also used for the doublet configurations.

For beam profile measurements, a scanning-slit beam profiler (Thorlabs BP209-IR) [73] was used to acquire this data. The profiler was placed $100mm$ away from the test site. This distance allowed for changes in the profile between doublets to be more easily detected while capturing deflected off-axis beams without needing translational adjustment. Profiles were collected for each radial position following the corresponding transmission measurement. An additional profile was acquired with no lens in the test mount. Beam profiler resolution is rated at $1.2\mu m$.

3.3 Computation of Transmission and Beam Propagation Through Doublet Lenses

To calculate transmission through doublet lenses, the same computation methods employed to calculate singlet lens transmission were used. The transmission values from the Fresnel equations were determined, and the bulk transmission was calculated using the exact slab solution for the doublet lens configuration.

Ray trace comparison was performed in OSLO ray trace software in order to ascertain ray deflection as a result of the translation of the matched lens pair. Fig. 34 shows a sample ray trace through a 50mm EFL matched pair of BK7 lenses for a translation from 0.0mm to 9.0mm in 1.5mm increments. This sample configuration produces the highest ray deflection out of all configurations due to the higher index of refraction and the smallest radius of curvatures on the concave/convex surfaces. In an empirical observation, no major complications arising from ray deflection through the sample arrangement were found. The same observation can be then applied to all other configurations.

A point-spread function (PSF) analysis was also performed in OSLO. The simulated PSF for the unobstructed beam is shown in Fig. 35. This PSF has been normalized to a value of 0.5235. The PSF displays a typical Gaussian profile with a faint Airy ring approximately 0.5mm from the central peak. The PSF plots for 50mm EFL configurations of BK7 PCX with BK7 PCV normalized to 0.4055, BK7 PCX with FS PCV normalized to 0.3814, FS PCX with BK7 PCV normalized to 0.4642, and FS PCX with FS PCV normalized to 0.4324 can be seen in Fig. 36. Again, apart from

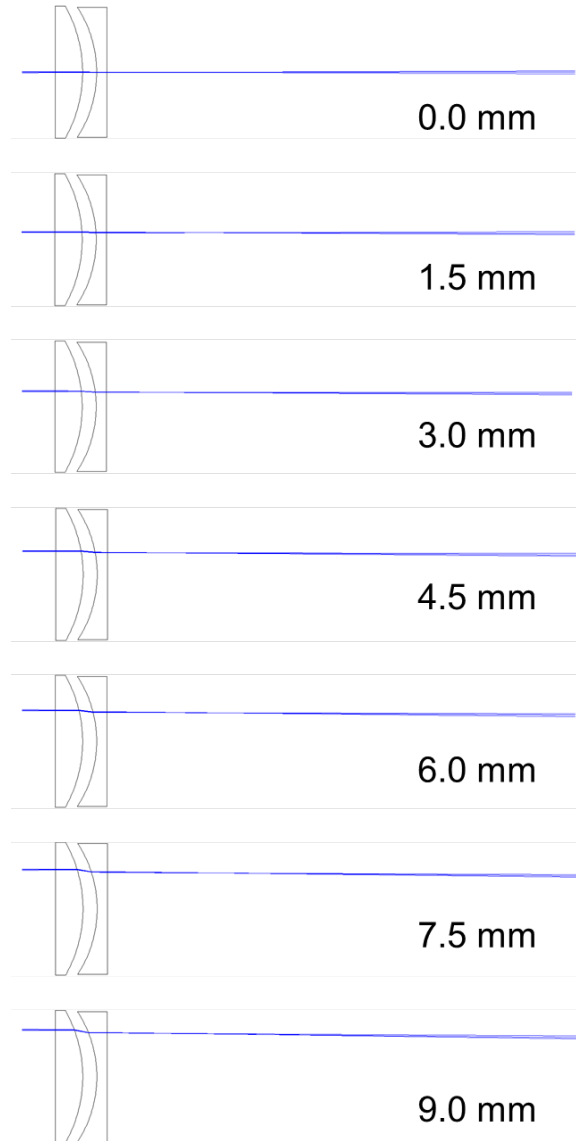


Figure 34: Ray trace performed in OSLO of a 50mm EFL matched pair of BK7 lenses from the plano surface of the PCX lens to the detector plan. The images show the translated matched pair starting at the top with 0.0mm translation and moving down in 1.5mm increments to 9.0mm .

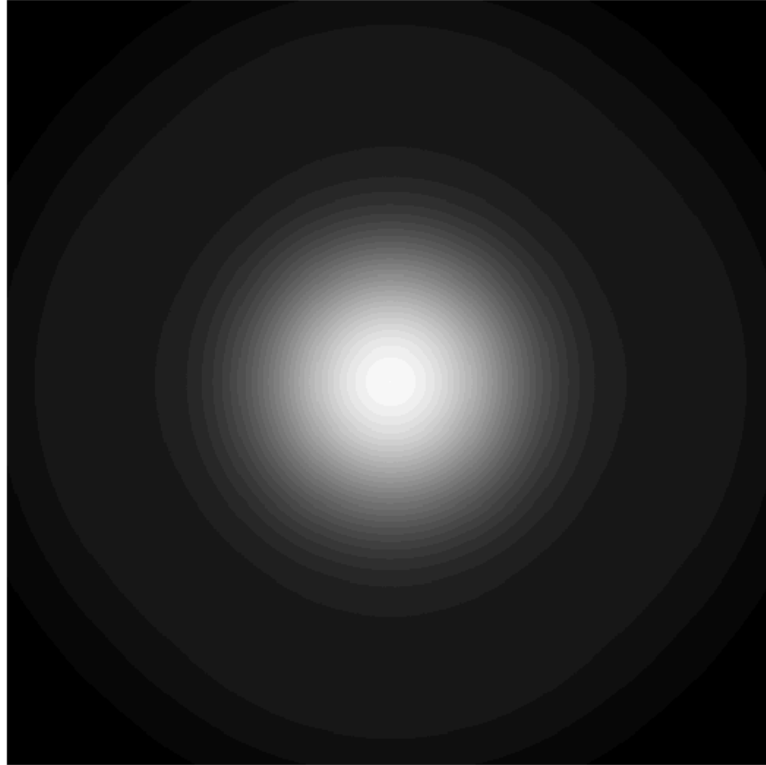


Figure 35: Simulated PSF of unobstructed beam at the detector surface. The PSF has been normalized to a value of 0.5235.

affects attributable to vertical translation of the matched pair, no major aberrations were found in empirical observations. The same conclusions can be made for the 75mm and the 100mm EFL sets.

To quantify beam aberrations, Seidel wavefront errors were computed in OSLO. As with earlier ray trace results, any aberration values found for the 50mm would be more exaggerated as compared to 75 and 100mm EFL matched pairs. Due to this, only 50mm EFL matched pairs were computed, shown in Table 10. Identical values were found over the lens profile (i.e. W040 for 0.0mm for the BK7-BK7 matched pair is equivalent to W040 for 9.0mm for the same matched pair). These values indicate negligibly-low aberrational effects at the detector plane for all matched pairs.

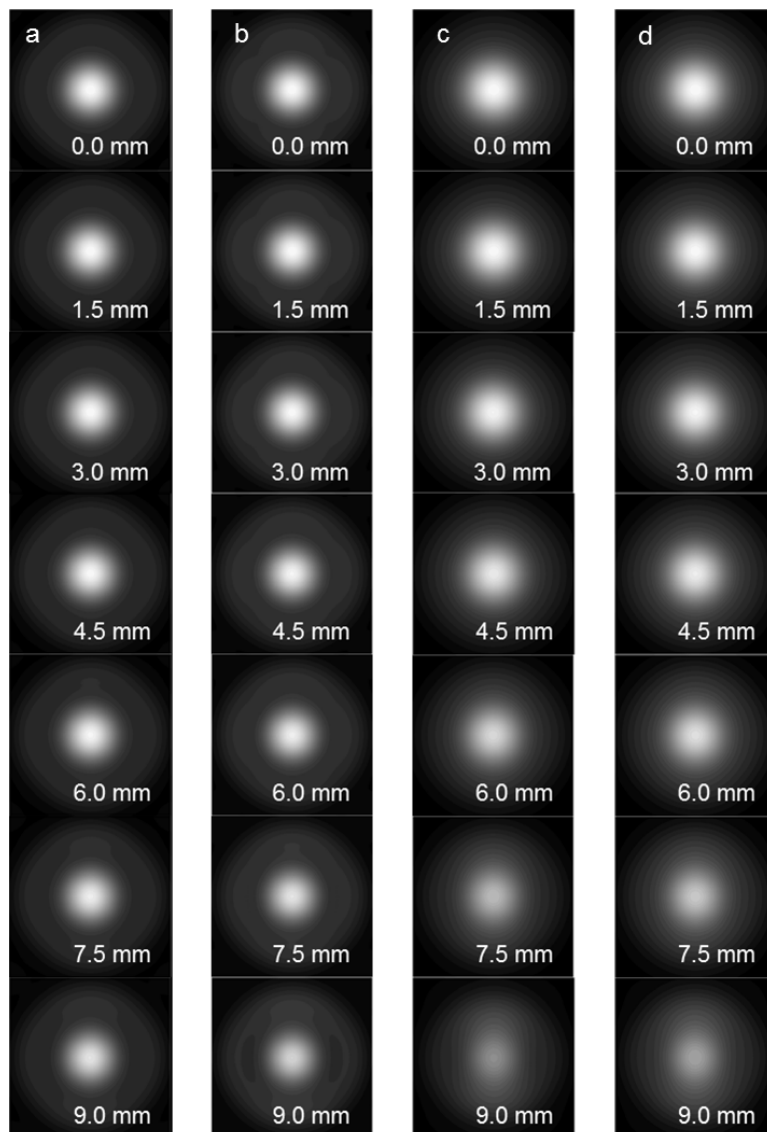


Figure 36: Point-spread functions (PSF) of 50mm EFL matched pairs, The images show the translated matched pair PSF starting at the top with 0.0mm translation and moving down in 1.5mm increments to 9.0mm. (a) BK7 PCX with BK7 PCV normalized to 0.4055, (b) BK7 PCX with FS PCV normalized to 0.3814, (c) FS PCX with BK7 PCV normalized to 0.4642, (d) FS PCX with FS PCV normalized to 0.4324.

Table 10: Seidel wavefront errors for +50mm EFL matched pairs

Lens Pair	Seidel Wavefront (λ)				
	W040	W131	W222	W220	W311
BK7-BK7	2.54E-05	8.91E-09	2.28E-12	1.63E-12	-6.08E-17
BK7-FS	2.55E-05	9.36E-09	2.57E-12	1.77E-12	1.17E-16
FS-BK7	2.55E-05	1.00E-08	3.81E-12	2.47E-12	1.84E-15
FS-FS	2.56E-05	9.88E-09	3.36E-12	2.21E-12	1.11E-15

The computation for beam propagation was also constructed in Matlab. A script iterated through each lens combination. For each individual lens combination, the propagation matrix was assembled. The propagation matrix for each surface as well as free space between each surface was calculated and assembled using the arrangement outlined in 1.5.2. The complex radius of curvature at the detector surface was then calculated, and the beam spot size extracted. A similar computation was also performed in OSLO ray trace.

Skew Gaussian beam profiles, which are realistic in systems such as these, are profiles where the peak of the profile is either situated to the left or right of the center of the profile distribution. The major contributor of skew in this work is the 0.5° to 2° tilt of elements in the system in order to prevent back reflections to the laser cavity. Thus, if this is not carefully accounted for, the skew in measured data can obscure any useful physical interpretations.

Two possible approaches were identified to treat skew Gaussian profile data. One is to compute the tilt in elements prior to the test mount. This is difficult to do; while commercial lenses are generally well-documented by a manufacturer, commercial polarizers, such as the one used in this work, have construction details not readily available from manufacturers. Another approach is to simply normalize any beam spot size measurements from test elements by the beam spot size measurement made without any test elements, thus removing systematic effects. Since the tilt in earlier elements will be present in all profile measurements, the effect will be canceled out, and the results analyzed in this way will be comparable to computations.

Given the skewed profiles, there were two additional approaches identified for ex-

tracting the beam spot size information. The first method, referred to as the Gaussian fit method, uses a curve-fitting tool in Matlab to find the Gaussian function for the profile measurements. The beam spot size was then extracted from the fit coefficients.

The curve-fit function as given by Matlab is

$$Y = \sum_{i=1}^n a_i \exp\left(-\left(\frac{x-b_i}{c_i}\right)^2\right), \quad (181)$$

where Y is the value for a given position x , a_i is the peak distribution value, b_i is the spatial offset of the peak distribution from $x = 0$, and c_i is a value relating to the distribution width. The subscript refers to orders of fits in the case a given profile measurement has multiple modes. In this work, only one mode was observed in measured data. After equating this expression with the corresponding expression for the profile of a Gaussian beam and some algebraic manipulation, the spot size is given as

$$w_d = \sqrt{2} c_1, \quad (182)$$

where w_d is the spot size at the detector for a given arrangement of test elements. The main advantage of this method is noise insensitivity; however, a drawback is the tendency to overestimate the spot size measurement.

Another way to extract beam spot size measurements from measurement data is to calculate the width of the distribution at half of the peak height. This value, commonly referred to as full-width at half-max (FWHM), has higher sensitivity to noise in the measurement data than the fit method. It also produces a value closer to reality, since it recognizes the skewed peak and is taken directly from the data. After

the FWHM is found, the spot size is given as

$$w_d = \frac{FWHM}{2\sqrt{2}}. \quad (183)$$

Using both methods, along with normalization, beam spot size measurements can be both appropriately interpreted and compared with computations.

An advantage of using both methods, apart from determining beam skew, is to also grade aberrations. The shape of the beam in a transverse direction will be affected by transverse aberrations. Any aberrational changes between radial positions or lenses will be detectable by a change in beam size and skew. Thus, aberrational differences between uncoated and rARSS FS lenses will be detected as not only a change in beam size, but an increase/decrease of difference between the Gaussian fit and FWHM analysis results.

To verify the beam profile measurements in order to compare them to computation, profiles were measured with no test elements. Earlier elements in the system were tilted in order to prevent back reflections into the laser source cavity. Thus, the measured beam spot size was expected to be slightly lower than predicted. The measured beam spot size was found to be $850.6 \mu m$ using the Gaussian fit method and $841.2 \mu m$ using the FWHM method. The computed beam spot size based on Gaussian propagation done in Matlab was calculated to be $882.6 \mu m$. A visual comparison of the raw and computed profile data is shown in Fig. 37.

As an additional comparison, beam spot sizes were computed in OSLO ray trace software. A Gaussian ABCD matrix method function similar to the one presented in Chapter 1 was used. Values were found to differ from those produced from Matlab

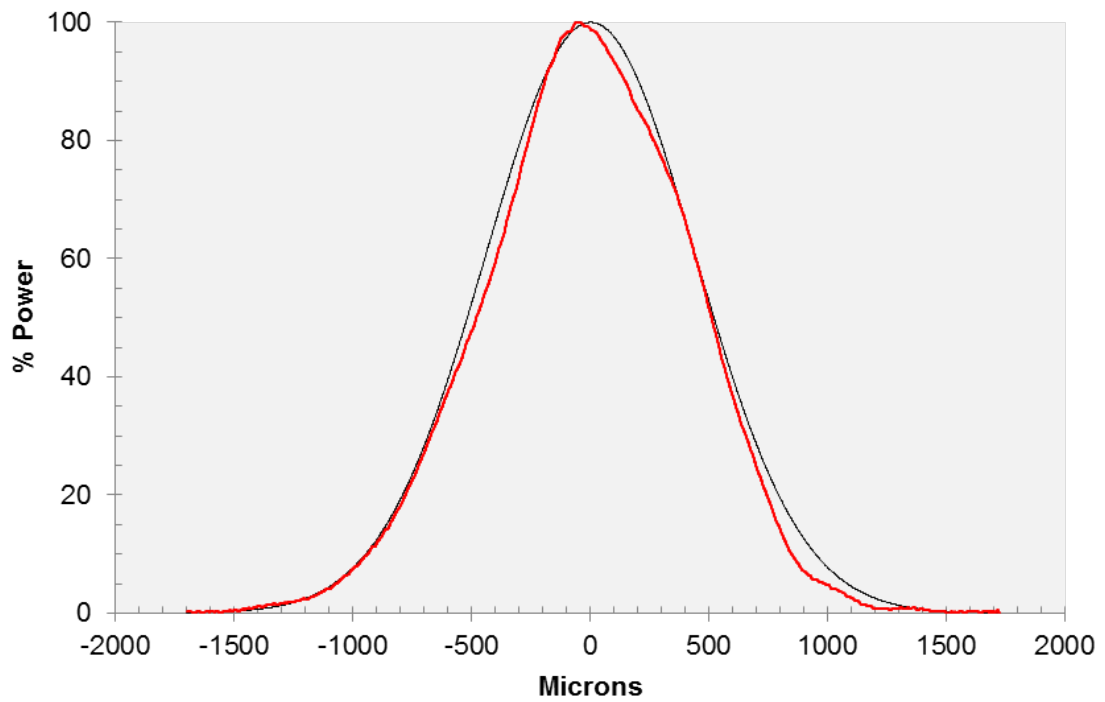


Figure 37: Profile of beam with no test elements in beam path. The red line represents the measured beam profile, and the black line represents the computed beam spot size based on Gaussian propagation.

calculations. Reasons for these are the limitations of the ABCD matrix method to include considerations for offset components and the lack of coating modeling in the version of OSLO used to construct the ray trace models. Additionally, the ray trace model is based on manufacturer-produced values and is an ideal system, while the Matlab computation is based on physical measurements of the system. Thus, the values produced by Matlab are expected to be closer to measured values. OSLO ray trace-produced values are still of use, and will help provide an insight into how the system performs with respect to beam spot size over varying EFLs.

3.4 Performance Results

3.4.1 Transmission Performance Results

The measured transmission plots for the doublet lenses are shown in Figs. 38 - 40. The AR-coated BK7 PCV lenses are shown with black square markers, the rARSS FS PCV lenses are shown with red circle markers, and the uncoated FS PCV lenses are shown with blue triangle markers. Much like earlier results with the singlet lens configurations, there is a deviation between results for the AR-coated BK7 and rARSS FS lens mixtures and the computed metric for all EFLs; however, there is also some deviation of the uncoated FS pairs from the computation for the $50mm$ and $75mm$ EFLs. Tables 11 and 12 show the mean percent difference of the measured transmission from theoretical limits. Lens combinations using one or two lenses with rARSS on the curved surface are on the same magnitude of mean percent difference as those with AR-coated BK7 lenses.

There may be multiple sources of performance loss of doublets. One possible rea-

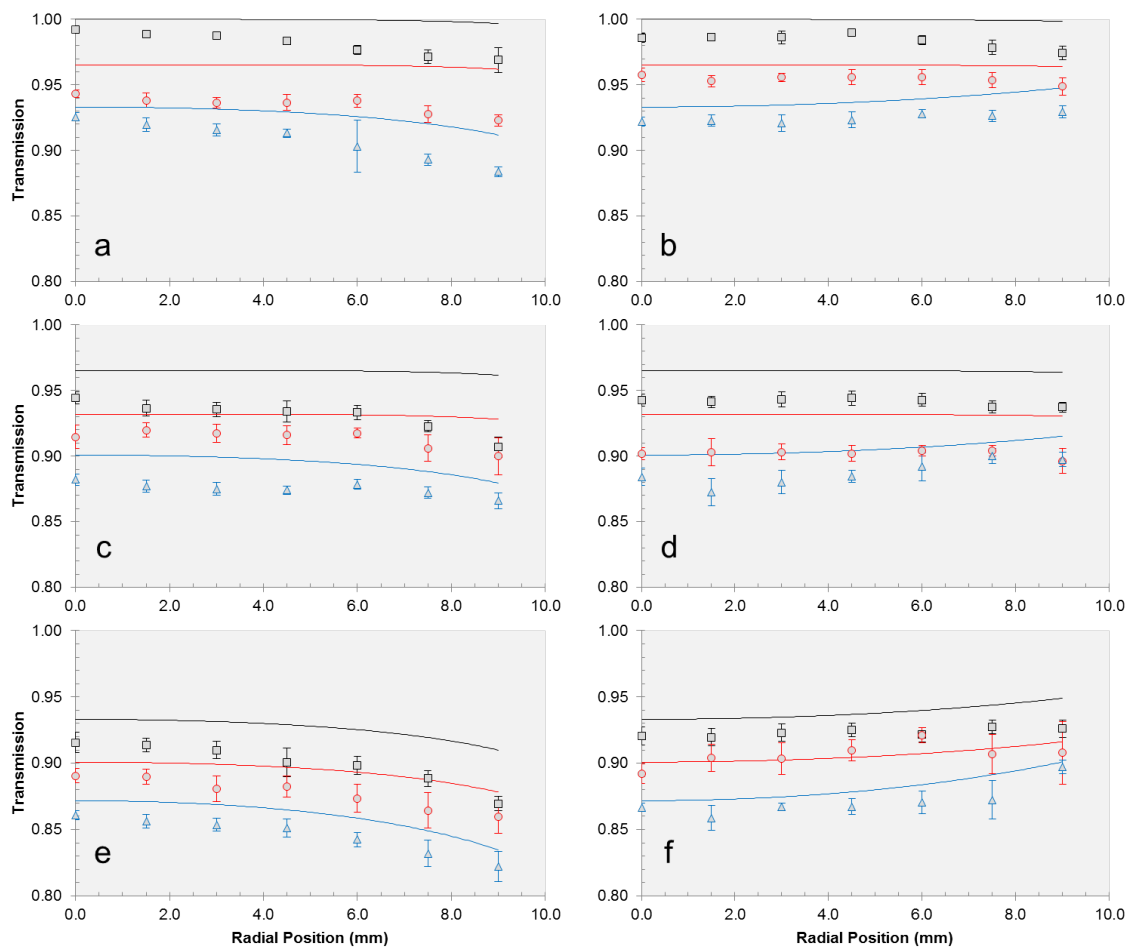


Figure 38: Measured (bullets) and calculated (lines) normalized transmission of a FS 50mm EFL PCX/PCV lens pair as functions of radial distance (r) for double-sided AR-coated BK7 PCV lens (black), single-sided rARSS FS PCV lens (red), and uncoated FS PCV lens (blue). (a) TE and (b) TM incident polarization for an AR-coated BK7 PCX lens. (c) TE and (d) TM incident polarization for a rARSS FS PCX lens. (e) TE and (f) TM incident polarization for an uncoated FS PCX lens. The standard deviation of the experimental measurements is the thickness of the bullets if not shown as a vertical bar.

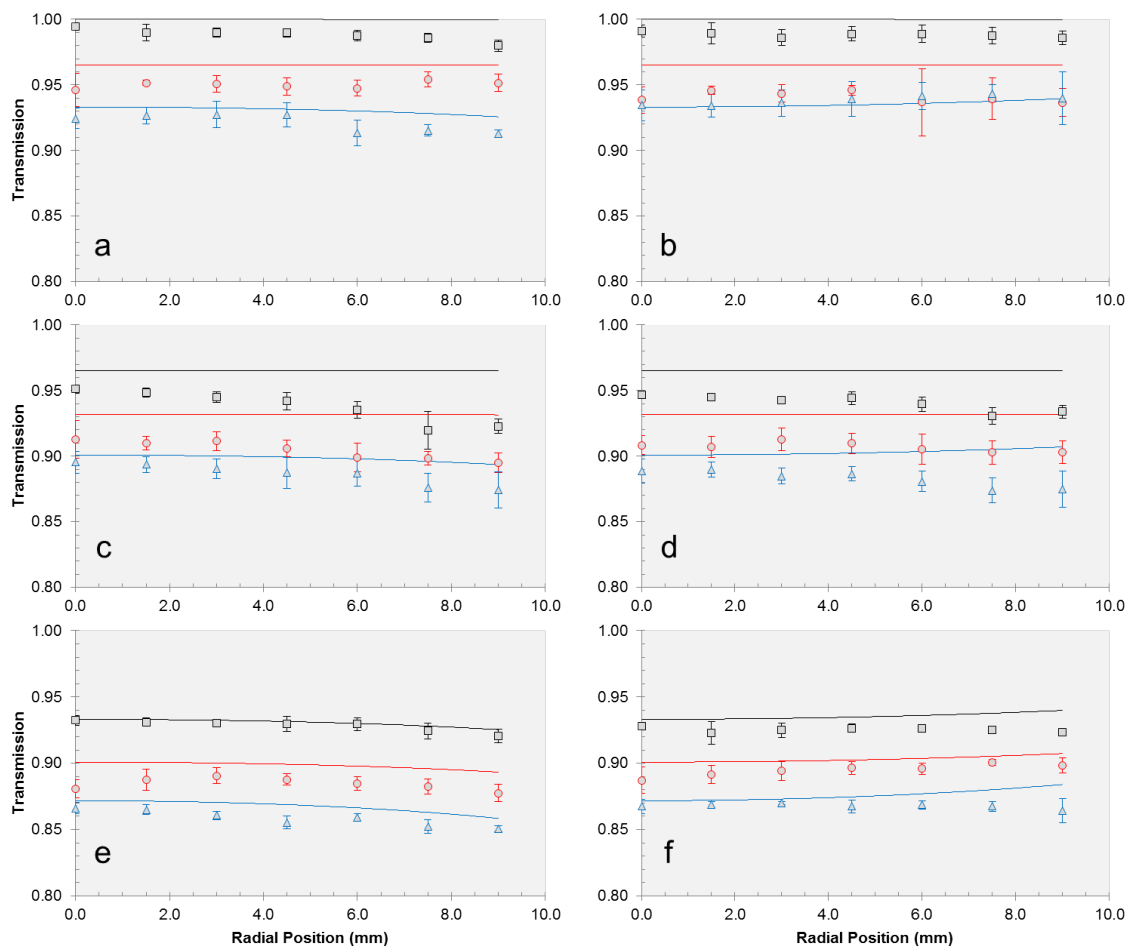


Figure 39: Measured (bullets) and calculated (lines) normalized transmission of a FS 75mm EFL PCX/PCV lens pair as functions of radial distance (r) for double-sided AR-coated BK7 PCV lens (black), single-sided rARSS FS PCV lens (red), and uncoated FS PCV lens (blue). (a) TE and (b) TM incident polarization for an AR-coated BK7 PCX lens. (c) TE and (d) TM incident polarization for a rARSS FS PCX lens. (e) TE and (f) TM incident polarization for an uncoated FS PCX lens. The standard deviation of the experimental measurements is the thickness of the bullets if not shown as a vertical bar.

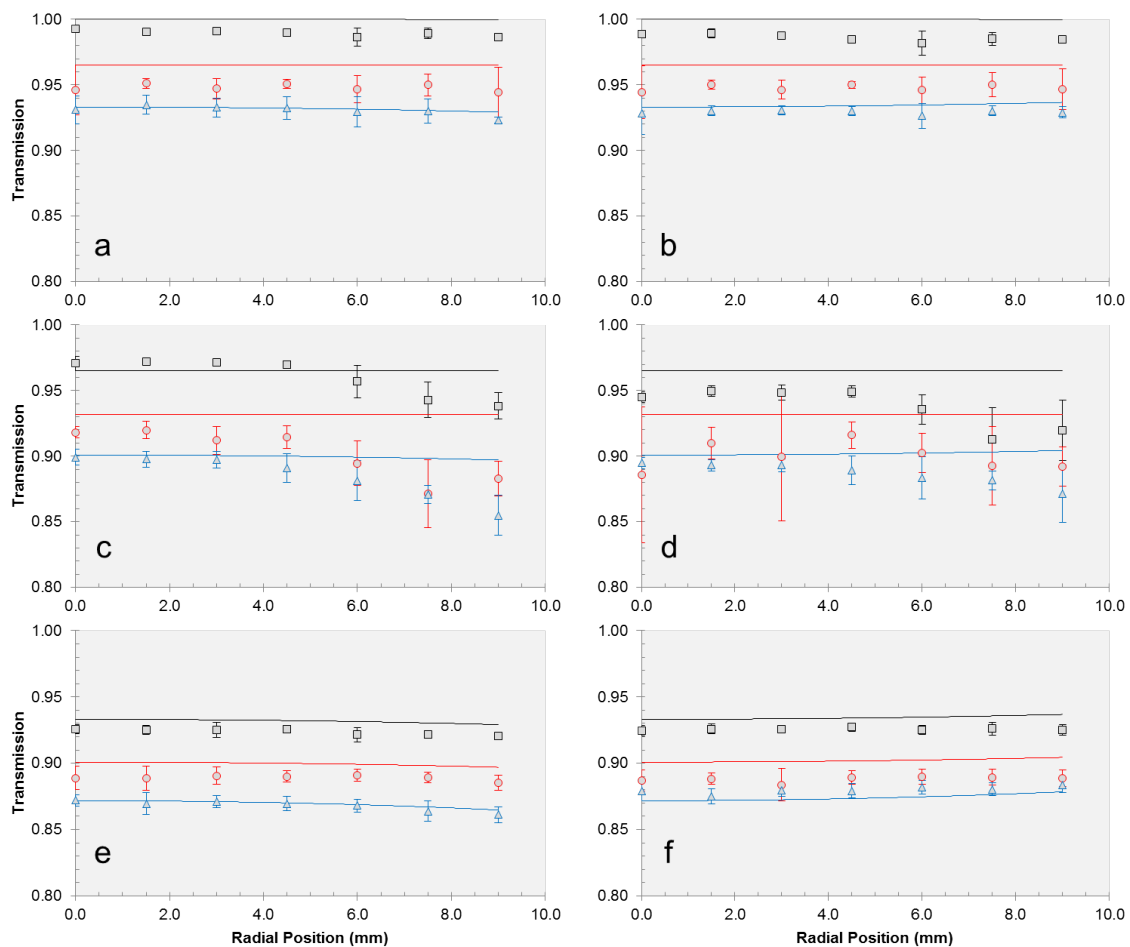


Figure 40: Measured (bullets) and calculated (lines) normalized transmission of a FS 100mm EFL PCX/PCV lens pair as functions of radial distance (r) for double-sided AR-coated BK7 PCV lens (black), single-sided rARSS FS PCV lens (red), and uncoated FS PCV lens (blue). (a) TE and (b) TM incident polarization for an AR-coated BK7 PCX lens. (c) TE and (d) TM incident polarization for a rARSS FS PCV lens. (e) TE and (f) TM incident polarization for an uncoated FS PCX lens. The standard deviation of the experimental measurements is the thickness of the bullets if not shown as a vertical bar.

Table 11: Mean percent difference of measured transmission values for doublet lens samples for TE polarization

EFL (<i>mm</i>)	Positive Lens	Negative Lens		
		Uncoated	rARSS	AR-coated
50	Uncoated	1.69E+00	1.86E+00	2.90E+00
	rARSS	2.16E+00	1.96E+00	3.60E+00
	AR-coated	2.04E+00	3.15E+00	1.82E+00
75	Uncoated	1.01E+00	1.55E+00	2.43E−01
	rARSS	1.35E+00	2.97E+00	2.90E+00
	AR-coated	1.03E+00	1.59E+00	1.18E+00
100	Uncoated	1.69E−01	1.16E+00	8.70E−01
	rARSS	1.69E+00	3.29E+00	1.20E+00
	AR-coated	1.98E−01	1.81E+00	1.06E+00

Table 12: Mean percent difference of measured transmission values for doublet lens samples for TM polarization

EFL (<i>mm</i>)	Positive Lens	Negative Lens		
		Uncoated	rARSS	AR-coated
50	Uncoated	1.20E+00	7.04E−01	1.65E+00
	rARSS	2.08E+00	3.22E+00	2.49E+00
	AR-coated	1.46E+00	1.11E+00	1.61E+00
75	Uncoated	9.61E−01	9.20E−01	1.10E+00
	rARSS	2.28E+00	2.71E+00	2.62E+00
	AR-coated	3.21E−01	2.56E+00	1.17E+00
100	Uncoated	6.52E−01	1.57E+00	9.46E−01
	rARSS	1.73E+00	3.51E+00	2.97E+00
	AR-coated	5.48E−01	1.85E+00	1.40E+00

son is a loss stemming from the cascading of elements that is not present when using transmission from multiple singlet systems. Another reason may be the lower optimization of concave surfaces as compared to convex surfaces from the same etch batch. Losses in the singlet data were interpreted by developing a transmission enhancement function in order to extract the rARSS surface performance. With doublet samples, this function does not give the same insights. Multiple surfaces of rARSS, or mixtures of rARSS and AR-coated surfaces, are unable to be separated in performance evaluations. Thus, to determine whether transmission performance of the doublet configurations is realistic and to discover the loss sources, the transmission efficiency was used.

Additionally, as a comparison, data from the singlet transmission results were used to construct equivalent doublets. This data is from testing that does not exactly match that of the doublet conditions. For example, the initial rARSS surface is the first surface encountered in the singlet configuration and the second in the doublets. This means a direct transmission comparison is not possible. The transmission efficiency, as a value normalized by its corresponding baseline of these constructed doublets, can be directly compared to the in-situ doublet's transmission efficiency.

A summary of transmission efficiency plots of in-situ and constructed doublets is shown in Fig. 41. The transmission efficiency is shown as markers where blue data are from AR-coated BK7 pairs, and red data are from rARSS pairs. The solid lines are transmission efficiencies from comparison computations for in-situ doublets, and the dashed lines are from constructed doublets. The lighter square/circle markers are from in-situ doublets, and the darker square/circle markers are from constructed

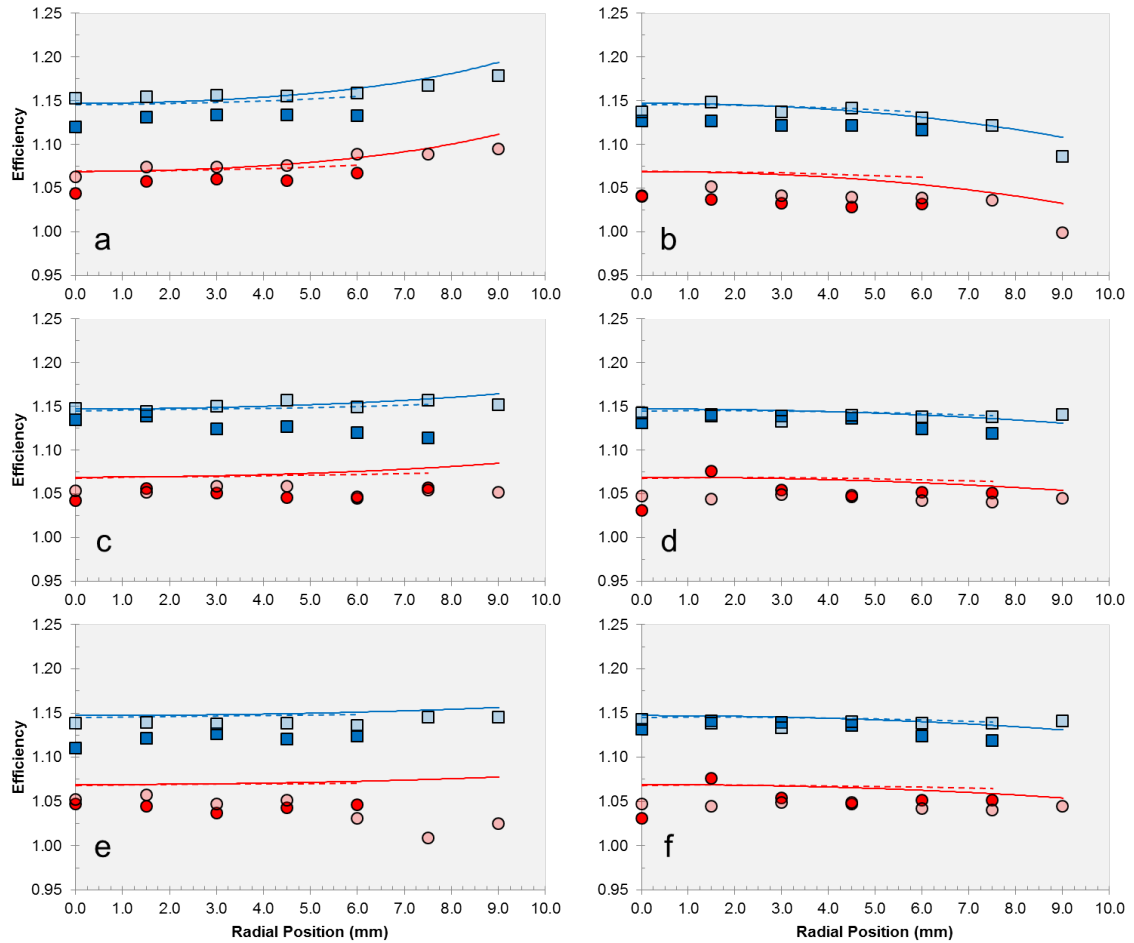


Figure 41: Transmission efficiency of doublet lenses. Blue data are from AR-coated BK7 pairs, and red data are from rARSS pairs. The solid lines are from comparison computations for in-situ doublets, and the dashed lines are from constructed doublets (doublets formed from singlet transmission measurements). The lighter square/circle markers are from in-situ doublets, and the darker square/circle markers are from constructed doublets. The right column of plots are from TE-mode source polarization, and the left column of plots are from TM-mode source polarization. (a) and (b) are data from 50mm EFL lens pairs, (c) and (d) are from 75mm EFL lens pairs, and (e) and (f) are from 100mm EFL lens pairs.

doublets. The right column of plots are from TE-mode source polarization, and the left column of plots are from TM-mode source polarization.

Observations from these plots show general agreement of the transmission efficiency of the in-situ doublets with that of the computation. There is even better agreement of the transmission efficiency between in-situ doublets and constructed doublets. This indicates the transmission loss of multiple rARSS surfaces is not due to a cascading effect, but to the same loss as the singlets. The increased deviation of the doublets away from computation is more than likely due to the transmission loss previously observed in PCV lens samples.

3.4.2 Beam Profile Performance Results

The results from normalized beam profile tests are shown in Figs. 42 - 44. The plots show AR-coated BK7 PCV lenses as black squares, rARSS FS PCV lens samples as red circles, and uncoated FS PCV lenses as blue triangles. Lighter markers indicate data evaluated using the Gaussian fit method, and darker markers indicate data using the FWHM method. Simulated data from Matlab are shown as lines with the colors corresponding to the same PCV lenses as for the measured data. Dotted lines correspond to modeling performed in OSLO ray trace software using a Gaussian paraxial ABCD matrix function. The top plot in each figure is for an AR-coated BK7 PCX lens, the middle plot is for a rARSS FS PCX lens, and the bottom plot is for an uncoated FS PCX lens.

The $50mm$ EFL results still show significant deviation from computation, but the $75mm$ EFL results more closely match the computation. The $100mm$ EFL results

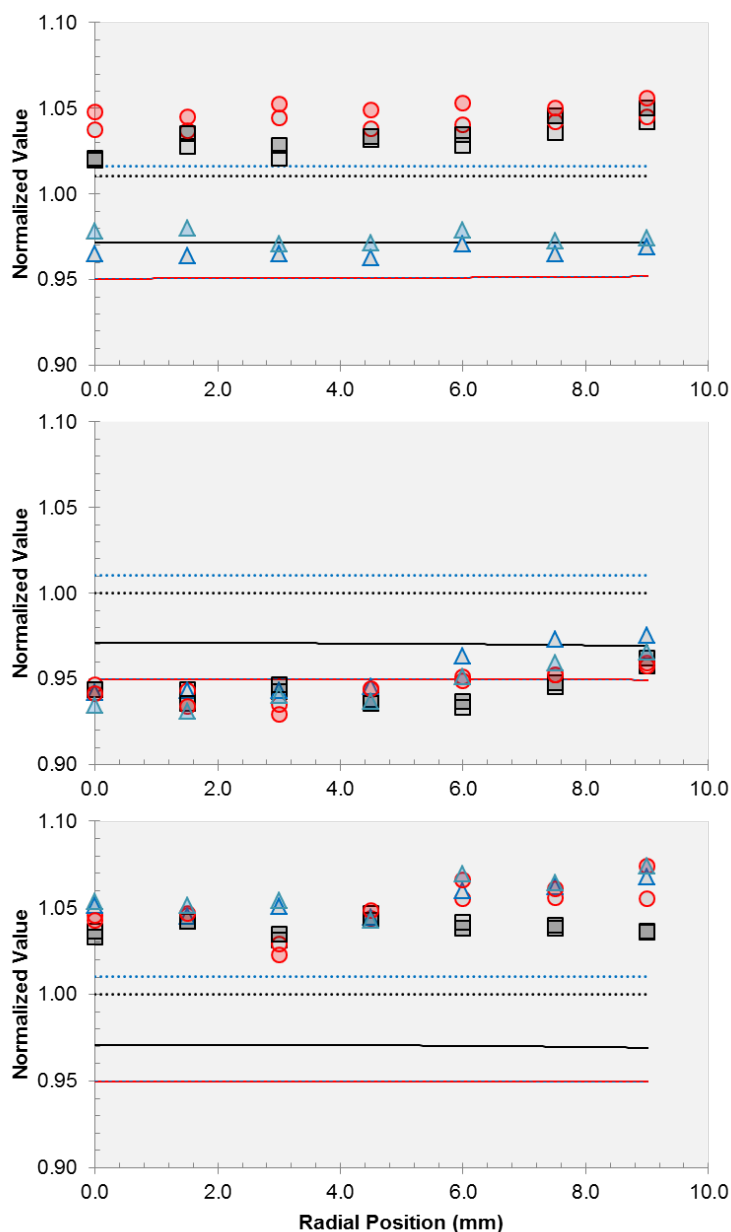


Figure 42: Measured normalized beam spot sizes as a function of radial distance for 50mm EFL doublets. In each plot, AR-coated BK7 PCV lenses are shown as black squares, rARSS FS PCV lens samples are shown as red circles, and uncoated FS PCV lenses are shown as blue triangles. Lighter markers indicate data evaluated using the Gaussian fit method, and darker markers indicate data using the FWHM method. Simulated data are shown as lines with the colors corresponding to the same PCV lenses as for the measured data. Dotted lines correspond to modeling performed in OSLO ray trace software. The top plot is for an AR-coated BK7 PCX lens, the middle plot is for a rARSS FS PCX lens, and the bottom plot is for an uncoated FS PCX lens.

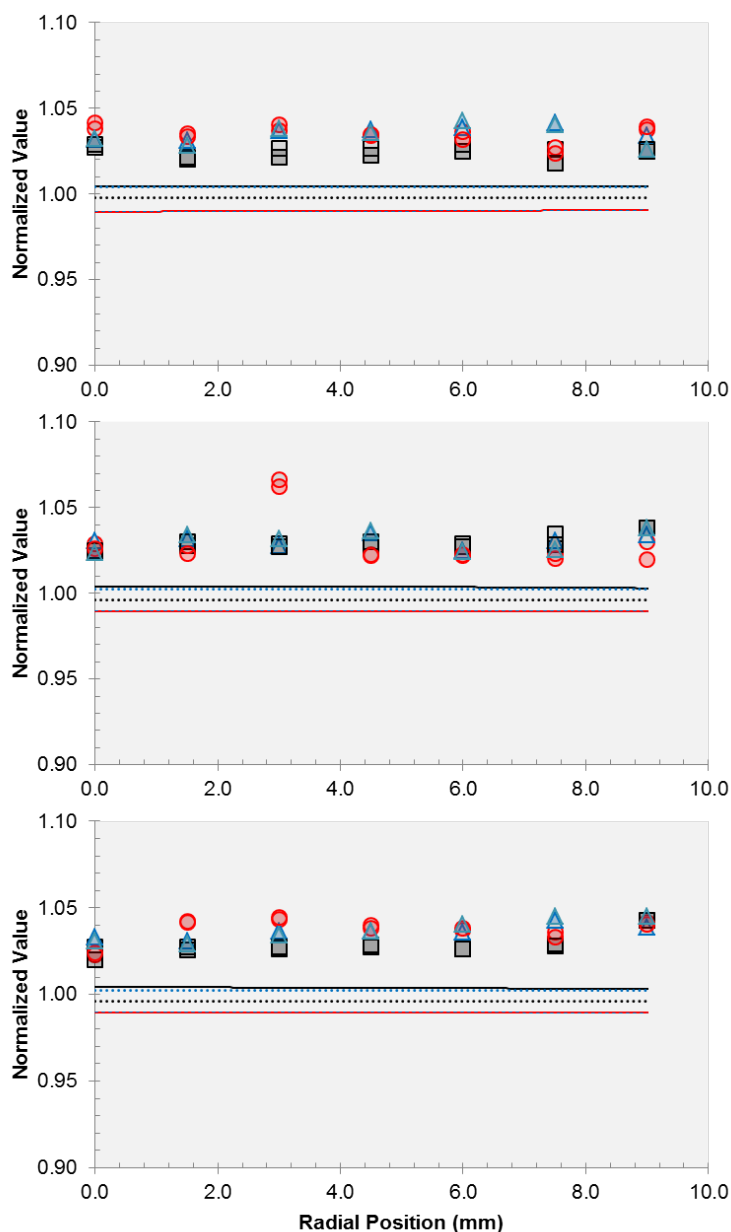


Figure 43: Measured normalized beam spot sizes as a function of radial distance for 75mm EFL doublets. In each plot, AR-coated BK7 PCV lenses are shown as black squares, rARSS FS PCV lens samples are shown as red circles, and uncoated FS PCV lenses are shown as blue triangles. Lighter markers indicate data evaluated using the Gaussian fit method, and darker markers indicate data using the FWHM method. Simulated data are shown as lines with the colors corresponding to the same PCV lenses as for the measured data. Dotted lines correspond to modeling performed in OSLO ray trace software. The top plot is for an AR-coated BK7 PCX lens, the middle plot is for a rARSS FS PCX lens, and the bottom plot is for an uncoated FS PCX lens.

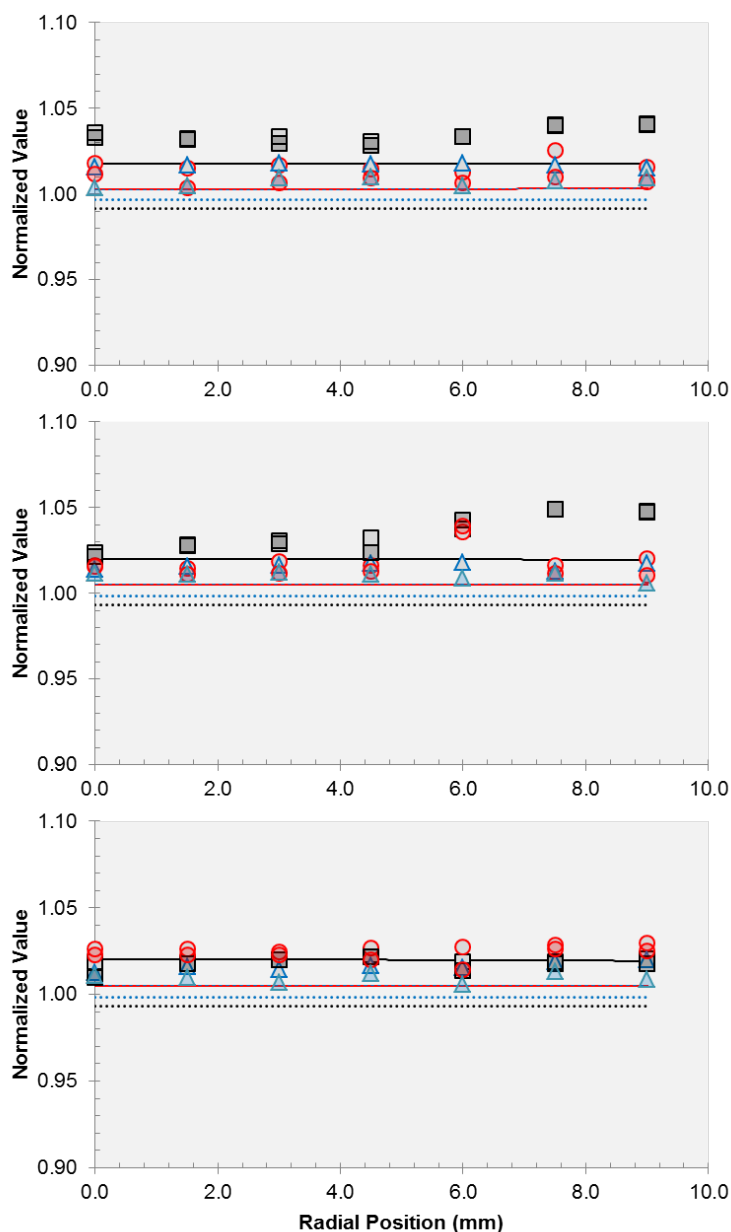


Figure 44: Measured normalized beam spot sizes as a function of radial distance for 100mm EFL doublets. In each plot, AR-coated BK7 PCV lenses are shown as black squares, rARSS FS PCV lens samples are shown as red circles, and uncoated FS PCV lenses are shown as blue triangles. Lighter markers indicate data evaluated using the Gaussian fit method, and darker markers indicate data using the FWHM method. Simulated data are shown as lines with the colors corresponding to the same PCV lenses as for the measured data. Dotted lines correspond to modeling performed in OSLO ray trace software. The top plot is for an AR-coated BK7 PCX lens, the middle plot is for a rARSS FS PCX lens, and the bottom plot is for an uncoated FS PCX lens.

are closer still. All results have a range of $\pm 1.2\mu m$ as determined by the resolution of the beam profiler.

Tables 13 - 18 show the normalized beam spot size ranges between the Gaussian fit method and the FWHM method for 75 and 100mm EFL doublet pairs. Ranges are of similar magnitude across each lens type, most notably on the order of 10^{-3} . This indicates a close match between both analysis methods for all lenses. In conjunction with observed results showing a close match between beam spot sizes from rARSS and uncoated FS lens, there is evidence of low transverse aberration effects in rARSS lenses as compared to uncoated FS lenses.

All of the doublet configurations with PCX and PCV lenses not of the same lens type have a sister doublet where the type of the PCV lens in the first doublet is the type of the PCX lens in the second, and vice versa. For instance, a PCX uncoated FS lens followed by a PCV AR-coated BK7 lens has a corresponding pair with a PCX AR-coated BK7 lens followed by a PCV uncoated FS lens (Fig. 45). While it was found the transmission performance results were not dependent on any cascading effects and were dependent primarily on the individual losses, this may not hold true for beam profile performance. In order to pinpoint whether the order of surfaces has an effect on beam spot size, the normalized data were plotted together according to matching surface arrangements. These plots can be seen in Figs. 46 - 48.

Table 13: Normalized size ranges for beam spot measurements for 75mm EFL matched pairs with an AR-coated BK7 PCX lens.

Position (mm)	Negative Lens		
	Uncoated	rARSS	AR-coated
0.0	5.32E-04	3.69E-03	1.53E-03
1.5	2.58E-03	1.79E-03	1.11E-03
3.0	8.96E-04	3.45E-03	5.31E-03
4.5	2.02E-03	6.86E-04	4.16E-03
6.0	4.24E-03	4.17E-03	4.09E-03
7.5	8.07E-04	3.54E-03	7.90E-03
9.0	7.82E-03	1.65E-03	1.30E-03

Table 14: Normalized size ranges for beam spot measurements for 75mm EFL matched pairs with a rARSS FS PCX lens.

Position (mm)	Negative Lens		
	Uncoated	rARSS	AR-coated
0.0	6.84E-03	2.65E-03	7.64E-04
1.5	2.42E-03	4.82E-03	2.08E-03
3.0	3.86E-03	3.89E-03	1.45E-03
4.5	1.35E-03	8.81E-04	1.74E-03
6.0	5.53E-04	8.11E-04	1.45E-03
7.5	5.01E-03	2.69E-03	6.27E-03
9.0	4.07E-03	1.06E-02	2.30E-04

Table 15: Normalized size ranges for beam spot measurements for 75mm EFL matched pairs with an uncoated FS PCX lens.

Position (mm)	Negative Lens		
	Uncoated	rARSS	AR-coated
0.0	2.53E-03	1.23E-03	7.10E-03
1.5	1.66E-03	4.55E-04	1.54E-03
3.0	2.41E-03	1.27E-03	1.16E-03
4.5	1.35E-04	2.03E-03	1.21E-03
6.0	4.07E-03	8.65E-04	1.84E-04
7.5	2.27E-03	2.70E-03	1.23E-03
9.0	6.67E-03	1.09E-03	3.75E-04

Table 16: Normalized size ranges for beam spot measurements for 100mm EFL matched pairs with an AR-coated BK7 PCX lens.

Position (<i>mm</i>)	Negative Lens		
	Uncoated	rARSS	AR-coated
0.0	1.20E-02	6.32E-03	2.81E-03
1.5	1.18E-02	1.13E-02	3.65E-04
3.0	8.42E-03	1.03E-02	4.07E-03
4.5	7.96E-03	5.60E-03	2.67E-03
6.0	1.33E-02	5.82E-03	2.48E-04
7.5	9.02E-03	1.57E-02	4.76E-04
9.0	5.40E-03	8.71E-03	5.49E-04

Table 17: Normalized size ranges for beam spot measurements for 100mm EFL matched pairs with a rARSS FS PCX lens.

Position (<i>mm</i>)	Negative Lens		
	Uncoated	rARSS	AR-coated
0.0	2.08E-03	1.03E-03	2.04E-03
1.5	4.78E-03	3.38E-03	2.16E-04
3.0	4.23E-03	6.37E-03	1.59E-03
4.5	6.26E-03	3.45E-03	9.04E-03
6.0	9.08E-03	3.31E-03	5.12E-03
7.5	1.04E-03	4.70E-03	3.90E-04
9.0	1.19E-02	9.61E-03	1.29E-04

Table 18: Normalized size ranges for beam spot measurements for 75mm EFL matched pairs with an uncoated FS PCX lens.

Position (<i>mm</i>)	Negative Lens		
	Uncoated	rARSS	AR-coated
0.0	1.99E-03	3.60E-03	9.53E-03
1.5	6.26E-03	3.65E-03	9.66E-04
3.0	7.20E-03	2.18E-03	4.53E-04
4.5	4.64E-03	6.39E-03	1.40E-03
6.0	9.49E-03	1.30E-03	4.82E-03
7.5	5.29E-03	2.22E-03	1.22E-03
9.0	1.13E-02	4.57E-03	2.74E-03

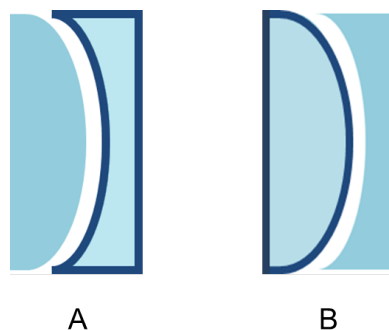


Figure 45: "Sister" doublet configuration sample. A: PCX uncoated FS lens followed by a PCV AR-coated BK7 lens, B: PCX AR-coated BK7 lens followed by a PCV uncoated FS lens.

3.5 Conclusions of Performance of Random Anti-Reflection Surface Structure on Doublet Lenses

The viability of rARSS as a surface treatment to reduce Fresnel reflectivity through multiple surfaces of spherical lens elements has been compared to ideal SLAR thin-film coatings for both incident light polarization orientations. As with the single lens results, theoretical SLAR coating performance was shown to be a useful metric for rARSS on these surfaces. Further, the methodology designed and tested for single lenses was applied for use with doublet lenses in order to evaluate the scalar polarized transmission properties of rARSS on multiple spherical lens topography.

To perform this work, the same six FS lenses of EFLs ± 50 , ± 75 , and ± 100 mm with rARSS used in the singlet work were utilized. Lenses were placed in combinations of one PCX lens, planar side facing the source, followed by a PCV lens of matched curvature with planar side facing away from the source. These lenses were tested in combinations with unprocessed FS lenses and commercially available AR-coated lenses of identical EFL. Measured transmission and transmission efficiency were com-

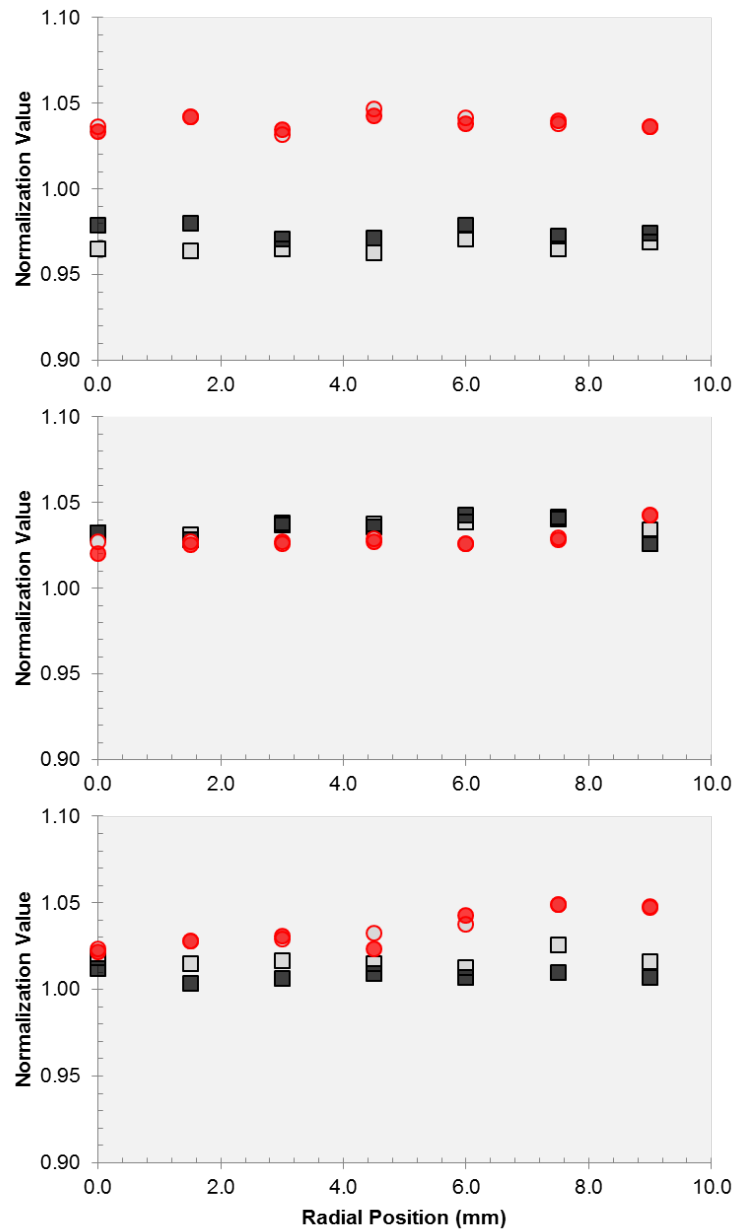


Figure 46: Measured beam spot sizes as a function of radial distance for mixtures of AR-coated BK7 lenses and uncoated FS lenses. Black square markers indicate AR-coated BK7 PCX lenses matched with uncoated FS PCV lenses. Red circle markers indicate uncoated FS PCX lenses and AR-coated BK7 PCV lenses. Lighter markers indicate data evaluated using the Gaussian fit method, and darker markers indicate data evaluated using the FWHM method. The top plot is for 50mm EFL lenses, the middle plot is for 75mm EFL lenses, and the bottom plot is for 100mm EFL lenses.

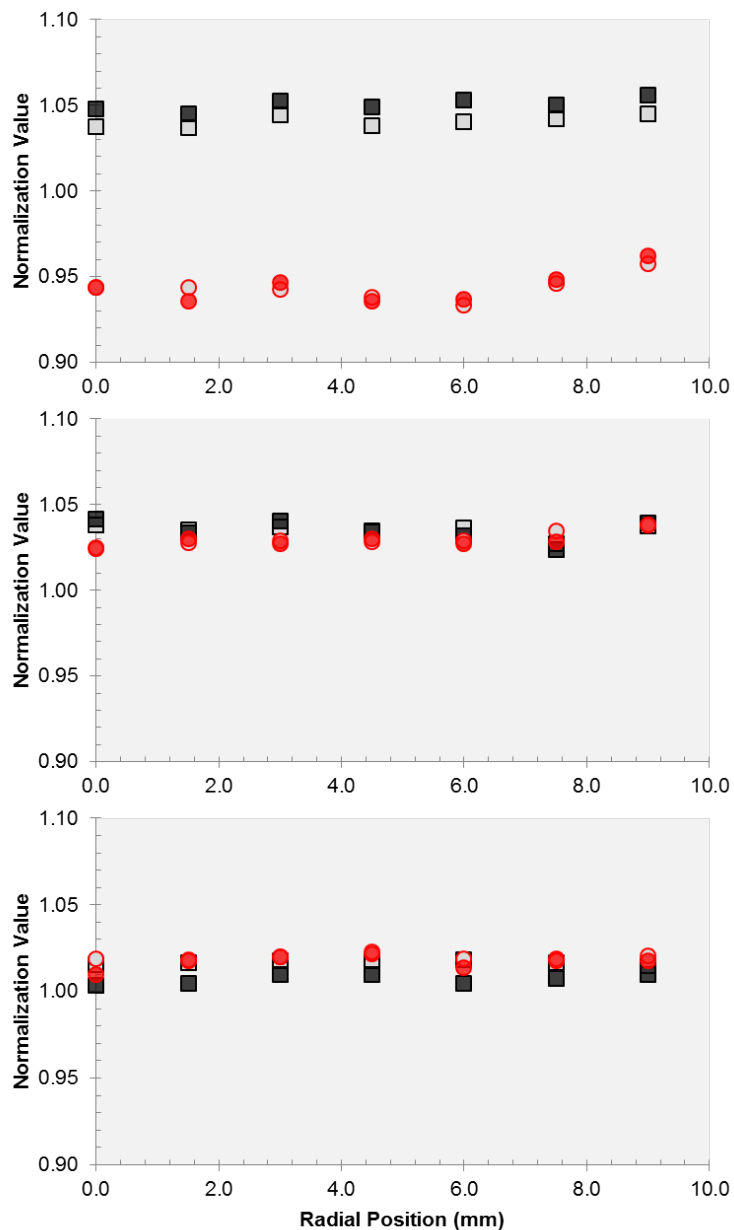


Figure 47: Measured beam spot sizes as a function of radial distance for mixtures of AR-coated BK7 lenses and rARSS lenses. Black square markers indicate AR-coated BK7 PCX lenses matched with rARSS PCV lenses. Red circle markers indicate rARSS PCX lenses and AR-coated BK7 PCV lenses. Lighter markers indicate data evaluated using the Gaussian fit method, and darker markers indicate data evaluated using the FWHM method. The top plot is for 50mm EFL lenses, the middle plot is for 75mm EFL lenses, and the bottom plot is for 100mm EFL lenses.

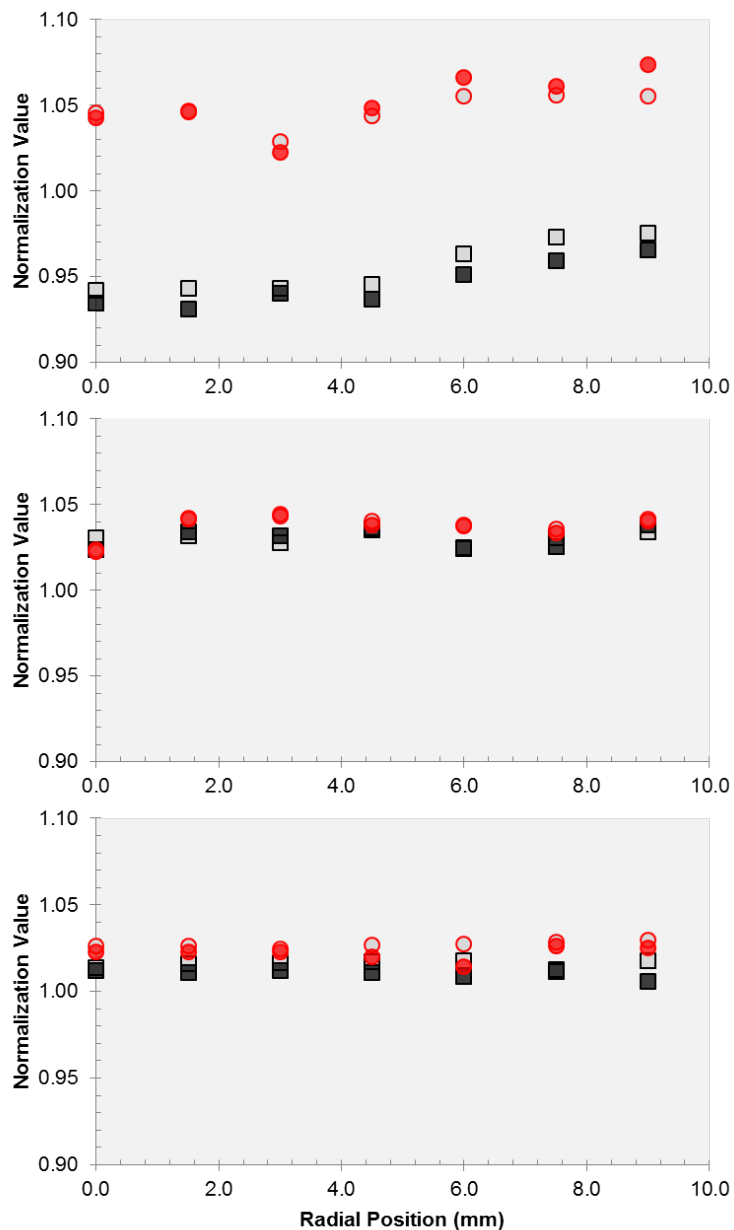


Figure 48: Measured beam spot sizes as a function of radial distance for mixtures of rARSS lenses and uncoated FS lenses. Black square markers indicate rARSS PCX lenses matched with uncoated FS PCV lenses. Red circle markers indicate uncoated FS PCX lenses and rARSS PCV lenses. Lighter markers indicate data evaluated using the Gaussian fit method, and darker markers indicate data evaluated using the FWHM method. The top plot is for 50mm EFL lenses, the middle plot is for 75mm EFL lenses, and the bottom plot is for 100mm EFL lenses.

pared against theoretical values as both a method to evaluate results and to establish a metric for comparison. Additionally, transmission efficiency was calculated for equivalent arrangements of singlet data and compared to doublet transmission efficiency in order to identify sources of loss.

It has been shown that series of spherical surfaces with rARSS do not perform to the computation metrics established. In comparison with data from singlet lenses, it was found that the loss of performance is not dependent on cascading effects, but to lower transmission enhancement for PCV lenses. It is concluded that cascading optical elements, if given optimized rARSS treatment, can perform to computed comparison metrics.

Beam profile measurements were obtained for the same testing method as transmission measurements, and the beam spot sizes for each profile extracted. Profiles were analyzed for beam spot sizes using two different methods in order to reduce bias from element tilt in the optical train prior to the test location. Gaussian beam propagation was computed through the doublet arrangements to provide a comparison for evaluation of performance. Beam spot size performance was found to deviate from computation metrics for higher surface curvatures. Comparisons of lens doublet combinations showed high sensitivity to surface order for higher surface curvatures with a drop to low sensitivity to surface order for lower surface curvatures.

CHAPTER 4: CONCLUSIONS

4.1 Summary of Optical Performance of Random Anti-Reflection Surface Structure

In this work, rARSS treatment optimized for planar substrates has been applied to a set of PCX and PCV FS spherical lenses of EFLs ± 50 , ± 75 , and ± 100 mm. These lenses were tested in singlet and doublet configurations in order to measure transmission performance of rARSS on spherical surfaces. The parameters of interest included surface curvature, sample thickness, radial position from optic axis, linear polarization direction, global angle θ and local angle θ' (Table 19). To test singlet and doublet configurations for the given parameters, a methodology was developed due to the inability of current testing instruments to adequately characterize transmission performance. This methodology was designed to be scalable to other optical elements for future investigations. Another set of FS spherical lenses of equivalent EFLs were etched with a non-optimized process and tested in the singlet configuration under the same test parameters in order to investigate transmission dependencies. Commercially-obtained uncoated FS lenses and AR-coated BK7 lenses were also used to provide control and comparison samples.

To compare and characterize resulting transmission performance, a ray-trace model using Fresnel formulae was constructed. An ideal SLAR thin film model was used as

Table 19: Parameters of interest and values used to test and analyze transmission of rARSS on spherical surfaces.

Parameter of Interest	Values
Surface Curvature (EFL)	$\pm 50mm, \pm 75mm, \pm 100mm$
Sample Thickness	$2.0mm - 5.9mm$
Radial Position	$0.0mm, 1.5mm, \dots, 9.0mm$
Linear Polarization	TE, TM
Global Angle θ	$0^\circ, 15^\circ, 30^\circ$
Local Angle θ'	$-20^\circ - 50^\circ$

a comparison tool for rARSS on spherical surfaces. The goal of this model is not to exactly match the rARSS performance, but to provide a universal threshold by which future iterations of etching optimization on curved surfaces can be evaluated. This model was found to meet those goals.

PCX lenses were found to meet the same transmission performance measured with planar substrates using the same optimized etch recipe. Lens measurements were also found to keep high transmission enhancement over a wide FOV, similar to the enhancement values found with rARSS on planar substrates. PCV lenses, while found to have enhanced transmission in comparison with bare FS lenses over a wide FOV, did not perform to the same transmission enhancement level as the PCX lenses. The non-optimized lenses were predictably found to have lower transmission enhancement, and in some cases performed below that of the bare substrate. When evaluating dependencies of transmission enhancement on each lens set, the dominant variable for lenses with optimized etch recipes is AOI as seen by the surface of the lens. For lenses with non-optimized etches, the dominant variable was the thickness of each lens at each radial position.

Observations were made from SEM images collected from $\pm 50mm$ EFL optimized

and non-optimized lenses. Structures on both optimized 50mm EFL lenses were similar in shape, density, and size. Small orientation changes were observed across the $+50\text{mm}$ EFL lens, and small size changes were observed across the -50mm EFL lens. The non-optimized samples each had unique structure. All lens samples showed some evidence of isotropic pillar formation, but more conclusive statements cannot be made without further investigation

For future lens samples with rARSS treatment, PCX and PCV should be etched with different optimized recipes in order to achieve maximum transmission enhancement. The PCX lenses should be processed using the same etch recipe for a planar substrate. The PCV lenses require further parameterization of the optimized etch recipe for a planar substrate; however, it is predicted that a new recipe for PCV lenses will be similar to the original recipe due to the current substantial transmission enhancement over the bare substrate. For an etch recipe not optimized for transmission at 633nm , both PCX and PCV lenses will have highly varying transmission functions over the substrate profile.

Doublet lens configurations were measured with the same testing method, but without AOI variation. It was found that transmission did not meet the computed metrics. In comparison to singlet lens transmission, the doublet transmission losses were determined to be a result of PCV lens transmission loss and not due to cascading effects. It is concluded that higher optimization of rARSS on PCV lenses will result in a direct increase of transmission performance in doublet configurations.

The beam profile, and subsequently the beam spot size, was measured for the same doublet lens configurations and parameters. As with the transmission measurements,

the beam spot size was computed for comparison by using SLAR surfaces in lieu of an exact physical model for rARSS. A matrix method developed for Gaussian beam propagation through the doublets was used to compute the beam spot size results. While beam spot size results did not agree closely for the doublets, normalization and multiple analysis approaches allowed for more appropriate comparisons. The surface curvature was found to have an effect on beam spot size, with higher surface curvatures performing with higher deviation from expected values than lower surface curvatures.

In order to understand the dependence of beam spot size on the sequence of surfaces in the beam path, doublets with matching surfaces but different sequence (for example, an AR-coated BK7 PCX lens with a rARSS PCV lens versus a rARSS PCX lens with an AR-coated BK7 PCV lens) were compared. Higher surface curvature doublets produced beam spot sizes with significant deviation between matching surfaces of different sequence. The same was not observed for lower surface curvature doublets, and beam spot sizes from these sample pairs were closely matched.

4.2 Future Work

4.2.1 Random Anti-Reflection Surface Structure on Microlens Arrays

In the work presented, the optical elements of interest have been spherical PCX and PCV FS lenses. Etch recipe optimization has been well-documented for planar substrates, and it was found the same etch recipes can be extended to PCX lenses in particular to achieve similar transmission enhancement performance. Given both surface types benefit from the same etch process, it could be hypothesized that com-

binations of these surfaces could benefit as well. A common mixture is a MLA.

AR thin films are not viable solutions for many MLA applications due to the lack of environmental robustness as well as deposition issues in the junctions between lenses in the array [74, 75]. Ordered ARSS can be added to a MLA surface via imprinting, which limits materials to polymers [75–78]. This can result in reproduction errors and high resource costs as well. The structure is also isotropic, which can limit the open aperture of the individual lenses. Testing of these elements is also through a qualitative analysis of imaging and transmission, often offering an incomplete characterization of MLA capabilities.

Proposed future research is the application of rARSS on a MLA. The resistance to environmental damage and repeatability of fabrication make MLAs good candidates for rARSS treatment. There has been some previous work showing the possibility of successful structures on MLA surfaces [29, 31]. One possible future investigation is to examine the formation of anisotropic random structure on the MLA itself, and compare this to reported results of periodic structure on MLAs. Of particular interest is how this structure will form at the junction of a microlens with the planar substrate. As an optical performance test, a measurement system similar to the same arrangement presented in this work (Figs. 8) could be utilized. AR-coated MLAs as well as uncoated MLAs could be used as control and comparison samples.

4.2.2 Wavefront Performance and Scattering Measurements of Random Anti-Reflection Surface Structure on Non-Planar Surfaces

Transmission and beam profile performances of rARSS on spherical lenses have been investigated in this work. An additional characterization that will help to provide a complete understanding of the performance capabilities of rARSS on curved surfaces will be to investigate the beam wavefront from such elements. Wavefront deformation in other lens samples treated with surface structure similar to rARSS has been shown to be a useful metric in characterizing plasma etch rates [36]. It may also help to evaluate application of rARSS-treated lenses in optical element trains where wavefront deformation is detrimental to proper operation.

Particular attention is to be paid to characterizing scattering losses from optical power elements. In investigations of planar elements, it has been found that substrates with rARSS produce significantly low scatter uniformly distributed over 4π steradians [33,34]. This is of importance to high-power laser applications, where small scattering loss can have high enough amplitude to cause damage in other systems and users.

By evaluating scattering and wavefront deformation for these optical power elements, applications of rARSS on spherical lenses can be rated for interferometric or phase-sensitive systems.

REFERENCES

- [1] H. A. McLeod, Thin-film optical filters. CRC Press. (2010).
- [2] U. Schallenberg, Design principles for broadband AR coatings. Proc. SPIE. **7101**(2008), 710103-1.
- [3] C. H. Sun, B. J. Ho, B. Jiang, and P. Jiang, Biomimetic subwavelength antireflective gratings on GaAs. Opt. Lett.. **33**(2008), 2224–2226.
- [4] Y. Kanamori, M. Sasaki, and K. Hane, Broadband antireflection gratings fabricated upon silicon substrates. Opt. Lett.. **29**(1999), 1422–1424.
- [5] P. Lalanne and G. M. Morris, Design, fabrication and characterization of subwavelength periodic structures for semiconductor anti-reflection coating in the visible domain. Proc. SPIE. **2776**(1996), 300–308.
- [6] D. S. Hobbs and B. D. MacLeod, design, fabrication, and measured performance of anti-reflecting surface textures in infrared transmitting materials. Proc. SPIE. **5786**(2005), 40.
- [7] T. Lohmüller, M. Helgert, M. Sundermann, R. Brunner, and J. P. Spatz, Biomimetic interfaces for high-performance optics in the deep-UV light range. Nano Lett.. **8**(2008), 1429–1433.
- [8] Y. M. Song, H. J. Choi, J. S. Yu, and Y. T. Lee, Design of highly transparent glasses with broadband antireflective subwavelength structures. Opt. Exp.. **18**(2010), 13063–13071.
- [9] Y. Kanamori, H. Kikuta, and K. Hane, Broadband antireflection gratings for glass substrates fabricated by fast atom beam etching. Jpn. J. Appl. Phys.. **39**(2000), L735–L737.
- [10] A. Gombert, W. Glaubitt, K. Rose, J. Dreibholz, B. Bläsi, A. Heinzl, D. Sporn, W. Döll, and V Wittver, Subwavelength-structured antireflective surfaces on glass. Thin Solid Films. **351**(1999), 73–78.
- [11] A. Gombert, K. Rose, A. Heinzl, W. Horbelt, C. Zanke, B. Bläsi, and V. Wittver, Antireflective submicrometer surface-relief gratings for solar applications. Solar Energy Materials and Solar Cells. **54**(1998), 333–342.
- [12] Y. Kanamori, M. Sasaki, and K. Hane, High aspect-ratio two-dimensional silicon subwavelength gratings fabricated by fast atom beam etching. Proc. SPIE. **3874**(1999), 345–354.
- [13] Y. Kanamori, M. Sasaki, and K. Hane, Antireflection structures for visible and infrared wavelengths fabricated on silicon substrates by fast atom beam etching. Proc. SPIE. **3740**(1999), 484–487.

- [14] P. Nubile, Analytical design of antireflection coatings for silicon photovoltaic devices. *Thin Solid Films*. **342**(1999), 257–261.
- [15] J. A. Dobrowolski, D. Poitras, P. Ma, H. Vakil, and M. Acree, Toward perfect antireflection coatings: numerical investigation. *Appl. Opt.* **41**(2002), 3075–3083.
- [16] T. Maier, D. Bach, P. Müllner, R. Hainberger, and H. Brückl, Antireflective surface structures in glass by self-assembly of SiO₂ nanoparticles and wet etching. *Opt. Exp.* **21**(2013), 20254–20259.
- [17] M. E. Motamedi, W. H. Southwell, and W. J. Gunning, Antireflection surfaces in silicon using binary optics technology. *Appl. Opt.* **31**(1992), 4371–4376.
- [18] J. Ullmann, M. Mertin, H. Lauth, H. Bernitzki, K. Mann, D. Ristau, W. Arens, R. Thielsch, and N. Kaiser, Coated optics for DUV-excimer laser applications. *Proc. SPIE*. **3578**(1998), 64.
- [19] W. H. Southwell, Pyramid-array surface-relief structures producing antireflection index matching on optical surfaces. *J. Opt. Soc. Am. A*. **8**(1991), 549–553.
- [20] E. Olivia. F. Dimroth, and A. W. Bett, GaAs converters for high power densities of laser illumination. *Prog. Photovolt: Res. Appl.* **16**(2008), 289–295.
- [21] Z. Yu, H. Gao, W. Wu, H. Ge, and S. Y. Chou, Fabrication of large area subwavelength antireflection structures on Si using trilayer resist nanoimprint lithography and liftoff. *J. Vac. Sci. Technol. B*. **21**(2003), 2874–2877.
- [22] W. H. Lowdermilk and D. Milam, Graded index antireflection surfaces for high power laser applications. *Appl. Phys. Lett.* **36**(1980), 891–893.
- [23] D. S. Hobbs, B. D. MacLeod, and J. R. Riccobono, Update on the development of high performance anti-reflecting surface relief micro-structures. *Proc. SPIE*. **6545**(2007), 65450Y.
- [24] K.-N. Tu, *Electronic thin-film reliability*. Cambridge University Press. (2011).
- [25] P. Baumeister, *Optical Coating Technology*. SPIE Press (2004).
- [26] Y. Kanamori and K. Hane, 100 nm period silicon antireflection structures fabricated using a porous alumina membrane mask. *Appl. Phys. Lett.* **78**(2001), 142–143
- [27] S. J. Wilson and M. C. Hutley, The optical properties of 'moth eye' antireflection surfaces. *Optica Acta*. **29**(1982), 993–1009.
- [28] H. Kikuta, H. Toyota, and W. Yu, Optical elements with subwavelength structured surfaces. *Opt. Rev.* **10**(2003), 63–73.

- [29] H. Jung, C. Song, and K. Jeong, Monolithic polymer microlens arrays with anti-reflective structures using a metal annealed mask. *Proceedings of IEEE Conference on Optical MEMS and Nanophotonics*. (2011), 145–146.
- [30] J. R. Wendt, G. A. Vawter, R. E. Smith, and M. E. Warren, Fabrication of subwavelength, binary, antireflection surface-relief structures in the near infrared. *J. Vac. Sci. Technol. B*. **14**(1996), 4096–4098.
- [31] K. M. Baker, Highly corrected close-packed microlens arrays and moth-eye structuring on curved surfaces. *Appl. Opt.* **38**(1999), 352–356.
- [32] P. Lalanne and G. M. Morris, Antireflection behavior of silicon subwavelength periodic structures for visible light. *Nanotechnology*. **8**(1997), 53-56.
- [33] L. E. Busse, C. M. Florea, J. A. Frantz, L. B. Shaw, I. D. Aggarwal, M. K. Poutous, R. Joshi, and J. S. Sanghera, Anti-reflective surface structure for spinel ceramics and fused silica windows, lenses, and optical fibers. *Opt. Mater. Express*. **4**(2014), 2504–2515.
- [34] L. E. Busse, C. M. Florea, L. B. Shaw, J. A. Frantz, S. Bayya, M. K. Poutous, R. Joshi, I. D. Aggarwal, and J. S. Sanghera, Antireflective surface structures on optics for high energy lasers. *Proc. SPIE*. **8959**(2014), 89591L.
- [35] X. Jing, J. Ma, S. Liu, Y. Jin, H. He, J. Shao, and Z. Fan, Analysis and design of transmittance for an antireflective surface microstructure. *Opt. Express*. **17**(2009), 16119–16134.
- [36] M. Schulze, D. Lehr, M. Helgert, E.–B. Kley, and A. Tünnermann, Transmission enhanced optical lenses with self-organized antireflective subwavelength structures for the UV range. *Opt. Lett.* **36**(2011), 3924–3926.
- [37] C. Taylor, K. J. Major, R. Joshi, L. E. Busse, J. Frantz, J. S. Sanghera, I. D. Aggarwal, and M. K. Poutous, Optical performance of random anti-reflective structures on curved surfaces. *Proc. SPIE*. **9359**(2015), 935916.
- [38] C. Taylor, L. E. Busse, J. Frantz, J. S. Sanghera, I. D. Aggarwal, and M. K. Poutous, Angle-of-incidence performance of random anti-reflection structures on curved surfaces. *Applied Optics*. **55**(2016), 2203-2213.
- [39] G. Sapkota, J. R. Case, L. E. Busse, J. A. Frantz, L. B. Shaw, J. S. Sanghera, I. D. Aggarwal, and M. K. Poutous, Characterization of random anti-reflecting surface structures and their polarization response at off-normal angles of incidence. *Proc. SPIE*. **9927**(2016), 992712.
- [40] A. K. Sood, G Pethuraja, A. W. Sood, R. E. Welser, and Y. R. Puri, Development of large area nanostructured AR coatings for EO/IR sensor applications. *Proc. of SPIE*. **8868**(2013), 88680P1–88680P10.

- [41] Y. Li, J. Zhang, S. Zhu, H. Dong, F. Jia, Z. Wang, Y. Tang, L. Zhang, S. Zhang, and B. Yang, Bioinspired silica surfaces with near-infrared improved transmittance and superhydrophobicity by colloidal lithography. *Langmuir*. **26**(2010), 9842–9847.
- [42] H. Toyota, K. Takahara, M. Okano, T. Yotsuya, and H. Kikuta, Fabrication of microcone array for antireflection structured surface using metal dotted pattern. *Jpn. J. Appl. Phys.*. **40**(2001), L747–L749.
- [43] C. Morhard, C. Pacholski, D. Lehr, R. Brunner, M. Helgert, M. Sundermann, and J. P. Spatz, Tailored antireflective biomimetic nanostructures for UV applications. *Nanotechnology*. **21**(2010), 425301.
- [44] M. Schulze, H.-J. Fuchs, E.-B. Kley, A. Tünnermann, New approach for antireflective fused silica structures by statistical nanostructures. *Proc. of SPIE*. **6883**(2008), 68830N1–68830N10.
- [45] T. Prakesh, Submicron size patterned nickel soft lithographic masters using aluminum template. *Soft Nano. Lett.*. **1**(2011), 41–45.
- [46] M. Schaepkens and G. S. Oehrlein, A review of SiO₂ etching studies in inductively coupled fluorocarbon plasmas. *J. Electrochem. Soc.*. **148**(2001), C211–C221.
- [47] V. M. Donnelly and A. Kornblitb, Plasma etching: yesterday, today, and tomorrow. *J. Vac. Sci. Technol. A*. **31**(2013), 050825-1.
- [48] J. W. Coburn, *Plasma Etching and Reactive Ion Etching*. American Institute of Physics. (1982).
- [49] M. Sugawara, *Plasma Etching: Fundamentals and Applications*. Oxford University Press, Inc.. (1998).
- [50] S. C. Brown, *Basic Data of Plasma Physics*. American Institute of Physics. (1994).
- [51] F. Rainer, W. Lowdermilk, D. Milam, T. Hart, T. Lichtenstein, and C. Carniglia, Scandium oxide coatings for high-power UV laser applications. *Appl. Opt.*. **21**(1982), 3685–3688.
- [52] B. Andre, L. Poupinet, and G. Ravel, Evaporation and ion assisted deposition of HfO₂ coatings: some key points for high power laser applications. *J. Vac. Sci. Technol. A*. **18**(2000), 2372–2377.
- [53] Corning Incorporated, "Corning HPFS 7979, 7980, 8655 fused silica," <https://www.corning.com>.
- [54] M. Born and E. Wolf, *Principles of Optics*. Cambridge University. (1999).
- [55] D. C. O'Shea, *Elements of modern optical design*. John Wiley & Sons, Inc. (1985).

- [56] R. P. Riesz and R. Simon, Reflection of a Gaussian beam from a dielectric slab. *J. Opt. Soc. Am. A.* **2**(1985), 1809–1817.
- [57] M. McGuirk and C. K. Carniglia, An angular spectrum representation approach to the Goos-Hänchen shift. *J. Opt. Soc. Am.* **67**(1977), 103–107.
- [58] J. E. Harvey, R. G. Irvin, R. N. Pfisterer, Modeling physical optics phenomena by complex ray tracing. *Opt. Eng.* **53**(2015), 035105–1.
- [59] A. Siegman, *Lasers*. University Science Books. (1986).
- [60] A. A. Tovar and L. W. Casperson, Generalized beam matrices: Gaussian beam propagation in misaligned complex optical systems. *J. Opt. Soc. Am. A.* **12**(1995), 1522-1533.
- [61] M. Ram, A method for investigating off-axis Gaussian beams. Debye Institute, University of Utrecht. (2014).
- [62] C. A. Bennett, *Principles of Physical Optics*. Wiley-Interscience. (2008).
- [63] J. M. Geary, *Introduction to Lens Design with Practical ZEMAX[®] Examples*. Willmann-Bell, Inc.. (2011).
- [64] Thorlabs, Inc., "Red HeNe Laser System: 5.0 mW, Linear, 120 VAC," thorlabs.com.
- [65] Thorlabs, Inc., "N-BK7 Plano-Convex Lenses (AR Coating: 350 - 700 nm)," thorlabs.com.
- [66] Thorlabs, Inc., "Photodiode Power Sensors (C-Series)," thorlabs.com.
- [67] Thorlabs, Inc., "1" (25 mm) Travel Translation Stages," thorlabs.com.
- [68] Thorlabs, Inc., "Rotation Platform," thorlabs.com.
- [69] Schott, "Data Sheets Optical Glasses from Schott," schott.com.
- [70] Thorlabs, Inc., "Optical Coatings," thorlabs.com.
- [71] Edmund Optics, Inc., "Anti-Reflection (AR) Coatings," edmundoptics.com.
- [72] D. Pekker and L. Pekker, A method for determining thickness and optical constants of absorbing thin films. *Thin Solid Films.* **425**(2003), 203–209.
- [73] Thorlabs, Inc., "Scanning Slit Optical Beam Profilers," thorlabs.com.
- [74] K. Hermans, S. Z. Hamidi, A. B. Spoelstra, C. W. M. Baastiaansen, and D. J. Broer, Rapid, direct fabrication of antireflection-coated microlens arrays by photoemposing. *Applied Optics.* **47**(2008), 6512-6517.

- [75] S. S. Oh, C. G. Choi, and Y. S. Kim, Fabrication of micro-lens arrays with moth-eye antireflective nanostructures using thermal imprinting process. *Micro-electronic Engineering*. **87**(2010), 2328-2331.
- [76] Y. P. Chen, C. H. Lee, and L. A. Wang, Fabrication and characterization of multi-scaled microlens arrays with anti-reflection and diffusion properties. *Nanotechnology*. **22**(2011), 21503-21511.
- [77] D. H. Ko, J. R. Tumbleston, K. J. Henderson, L. E. Euliss, J. M. DeSimone, R. Lopez, and E. T. Samulski, Biomimetic microlens array with antireflective moth-eye surface. *Soft Matter*. **7**(2011), 6404-6407.
- [78] T. Yanagishita, K. Nishio, and H. Masuda, Anti-reflection structures on lenses by nanoimprinting using ordered anodic porous alumina. *Applied Physics Express*. **2**(2009), 022001.